Threads in the Tapestry of Next Generation Nanodevices: Simulation and Thin Film Processing

Thesis by
David Spencer Catherall

In Partial Fulfillment of the Requirements for the
Degree of
Doctor of Philosophy

CALIFORNIA INSTITUTE OF TECHNOLOGY
Pasadena, California

2026
Defended March 23, 2026

David Spencer Catherall
ORCID: 0000-0002-3540-2419

ACKNOWLEDGEMENTS

The person most deserving of acknowledgment is, of course, Dr. Austin Minnich, who has been my advisor since Spring 2021. Each year I love to volunteer with prospective student activities, and I always get asked for my most important criteria in choosing a grad school. My answer has always been that you should choose a school with faculty that you would want to work with. I came to Caltech, in part, because there was a wide selection of faculty with interesting research so although I had no specific one in mind when starting, I was confident I could find a good fit. Now, with six years of hindsight, I believe that out of all the options available, joining the Minnich group was the best choice. The collaborative and friendly group culture, the knowledge and mentorship from Austin, and the interesting projects he's brought to the table have made my experience not just extremely valuable but a generally enjoyable one. In addition, I want to thank my thesis committee, Professors Brent Fultz, Joe Falson, and Linda Ye, for finding the time to review this work.

Second, I must thank the students who have helped me throughout this process. This includes Alex, Peishi, and Ben, who were the first I worked with while learning the ropes as a graduate student. My first project was quite a bit outside of my previous expertise, and it was standing on their shoulders that I was able to eventually publish my first papers. In my second project, Haozhe was a great help both in both experimental design and execution. Finally, making the Minnich laboratory what it is now would not have been possible without Azmain, Ivy, Mete, Yifei, or Fin.

While I've now covered the academic acknowledgments, life is a lot more than just sitting in a laboratory. For enriching my time and giving me things to look forward to, I thank my partner Shane and the couple dozen of my local friends. Most of my best memories from the last six years have been from our various gatherings and antics. Lastly, I thank my parents for always having been supportive of me, even though I know I may not have followed the path in life they envisioned before I moved out and started finding my own path.

ABSTRACT

Modern nanodevices such as silicon integrated circuits and superconducting quantum bits achieve their performance from the intrinsic properties of semiconducting, superconducting, and optical materials. Creating devices with improved performance, as well as creating new types of devices, requires an understanding of the fundamental material properties and the methods to actually grow and process these materials. For instance, in charge transport devices like transistors, phenomena such as hot carrier effects become relevant at the small length scales relevant in modern integrated circuits, necessitating new physical models and understanding during miniaturization. Additionally, as researchers seek to push the limits of device performance by reducing signal losses and by using novel materials, new etching and deposition technologies are needed to prepare ultra-high quality thin film materials to fabricate their devices. To this end, this thesis contains work in three facets of solid-state devices: simulation, etching, and deposition.

In Chapter 2, we investigate the hot hole transport properties of silicon via a recently developed *ab-initio* formalism utilizing the Boltzmann transport equation. Hot carrier transport and fluctuations are of critical importance in essentially all modern transistors, and a thorough understanding of the underlying physics is central to their design and operation. In the hot carrier regime, electric fields are sufficiently strong to perturb the electron distribution function such that equilibrium relationships including Ohm's law, the Einstein diffusion relation, and Nyquist noise equation are no longer valid. In this non-equilibrium case, additional microscopic insight may be learned about the material system from the field-dependent mobility, diffusion coefficient, and noise spectrum. Here we develop and apply a first-principles approach to hot carrier transport that does not require any adjustable parameters, facilitating direct comparison to experiment. While this computational method has been applied to electrons in Si and GaAs, we apply it to holes in Si for the first time, calculating the anisotropic DC mobility, diffusion coefficient, and energy relaxation time. Furthermore, we extend the numerical theory underlying the solution to the linearized Boltzmann transport equation to achieve greater accuracy and allow for calculations at cryogenic temperatures. Using this modified theory, we successfully predict experimentally observed phenomena in the cryogenic field-dependent drift velocity and noise spectrum and elucidate their origin from the characteristics of the electron-phonon scattering rates and momentum relaxation time.

Chapter 3 switches focus of the thesis to nanofabrication techniques for thin films; in this chapter we work with a process called atomic layer etching. Although this technique is practically the reverse of atomic layer deposition, which is now common in nanofabrication, atomic layer etching is only a recent development and still in its infancy. The process utilizes sequential, self-limited steps to modify and remove the surface of a material in a precise and controlled manner. Here we report a new process for etching silicon dioxide (SiO_2). This material is common in device fabrication as a dielectric, optical medium, or surface contaminant. Atomic layer etching has the unique properties of smoothing surfaces while exhibiting sub-angstrom precision. To this end, a technique utilizing less-hazardous reactants than prior works and performed using a commercial-scale tool is of interest to improve devices by smoothing SiO_2 interfaces. We develop and demonstrate such a process using trimethylaluminum (TMA) and an argon/sulfur hexafluoride/hydrogen ($Ar/SF_6/H_2$) plasma mixture, demonstrating the process window, step synergy, saturation curves, process parameter dependence, contamination from precursors, smoothing effect, and the influence of SiO_2 deposition method on the etch rate.

In Chapter 4 we turn from etching to deposition techniques. This chapter focuses on a new physical vapor deposition method denoted thermal laser evaporation (also called thermal laser epitaxy). Physical vapor deposition techniques create thin films by the physical diffusion of material vapors onto a substrate. Common techniques included sputtering, electron beam evaporation, molecular beam epitaxy, and pulsed laser deposition. However, all of these come with various limitations. These limits include maximum process pressures, the use of reactive or fragile crucibles, and the maximum temperature of the deposition source. Thermal laser evaporation is an old technique which has long been neglected owing to the limits of laser technology and associated high cost. However, the recent development of 1070 nm fiber lasers has proven to be an enabling technology for this technique. In this chapter, we report the design and demonstration of a home-built thermal laser evaporation system. The system is among the first to be placed into operation in the modern era. We demonstrate its capabilities by evaporating nickel and perform roughness, compositional, and electrical characterization. We discuss lessons learned during system development and comment on both current and future designs.

PUBLISHED CONTENT AND CONTRIBUTIONS

[1] David S. Catherall and Austin J. Minnich. High-field charge transport and noise in *p*-Si from first principles. *Phys. Rev. B*, 107: 035201, Jan 2023. doi: 10.1103/PhysRevB.107.035201. URL https://link.aps.org/doi/10.1103/PhysRevB.107.035201.

D.C. designed the research, conducted the calculations, analyzed the data, and wrote the manuscript.

[2] David S. Catherall and Austin J. Minnich. Hot-hole transport and noise phenomena in silicon at cryogenic temperatures from first principles. *Phys. Rev. B*, 108:235207, Dec 2023. doi: 10.1103/PhysRevB.108.235207. URL https://link.aps.org/doi/10.1103/PhysRevB.108.235207.

D.C. designed the research, conducted the calculations, analyzed the data, and wrote the manuscript.

[3] David S. Catherall, Azmain A. Hossain, Anthony J. Ardizzi, and Austin J. Minnich. Atomic layer etching of SiO2 using sequential exposures of Al(CH3)3 and H2/SF6 plasma. *Journal of Vacuum Science & Technology A*, 42(5):052605, 09 2024. ISSN 0734-2101. doi: 10.1116/6.0003793. URL https://doi.org/10.1116/6.0003793.

D.C. co-designed the research, conducted the calculations, analyzed the data, and wrote the manuscript.

[4] David S. Catherall, Yifei Yan, Finley B. Donachie, Azmain A. Hossain, and Austin J. Minnich. Characterization of ultrathin nickel films deposited by thermal laser evaporation. *Applied Physics Letters*, 128(8): 081902, 02 2026. ISSN 0003-6951. doi: 10.1063/5.0309594. URL https://doi.org/10.1063/5.0309594.

D.C. co-designed the research, designed and co-constructed the experimental apparatus, co-ran the experiments, analyzed the data, and wrote the manuscript.

[5] Ivy I. Chen, Jennifer Solgaard, Ryoto Sekine, Azmain A. Hossain, Anthony Ardizzi, David S. Catherall, Alireza Marandi, James R. Renzas, Frank Greer, and Austin J. Minnich. Isotropic atomic layer etching of MgO-doped lithium niobate using sequential exposures of H2 and SF6/Ar plasmas. *Journal of Vacuum Science & Technology A*, 42(6):062603, 10 2024. ISSN 0734-2101. doi: 10.1116/6.0003962. URL https://doi.org/10.1116/6.0003962.

D.C. participated in devising the experimental methodology and in the analysis of results.

[6] Azmain A. Hossain, Haozhe Wang, David S. Catherall, Martin Leung, Harm C. M. Knoops, James R. Renzas, and Austin J. Minnich. Isotropic plasma-thermal atomic layer etching of superconducting titanium nitride films using sequential exposures of molecular oxygen and SF6/H2 plasma. *Journal of Vacuum Science & Technology A*, 41(6):062601, 09 2023. ISSN 0734-2101. doi: 10.1116/6.0002965. URL https://doi.org/10.1116/6.0002965.

D.C. participated in devising the experimental methodology and in the analysis of results.

[7] Azmain A. Hossain, Sela Murphy, David S. Catherall, Anthony J. Ardizzi, and Austin J. Minnich. Atomic layer etching of niobium nitride using sequential exposures of O2 and H2/SF6 plasmas. *Journal of Vacuum Science & Technology A*, 43(4):042605, 07 2025. ISSN 0734-2101. doi: 10.1116/6.0004548. URL https://doi.org/10.1116/6.0004548.

D.C. participated in devising the experimental methodology and in the analysis of results.

[8] Haozhe Wang, Azmain Hossain, David Catherall, and Austin J. Minnich. Isotropic plasma-thermal atomic layer etching of aluminum nitride using SF6 plasma and Al(CH3)3. *Journal of Vacuum Science & Technology A*, 41(3):032606, 05 2023. ISSN 0734-2101. doi: 10.1116/6.0002476. URL https://doi.org/10.1116/6.0002476.

D.C. participated in devising the experimental methodology and in the analysis of results.

TABLE OF CONTENTS

LIST OF ILLUSTRATIONS

LIST OF TABLES

Chapter 1

INTRODUCTION

Perhaps the most defining feature of technological development within the last 120 years has been the development of computing technologies, starting with the invention of the most basic transistor, the vacuum tube. Developments since have included the invention of electronic components, miniaturization, and the discovery or integration of novel materials. Underlying all of these advances has been four key tools: simulation, patterning, etching, and deposition. Advancements in each tool has led to advancements in one or more of the three major technological developments. Each tool is indispensable, and in this thesis we will discuss all but patterning, though it is no less deserving of study.

Fabricating devices with improved performance and creating new types of devices both require a thorough understanding of the intrinsic properties of the materials used. For instance, at the macroscopic level the behavior of integrated transistors is determined by charge transport phenomena which can generally be understood through average quantities and simple or empirical equations. At these scales, transport is affected primarily by material properties such as composition, thickness, and doping. However, in applications at very small scales (less than electron mean free path) or large electric fields ($\gtrsim$ 1 kV cm^{-1} at room temperature), and especially where noise is important, the necessary physics to predict behavior become even more complicated as a microscopic understanding of charge transport is required. For example, Moore's law has begun to reach its end owing to physics such as quantum tunneling, which only becomes important at nanometer scales. While advances in device packaging and 3D architecture may keep overall transistor density increasing, we are fast approaching physical limits for planar transistor density. Pushing these boundaries any further requires a precise understanding of material properties and behavior not currently available in the simulations used to design these devices.

Additionally, as semiconductor companies seek to increase device yield and reliability and researchers push the limits of device performance by reducing signal losses, new etching techniques are required with novel characteristics. Etching is a critical step in the fabrication of practically any device, whether it utilizes the

transport of electrons and holes (semiconductors), Cooper pairs (superconductors), or photons (optical). The typical fabrication pipeline starts with the deposition of one or more materials, patterning, and the etching of some number of the deposited layers. This is usually followed up with more etching, patterning, and deposition steps to make a functional device. The current state-of-the-art in materials etching is split into two categories: wet and dry. Wet etching is a relatively simple process in which the material is placed in a solution which contains an etchant. Wet etch parameters include the etch bath chemistry, temperature, and time. Wet etching is notoriously difficult in practice, though, for multiple reasons: obtaining perfect uniformity requires removing the etchant in a uniform manner, which is practically impossible for modern substrates with sizes in excess of 6 inches, *in-situ* monitoring is difficult or impossible, it is an *ex-situ* process, and etching reactions can have products which make control of the etch rate or small-scale uniformity challenging. Dry processes, on the other hand, take place under vacuum and the etchant takes the form of either reactive gas species such as chlorine and oxygen, high-energy plasmas, or some combination thereof. In dry processes, no liquid phase is used (hence the "dry" moniker, even though water vapor may be used). Dry etching features more parameters than wet etching, including the gas chemistry, pressure, ion energy, table bias, temperature, and time. Dry etching, however, has a relatively limited set of chemistries and if a plasma is required, will always have some anisotropic character (which may be desirable). While dry etching has advantages including amenability towards *in-situ* monitoring and producing less-problematic reaction products, it lacks the fine control or selectivity that cutting-edge device fabrication demands. Furthermore, dry plasma etching often leads to significant (sub)surface damage which may decrease device performance.

Lastly, as researchers continue to develop or discover new materials, whether suitable for devices or having their own interesting properties to study, deposition techniques need to develop to deposit them. Today, techniques fall into two main categories: chemical and physical. Chemical techniques rely upon chemical reactions at the substrate surface to deposit the material of interest. However, it is generally limited by the available chemistries: not every material has precursors which react on the substrate surface within the thermal budget available or leave a pure high-quality film behind. Physical deposition techniques are much less burdened by chemistry, relying instead on the vaporization of one or more elemental constituents which condense on the substrate to form the desired film. Vaporization techniques vary widely and include plasma bombardment, laser ablation, and evaporation through

electric currents, resistive heating elements, or electron beams. Each technique has advantages and disadvantages, however, there exist certain materials which no technique is able to deposit a film of reliably. These films include refractory or highly reactive elements, which are increasingly of interest in the exotic films envisioned by materials scientists. Therefore, a technique which reliably deposits these problematic materials is desirable.

1.1 Simulation: Hot carrier transport

The fundamental equation most common among anyone familiar with electricity is, of course, Ohm's law:

$$V = IR \tag{1.1}$$

which represents a linear relationship between voltage and the resulting current in a circuit, mediated by the resistance. This equation generally holds at the voltages and temperatures employed with macroscopic electronics. Other linear relationships also exist which hold similar validity, including the Einstein relationship, which links the diffusivity of charge carriers to their mobility:

$$D = \frac{\mu_q k_B T}{q} \tag{1.2}$$

where μ_q is the carrier mobility, k_B is the Boltzmann constant, T is the temperature, and q is the carrier charge. Another quantity of interest is the current noise, which manifests as spontaneous, random fluctuations in the measured current. To quantify these random fluctuations, the power spectral density (PSD) can be used, which represents the power of the noise at a given frequency. This can be calculated using the Johnson-Nyquist noise relation:

$$S_j(\omega) = 4k_B T \ \mathrm{Re}[\sigma_{AC}(\omega)] \tag{1.3}$$

where $S_j(\omega)$ is the spectral power density of current fluctuations, ω is the angular frequency, and $\sigma_{AC}(\omega)$ is the AC conductivity.

Underlying these three equations and all other "equilibrium" charge transport relationships is the assumption that the charge carriers are in thermal equilibrium within their host system. In the case of semiconductors, this means that the carriers are always in equilibrium with the crystal lattice. In these cases, the carrier distribution is negligibly altered from the Fermi-Dirac distribution:

$$\overline{n}_\lambda = \frac{1}{e^{(\epsilon_\lambda - \mu)/k_B T} + 1} \tag{1.4}$$

where $\overline{n}_\lambda$ is the mean carrier occupation of the electronic state λ, ϵ_λ is the state energy, and μ is the Fermi energy. Therefore, in this case transport properties are simply derived from a small perturbation of the equilibrium distribution.

However, this assumption is not always valid. When carriers are subject to a sufficiently strong electric field (for instance, at room temperature in silicon this is about 1 kV cm^{-1}), charge carriers are accelerated so rapidly that the distribution shifts anisotropically towards higher energies. Once carriers have excess effective temperature (ΔT) comparable to the lattice temperature ($\Delta T/T \sim 1$), carriers access different scattering mechanisms than those available at equilibrium (when $\Delta T/T \ll 1$). Thus, not only is the fluctuation-dissipation theorem [1, 2] violated (which normally relates transport properties of fluctuation and relaxation because the underlying physical mechanisms by which they occur are the same), but even the most basic equilibrium equations like Ohm's law lose validity. For instance, at high fields the current changes nonlinearly with voltage and may even depend on crystalline orientation with respect to the applied electric field, even in cubic crystals [3]. At these fields, qualitatively new information may also be obtained from noise quantities such as the current PSD, owing to the breakdown of the Einstein [4] and Nyquist equations [5]. Additional interesting phenomena such as drift velocity saturation and negative differential resistance may also occur [6–8]. This phenomenon is commonly referred to as "hot carrier transport", so named because the carriers are "hotter" than the lattice. In this regime, properties like the diffusion coefficient differ from the mobility, yielding new information about the material system when examined as a function of electric field strength [5, 9–12].

Hot carrier transport has long been of interest for its uses in devices, to avoid its effects in devices, and as a tool to probe semiconductor physics. As semiconductor devices become smaller, hot carriers are increasingly relevant as device operating voltages have remained largely the same while dimensions have shrunk dramatically, increasing the electric fields involved. Sometimes hot carrier effects can be beneficial; in some materials (e.g. GaAs) hot electrons scatter between states with substantially different effective masses, yielding negative differential resistance which is of use in devices such as the Gunn diode [13]. On the other hand, effects such as hot-carrier injection, in which a carrier gains enough energy to tunnel through energy barriers, is a major problem in modern integrated circuits, causing leakage current in devices such as MOSFETs [13]. However, because hot carriers by their nature interact with both the host lattice and with the electric field in different

ways than at equilibrium, the study of their behavior has been important for the understanding of semiconductor physics [10]. Alternatively, simulating hot carrier behavior and comparing to experiments is a means to test our current understanding of physics.

Owing to the importance of hot-carrier transport for both devices and physics (particularly electron-phonon scattering), the calculation of properties from first principles (*ab-initio*) is of interest [14–18] as this method is inherently connected to our ability to describe the underlying transport physics. Historically, and even today, empirical models are often used to simplify calculations, but without a physical basis these models do not have strong predictive capabilities, relying on free parameters which must be fit to experiments. By extension, they cannot be used to probe the underlying physics behind emergent phenomena such as carrier mobility since the mathematics may contain little physical meaning. While the *ab-initio* method was out of reach during the time in which much of our understanding of hot carrier transport was developed, recent advances have made the computations feasible. Now, the calculation of phonon-limited mobility is possible without adjustable parameters through density functional theory (DFT), density functional perturbation theory (DFPT), Wannier interpolation to fine grids needed for transport calculations, and the Boltzmann transport equation (BTE) [17, 18]. Implementations of this approach are now available in various software packages [19–23], and have been applied to calculate low-field properties in a number of materials such as Si [24–26] and GaAs [26–28], 2D materials including graphene [29–32] and MoS_2 [24, 31–34], and others [16]. The approach continues to develop, with advances in the *ab-initio* description of two-phonon scattering [35], neutral and ionized impurity scattering [36, 37], quadrupole interactions [38, 39], and other physics [40, 41].

Because charge transport in polar materials is more physically complex than in non-polar ones, we will focus here on non-polar semiconductors. In these materials, high-field effects were first experimentally observed as a departure from Ohm's law in Ge and Si [42–45]. The time-of-flight (TOF) technique was the first by which hot carrier transport could be quantitatively studied, in which carriers are injected into a material and their arrival at a spatially distant extraction point is monitored. This technique allowed the hot-carrier drift velocity to be measured, revealing high-field effects including anisotropy, drift velocity saturation, and negative differential resistance in *n*-Si [8] and *p*-Si [7, 46–48]. The TOF technique has also been used to measure fluctuation quantities such as the charge carrier diffusion coefficient [6, 49–

51]. Contemporaneous developments measuring the spectral noise power of current fluctuations also allowed for the determination of noise temperature [52, 53] and provided a second means for evaluating the diffusion coefficient [50, 51, 54, 55] using the fluctuation-diffusion relation [56]. Measurements at cryogenic temperatures have also found that non-Ohmic behavior becomes more apparent as temperature decreases [57–59].

Various theoretical and numerical methods have been employed to interpret these measurements in terms of microscopic transport processes [6, 10, 60–62]. For instance, Monte Carlo (MC) methods have long been employed to study high-field transport phenomena in *p*-Si [14] which have investigated both steady-state [63–66] and fluctuation phenomena [48, 50, 67]. These simulations function by simulating some number of discrete particles over time as they move through a system, using random number generation to simulate probabilistic events such as scattering. Monte Carlo simulations are useful when analytically or numerically solving the equations underlying carrier transport (e.g. the BTE) are difficult. However, while MC simulations have the distinct advantage of treating realistic device geometries [68, 69], something difficult to achieve with approaches such as solving the BTE, they often employ semi-empirical approximations for the band structure and scattering rates. Some recent works have employed full-band calculations which partially relax prior approximations [70–74], and applied them to various materials including *p*-Si [75–80]. However, no MC study on *p*-Si has employed a fully *ab-initio* band structure and scattering rates.

The fully *ab-initio* treatment of electron-phonon scattering [17, 18, 81] has recently been used to calculate low-field hole transport properties in silicon [82, 83]. These works found that *ab-initio* calculations with one-phonon scattering, spin-orbit coupling, and the relaxation time approximation is generally adequate to predict the low-field mobility. Overestimates of the mobility of around 30% were attributed to inaccuracies in the DFT valence band structure. At high fields, recent works have extended the *ab-initio* method to study high-field transport phenomena and noise [84–88].

High-field transport calculations offer a stricter test of the theory because band anisotropy, intervalley and interband scattering, and energy relaxation take on increased importance [10, 12, 89, 90]. The main difference between high and low-field calculations is the treatment of the momentum-space derivative of the deviational occupancy, which we show in Fig. 1.1. The methodology here uses a finite differ-

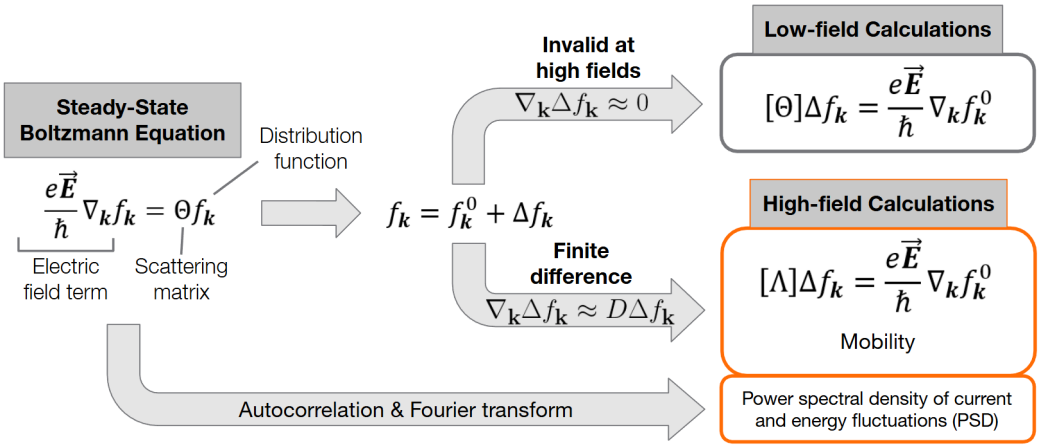

Figure 1.1: Schematic overview of charge transport BTE calculations. The BTE for a steady-state system of charge carriers under an electric field is given on the left. In the center is the form of the solution: the steady-state distribution function can be split into equilibrium and deviational components. Then, the treatment of the gradient of the deviational component determines validity at high fields. The treatments indicated within the arrows yield the BTE shown on the right, which can be used to calculate quantities such as the mobility. Noise quantities can be similarly calculated.

ence matrix to approximate a term which is typically neglected in low-field studies, permitting an approximation to the full solution to the BTE when the occupation function deviates from equilibrium due to a strong electric field.

Recent findings with the *ab-initio* methods include the importance of two-phonon scattering in GaAs [35, 85] and Si [86, 87] as well as the discovery of simultaneously high electron and hole mobilities in BAs [91–93]. However, recent methods for the *ab-initio* treatment of high-field transport [84–88] have not yet been applied to *p*-type semiconductors.

1.2 Etching: Vacuum etching techniques

Etching is a subtractive process in which material is removed from a substrate or film through physical or chemical means. Etching requires an etchant, typically a reactive chemical or energy source (usually ions), to remove material at a solid-liquid or solid-gas/plasma interface. A representative schematic of an etch process is shown in Fig. 1.2, in which a solid film is exposed (Fig. 1.2a) to a reactive chemical. The etchant adsorbs onto the surface (Fig. 1.2b) and reacts with it, forming a volatile or soluble compound which subsequently desorbs (Fig. 1.2c). Further exposure to the etchant continues the process (Fig. 1.2d), deepening the etch for as long as the

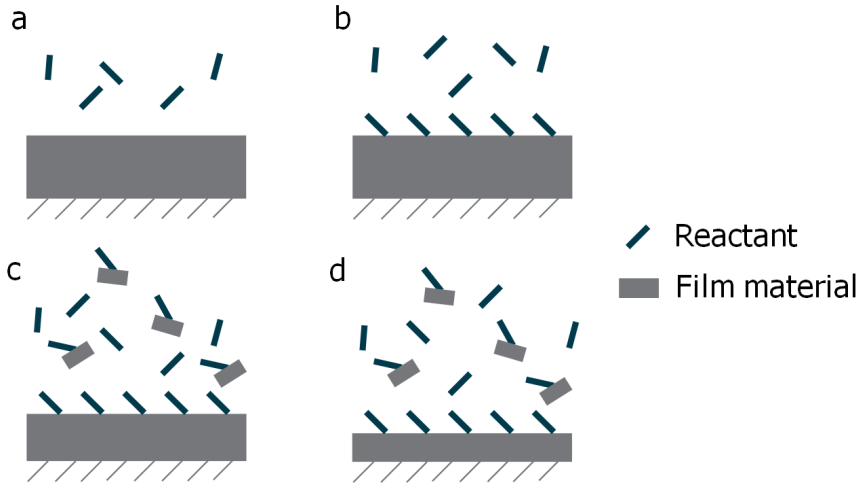

Figure 1.2: Schematic of a continuous etching process. (a) A film which is about to be exposed to an etchant. (b) The etchant adsorbs on the surface. (c) The etchant reacts with the film material and desorbs. (d) The etchant continues to react with the film and remove material for the entire duration of exposure.

material and etchant are in contact.

Subtractive processing is a critical step in the fabrication of practically any microdevice, whether it utilizes the transport of electrons and holes (semiconductors), Cooper pairs (superconductors), or photons (optical). In a typical fabrication pipeline, the process starts with the deposition of one or more materials on a substrate, followed by patterning, and then etching of some number of the deposited layers. This sequence is usually followed up with more etching, patterning, or deposition steps to make a functional device.

The current state of materials etching is split into two categories: wet and dry [94, 95]. In wet etching, the material is placed in a solution in which the etchant is dissolved. The process works exactly as shown in Fig. 1.2, where the dissolved etchant reacts with the solid material to form soluble products. Wet etching is attractive in its simplicity: it features only a few variables which need to be controlled (the etch bath chemistry, temperature, and time), and also features a very large range of chemical etchants to provide the necessary etch rate or selectivity. However, wet etching has a few notorious drawbacks: uniformity over large substrates ($\gtrsim$ 6 in) is practically difficult for rapid etches since the etchant cannot be uniformly removed with sub-second accuracy, *in-situ* monitoring is difficult or impossible, reaction products may affect the reaction, sensitivity to stirring and evaporation, and the majority of processes result in an isotropic etch (meaning the etch proceeds equally

in all directions). These issues mean many devices are not possible to fabricate using wet etching, particularly when sub-nanometer control is desired without the use of an etch-stop layer.

Dry processes, on the other hand, typically take place under vacuum and the etchant takes the form of either reactive gas species such as chlorine or oxygen, plasmas, or some combination of the two [94–96]. In dry processes, no liquid phase is used (hence the "dry" moniker, even though water vapor may be a part of the process). Dry etching has a number of advantages over wet etching, some of which are as follows: Dry etching is more amenable towards *in-situ* monitoring since the surface is completely exposed. The reaction products of dry etching are typically volatile and do not interfere with the reaction. Dry etching offers a larger number of variables than in wet etching, including the gas chemistry, pressure, ion energy, plasma power, the type of plasma source, table bias, temperature, and time. The lack of a liquid phase also allows for processing at both very low and very high temperatures (typically between $-150\,^{\circ}\mathrm{C}$ and $400\,^{\circ}\mathrm{C}$). Owing to its versatility and widespread use, we will focus the remainder of this discussion on dry etching.

The simplest form of dry etching is exposing a material to a gaseous etchant. For instance, silicon is etched by exposure to XeF_2 vapors [97], a process common in the fabrication of micro-electro-mechanical systems (MEMS). In this process, XeF_2 adsorbs onto the silicon surface and reacts to form Xe and SiF_4, both of which are volatile and quickly desorb. Furthermore, this reaction does not occur for the compounds of silicon including SiO_2, Si_3N_4, or SiC, meaning that patterns can be transferred into the silicon by using a mask of these materials. Because of the gaseous nature of XeF_2, the etch also proceeds isotropically, meaning it does not only etch down into the material but also underneath any mask that is present. This allows for undercuts or even the full release of structures built up on a silicon base layer [95], a necessary feature for MEMS devices.

A slightly more complex form of this method is the incorporation of plasma products. For instance, one can use a plasma containing chlorine gas to create highly reactive chlorine radicals for use as an etchant. In this case, the kinetic energy of plasma species plays no direct role in etching, but the plasma provides chemical species useful for etching reactions [98] (including radicals, ions, metastable species, and electrons). Sometimes these species are stable enough that the plasma can be placed so remote from the processing chamber that no charged species interact with the substrate at all, which can be advantageous as some plasma species may damage

exposed materials [96]. This latter remote-plasma process is often employed using oxygen as a source gas for stripping residual lithography resists, but is sometimes also employed for etching functional materials such as polysilicon [99].

There also exists a form of etching that does not require chemical reactions. This technique, termed ion milling [95, 96, 98], uses a plasma electrically biased against the table on which the substrate is placed. The resulting electric field causes ions generated in the plasma to be accelerated towards the substrate. These ions, typically in the form of ionized noble gases (e.g. Ar), bombard the material surface with enough kinetic energy to break bonds and release atoms or molecules of the solid material. Ion milling, unlike the techniques discussed previously, is anisotropic, meaning the etch proceeds primarily in a single direction. This feature allows for the fabrication of high aspect ratio features and accurately transferring a pattern from a lithographic mask into the underlying material without an undercut. However, it has a few notable drawbacks. First, because the solid material released by the ions has not been chemically altered, it often falls back onto the material surface and redeposits, degrading the quality of the etch. Second, the ions cause a large disruption in the crystal lattice where they hit the material surface. While this may be useful for etching as it weakens the existing surface bonds for subsequent removal by other ions, the final surface after etching is typically amorphous and this can induce losses in device performance. Third, because chemistry is not involved, this technique is largely non-selective meaning that it will etch both material and mask layers alike. Therefore, it is used only in unusual cases.

Reactive ion etching (RIE) is a combination of physical and chemical dry etch processes. In this case, species are introduced (either gas species or plasma products) which react with the material surface in conjunction with ion bombardment [96, 98]. The reacted material has a decreased binding energy to the material surface, requiring less kinetic energy from the ions to remove. A famous example is the Bosch process [100], which is a specialized version of this technique for highly anisotropic silicon etching. RIE is now so ubiquitous that it is nearly synonymous with dry etching. However, RIE lacks atomic-scale fidelity, results in plasma-induced surface damage, and can increase the surface roughness, placing limits on the achievable device quality.

Despite the wide variety of processes available between wet and dry etches, there are desired etch processes which have not yet been developed. For instance, some materials, such as lithium niobate, are notoriously difficult to etch owing to their

physical and chemical stability. In fact, until recently, the only means of etching this material for optical devices was ion milling. This technique, however, lacks the fine depth control necessary to reliably fabricate devices based on lithium niobate [101, 102]. Similarly, optical devices made from other materials including SiO_2 or Si_3N_4 require incredibly smooth (sub-nm roughness) sidewalls to avoid optical losses. Current etching techniques typically result in a sufficiently rough surface that optical losses from these imperfections are measurable and mitigation is an area of active research [103–106]. Therefore, etch techniques which smooth out surfaces would be of great interest in the optical device community.

Other types of devices, such those based on superconductors, are also prone to losses from the surface regions of their active materials. In this case, native oxides and damage induced by processing give rise to loss mechanisms such as two level systems. Ideally, an etch with fine depth control and without damaging the superconducting material could be used along with an encapsulation process to improve the noise performance of these devices [107, 108]. Finally, some devices such as high-electron-mobility transistors are incredibly sensitive to film thickness and etch damage. Therefore an damage-free etch process with precise sub-nm control is needed to improve both the functionality of these devices as well as the reliability of fabrication [109]. A process which exhibits excellent selectivity, precision, and smoothing would solve many of these problems [96].

1.3 Deposition: Physical vapor deposition

The simplest form of physical vapor deposition (PVD) is the evaporation and condensation of material. This technique utilizes thermal energy to sublimate or evaporate an element in vacuum, allowing the vapors to diffuse to the substrate where they condense and form a film [94, 95, 110]. Deposition material typically comes in the form of elementally pure pieces, which are loaded into a crucible made of either high-temperature ceramic (such as alumina or boron nitride) or refractory metal (such as tungsten or tantalum). While providing the needed thermal energy through resistive elements is possible, the preferred method to is to use a beam of electrons. This technique is called electron beam evaporation (E-beam). A schematic E-beam source is shown in Fig. 1.3a. The electron beam is supplied via a high-voltage power source and it is directed at the material surface through electron optics. This redirection is critical so that the electron beam source does not have line-of-sight to the deposition source, which would result in deposition on the beam source. Because electrons are charged particles, a local electric field will form on the deposition

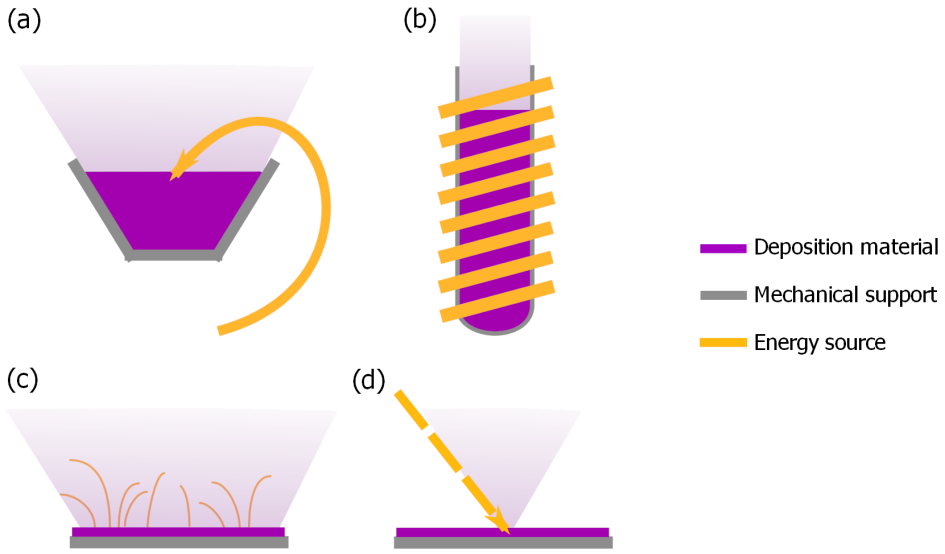

Figure 1.3: (a) An electron-beam evaporation source, which uses a directed beam of high-energy electrons to heat material held in a crucible. (b) An MBE effusion cell, consisting of a crucible heated by resistive coils. (c) A sputtering deposition source, which utilizes a plasma to bombard the surface with high-energy ions with sufficient kinetic energy to liberate material for deposition. (d) A PLD deposition source, which uses a pulsed laser to ablate material.

source where the beam impinges upon it, repelling the beam. This is typically dealt with by scanning the beam around the surface of the deposition source, which also aids in temperature uniformity. The use of a beam of electrons also means the maximum source temperature is limited only by the crucible and power output of the electron source. The major disadvantage of E-beam systems is that they are typically not constructed to deposit multiple elements simultaneously, nor are they used for reactive deposition with a background gas.

Where precision crystalline growth of compounds is required, molecular beam epitaxy (MBE) is employed [110, 111]. Chemical deposition techniques are also often used for this purpose, but for this thesis we limit the scope of our discussion to physical deposition. A schematic of an MBE source is shown in Fig. 1.3b. The main difference between MBE and E-beam lies in the energy source: rather than use a high-energy beam of electrons, MBE systems use a resistively heated coil. Furthermore, the source geometry also differs significantly: E-beam sources have a width comparable to their depth and the resulting flux has a wide solid angle. In MBE systems, crucibles are often many times deeper than they are wide. This difference means that E-beam source flux is widely dispersed through the chamber

above while MBE cells have a restricted solid angle resulting in a "molecular beam". Multiple MBE sources are used simultaneously to form compounds, and non-solid (such as oxygen) or high-vapor pressure materials (such as arsenic) can be incorporated through background gases, plasma sources, or specialized sources. This deposition method is typically used for ultra-pure epitaxial growth, utilizing very slow deposition rates (at or below a single monolayer per second) and heated substrates. MBE is unique in that the process may be tuned to be driven by kinetics rather than thermodynamics, allowing for the growth of metastable compounds.

While MBE and E-beam are capable of depositing many different materials, they are still limited by large-scale uniformity (e.g. wafers over 6 inches in diameter) and by the need for multiple sources to deposit compound materials. If one were to put a compound in an MBE or E-beam deposition source, the different constituents will most likely exhibit different vapor pressures and evaporate at different rates, forming a non-stoichiometric compound on the substrate. Sometimes this can be worked around, especially in the case of oxides, by introducing more of the limiting constituent through another source (such as oxygen gas when evaporating an oxide). However, for many compounds with multiple metallic elements this is not possible.

These limits can be worked around by turning to non-thermal techniques. The most common of these PVD methods is sputtering, which today is ubiquitous from research laboratories to the largest-scale semiconductor manufacturing facilities [94, 95, 110]. A schematic of sputtering is shown in Fig. 1.3c. In a sputtering process, a flat target comprised of a mechanical support, interfacial layer(s), and the material to be deposited is placed on top of a plasma source. Typically, the plasma source is coupled with a magnet to both confine the plasma ions close to the surface of the target and to distribute ion impingement as evenly as possible. Once a plasma is struck, ions are accelerated towards the surface of the target where they impart sufficient kinetic energy to liberate atoms of the material into the surrounding vacuum, where they subsequently diffuse towards the substrate.

Sputtering has a number of significant differences from the two PVD methods discussed previously:

1. Owing to its non-thermal nature, compounds can be deposited while preserving stoichiometry. Where stoichiometry is known to change from the deposition source to the deposited film, reactive deposition, cosputtering, or superstoichiometric targets are sometimes used to compensate.

2. Because a plasma in necessary to provide flux, the process requires medium vacuum (1-10 mTorr). To avoid contamination, the plasma gas (typically argon) must be refined to exceptional purity, but even still, argon itself may be incorporated into the deposited film.

3. A significant amount of time is often necessary to "burn out" the target, not just removing the native oxide and contaminating material, but also bringing its surface into a steady state.

4. Sputtering deposition tends to be isotropic, meaning that all surfaces get coated evenly. This may be advantageous for various device processing steps since 3D structures can be coated uniformly, but makes lift-off processing more difficult since a continuous film forms over the mask. This feature stems from two aspects: First, sputtering targets are typically many inches in diameter, sometimes even larger than the substrate itself, meaning deposition may come from a wider range of angles than the nearly point-source nature of MBE or E-beam sources. Second, the relatively high operating pressures compared to MBE and E-beam results in the mean free path of sputtered material being smaller than the distance from the material source to the substrate. This results in scattering events which randomize the incident angle of deposition.

For highly complex compounds containing constituents with dramatically different sputtering rates, or where fine tuning of the film properties is required, pulsed laser deposition (PLD) can be used [112]. A schematic PLD source is shown in Fig. 1.3d. Like sputtering, PLD is a non-thermal process. However, instead of using ion bombardment from a plasma to liberate the source material from a target, PLD utilizes high-energy laser pulses to ablate material. These pulses have sufficiently large energies and short pulse-widths that the differential vapor pressures of the source constituents do not practically matter. Because the deposition source is a point source, under UHV this method shares the non-conformal nature of MBE and E-beam.

However, this method is prone to two major issues: First, the ablation process does not guarantee that the ejected material will be atomic or molecular, and it may include large particles that settle on the substrate surface [113, 114]. Second, because light cannot be redirected (at the laboratory scale) without a physical medium, the final optic in the vacuum system will by necessity have direct line-of-sight to the deposition source. Therefore, the final optic (typically a window) will be deposited

upon and its performance will slowly degrade, necessitating regular maintenance [115].

While other PVD techniques exist, the four discussed here are the techniques primarily used by researchers and industry alike to create semiconducting, superconducting, and optical devices. Each technique has its advantages and disadvantages; however some gaps remain in the capabilities of all these techniques together. Currently, practical deposition of refractory metals and their compounds is only possible by sputtering, as it does not require heating the material to within its melting point. However, because sputtering involves the use of a plasma, the resulting film may be damaged by charged particles or high energy photons. The isotropic nature of sputtering also makes lift-off of these films difficult. MBE cannot reach the temperatures necessary to fabricate refractory metal and compound films without destroying the resistive heaters or the crucibles themselves. E-beam systems, while capable of arbitrary source temperatures in theory, pose challenges related to avoiding damage to the crucible, the crucible material evaporating, and the crucible reacting with the source material or diffusing contaminating material into it. At high powers, E-beam systems can also generate a significant amount of x-ray radiation which may damage the device being fabricated [95]. Furthermore, both MBE and E-beam systems are limited in both the maximum background pressure and what background gases are permissible for reactive deposition due to the mean free paths required and the heated elements. Therefore, prior to the recent development discussed here there is no easy means to deposit refractory metals or their compounds.

1.4 Outline of thesis

In this thesis we further develop the tools for understanding and predicting material behavior through *ab-initio* calculations. Further, we expand the methods for fabricating real devices through the development of a novel atomic layer etching recipe and the construction and demonstration of a thermal laser evaporation system.

In Chapter 2, we improve upon and employ a recently developed *ab-initio* formalism to simulate hot carrier transport in semiconductors by applying it to holes in silicon (*p*-Si). In our approach, we develop and apply a first-principles approach to hot carrier transport that does not require any adjustable parameters, facilitating direct comparison to experiment. In the hot carrier regime, electric fields are sufficiently strong to perturb the electron distribution function such that equilibrium relationships including Ohm's law, the Einstein diffusion relation, and Nyquist noise

equation are no longer valid. Therefore, another technique is needed to predictive simulations of material and device behavior. Our method utilizes the Boltzmann transport equation, which describes the evolution of the charge carrier distribution function under external fields and gradients and retains validity so long as transport is semi-classical. Taking as inputs a set of electronic states, their group velocities, and scattering information from DFT and DFPT, a set of linear equations are solved for the high-field transport and noise properties. In this non-equilibrium case, additional information can be learned about the material system from the field-dependent mobility, diffusion coefficient, and noise spectrum.

While the computational method employed here has been applied to electrons in Si and GaAs, we apply it to holes in Si for the first time, calculating the anisotropic DC mobility, diffusion coefficient, and energy relaxation time without adjustable parameters and up to 20 and 12 kV cm^{-1} and temperatures of 300 and 77 K. At these temperatures we find that the calculated properties quantitatively reproduce the trends of high-field transport including the electric field-dependence and anisotropy of the mobility and PSD, and the rapid variation of energy relaxation time with electric field at cryogenic temperatures. We also find that the absolute transport properties are uniformly overestimated by around $\sim 25\%$, consistent with the origin being inaccuracies in the valence band structure.

Furthermore, we extend the theory underlying solving the linearized Boltzmann transport equation to achieve greater accuracy and allow for calculations at cryogenic temperatures down to 6 K. Using this modified theory, we reproduce experimentally observed phenomena in the cryogenic field-dependent drift velocity and noise spectrum and provide new physical mechanisms for their occurrence. We show that the additional drift velocity saturation regime arises from scattering dominated by acoustic phonon emission. For the PSD, we find that the peak occurs due to the decrease of the momentum relaxation time with increasing electric field, an explanation not given in prior literature. This low-temperature investigation proves an important value of *ab-initio* calculations beyond just its predictive abilities: this technique yields more information about the system than could be realistically accessed in experiments. This knowledge allows for a thorough analysis regarding the mechanisms behind experimentally observed phenomena, an understanding of which is critical for accurate device simulation.

Chapter 3 and beyond switches focus to nanofabrication techniques for thin films. In this chapter, the focus is on the improvement of etching techniques through atomic

layer etching, which is practically the reverse of atomic layer deposition. Whereas in plasma and wet etching techniques the material is continually etched for as long as it is exposed to the etchant, atomic layer etching utilizes multiple steps to remove material. These steps are necessarily self-limiting; they react with the material to a specific depth (typically a monolayer) and no more. Atomic layer etching typically consists of a modification step to change the surface chemistry, and removal step which volatilizes the modified surface. In this chapter we report a new process for etching silicon dioxide, or silica. This material is common in device fabrication as a dielectric, optical medium, or surface contaminant. Atomic layer etching has unique properties among etching techniques including smoothing surfaces and repeatable sub-angstrom precision. However, previous recipes to etch silica entail the use of HF vapor, which is both difficult and dangerous to work with, and generally incompatible with commercial-scale tools capable of handling multi-inch wafers. To this end, a recipe utilizing less-hazardous precursor materials and performed using a commercial tool is of interest to improve devices by smoothing silica interfaces. We develop and demonstrate such a process using trimethylaluminum and sulfur hexafluoride plasma, demonstrating the process window, step synergy, saturation curves, process parameter dependence, contamination from precursors, smoothing effect, and the influence of silica deposition method on etch rate.

In Chapter 4 we turn to a technique for the deposition of novel materials, denoted thermal laser evaporation (TLE). While traditional PVD techniques rely on energetic plasmas, resistive heaters, or high-voltage electron beams, thermal laser evaporation uses laser light to evaporate material. This technique differs from pulsed laser deposition in that the laser power is continuous; the material is evaporated thermally, not through rapid ablation. While current PVD techniques have limitations including process pressures, the use of reactive crucibles, and most notably the maximum temperature of the deposition source, thermal laser evaporation (or epitaxy) either lacks these drawbacks or otherwise improves on them, making it an attractive alternative for the future of semiconducting, superconducting, and optical device fabrication. While the technique has a history spanning over sixty years, it has long been neglected owing to the limited power and high cost of short-wavelength lasers. However, the recent development of fiber lasers (1070 nm wavelength) has proven to be the enabling technology for this technique, as demonstrated by recent works. In this chapter we review the construction of the first modern TLE system in the US, discuss current and future design choices, and demonstrate the system by evaporating a nickel film. We characterize the resulting film with compositional,

roughness, and electrical analysis.

In Chapter 5 we summarize this research and present directions for further work.

Chapter 2

AB-INITIO HOT HOLE TRANSPORT IN SILICON

This chapter has been adapted from

David S. Catherall and Austin J. Minnich. High-field charge transport and noise in p-Si from first principles. *Phys. Rev. B*, 107: 035201, Jan 2023. doi: 10.1103/PhysRevB.107.035201. URL https://link.aps.org/doi/10.1103/PhysRevB.107.035201.

D.C. designed the research, conducted the calculations, analyzed the data, and wrote the manuscript.

David S. Catherall and Austin J. Minnich. Hot-hole transport and noise phenomena in silicon at cryogenic temperatures from first principles. *Phys. Rev. B*, 108:235207, Dec 2023. doi: 10.1103/PhysRevB.108.235207. URL https://link.aps.org/doi/10.1103/PhysRevB.108.235207.

D.C. designed the research, conducted the calculations, analyzed the data, and wrote the manuscript.

2.1 Introduction

The linearized Boltzmann transport equation

The Boltzmann transport equation (BTE) has long been the gold standard by which charge transport in semiconductors is understood. In its full form it can describe the time-dependent behavior of a system of particles subjected to both external forces and internal interactions, and is expressed as [14, 116–118]:

$$\frac{\partial f}{\partial t} + \mathbf{v}\nabla_{\mathbf{r}} f + \mathbf{F}\cdot\nabla_{\mathbf{p}} f = \left(\frac{\partial f}{\partial t}\right)_{coll} \tag{2.1}$$

where f is the space, momentum, and time dependent function describing the occupation of states, $\mathbf{v}$ is the velocity, $\nabla_{\mathbf{r}}$ is the gradient in space, $\nabla_{\mathbf{p}}$ is the gradient in momentum, $\mathbf{F}$ is the external force, and $\left(\frac{\partial f}{\partial t}\right)_{coll}$ represents the effect of particle scattering. We can simplify this expression when considering a system of charge carriers. First, the force exerted on a charged particle in an electric field $\mathbf{E}$ is simply $\mathbf{F} = q\mathbf{E}$, and the momentum can also be expressed in terms of wave vector $\mathbf{k}$ through the de Broglie relation $\mathbf{p} = \hbar\mathbf{k}$, where $\hbar$ is the reduced Plank constant, meaning $\nabla_{\mathbf{p}} = \nabla_{\mathbf{k}}/\hbar$. Second, we may also assume spatial homogeneity; while this

means real devices are out of reach for these calculations, the assumption enables computational tractability while the underlying materials physics remains largely the same in experiment where samples are sufficiently large to ignore size effects. With these changes we can express the spatially homogeneous charged particle BTE as:

$$\frac{\partial f_\lambda}{\partial t} + \frac{q}{\hbar}\mathbf{E}\cdot\nabla_{\mathbf{k}} f_\lambda = \left(\frac{\partial f_\lambda}{\partial t}\right)_{coll} \tag{2.2}$$

where we now express the distribution function as f_λ, recognizing that it is only a function of λ, which represents the electronic state (which itself is determined by the wave vector and band index). Because time-dependent transport property data are scarce compared to the steady-state, we will neglect time-dependence and set $\partial f_\lambda/\partial t = 0$, which also decreases computational complexity. We may further refine the left hand side of Eq. (2.2) by breaking apart the vectorized terms into cartesian components:

$$\frac{q}{\hbar}\mathbf{E}\cdot\nabla_{\mathbf{k}} f_\lambda = \sum_\gamma \frac{qE_\gamma}{\hbar}\frac{\partial f_\lambda}{\partial k_\gamma} \tag{2.3}$$

where γ represents the cartesian directions. We also replace the collision term with the collision integral $I[f_\lambda]$ [118] to get a simplified version of Eq. (2.2):

$$\sum_\gamma \frac{qE_\gamma}{\hbar}\frac{\partial f_\lambda}{\partial k_\gamma} = I[f_\lambda] \tag{2.4}$$

To solve this partial differential equation, we will need to convert it to a linear form. We assume the solution to the equation, f_λ^s, which is given by $f_\lambda^s \equiv f_\lambda^0 + \Delta f_\lambda$ where f_λ^0 is the equilibrium distribution and Δf_λ is the deviation. Substituted into Eq. (2.4) we get:

$$\sum_\gamma \frac{qE_\gamma}{\hbar}\frac{\partial f_\lambda^0}{\partial k_\gamma} + \sum_\gamma \frac{qE_\gamma}{\hbar}\frac{\partial \Delta f_\lambda}{\partial k_\gamma} = I[f_\lambda^0 + \Delta f_\lambda] \tag{2.5}$$

note that, taking f_λ^0 to be the Fermi-Dirac distribution:

$$\frac{\partial f_\lambda^0}{\partial k_\gamma} = -\frac{f_\lambda^0}{k_B T}(1 - f_\lambda^0)\frac{\partial \epsilon_\lambda}{\partial k_\gamma} \tag{2.6}$$

where ϵ_λ is the energy of state λ, k_B is the Boltzmann constant, and T is the lattice temperature. Because we are operating where $f_\lambda^0 \ll 1$, we can neglect the second order f_λ^0 terms. Then, we can relate this to the group velocity v_λ yielding:

$$\frac{\partial f_\lambda^0}{\partial k_\gamma} = -\frac{\hbar v_\lambda}{k_B T} f_\lambda^0 \tag{2.7}$$

Two critical components must be linearized: the collision integral and the momentum-space derivative. We will first show the linearization of the BTE and then review these two linear terms in detail. The collision integral has the linear form:

$$I[f_\lambda] = \Theta_{\lambda\lambda'}\Delta f_{\lambda'} \tag{2.8}$$

where $\Theta_{\lambda\lambda'}$ is the scattering matrix and is calculated through Fermi's Golden Rule. We can also treat the momentum-space derivative $\partial\Delta f_\lambda/\partial k_\gamma$ with a finite difference scheme:

$$\partial\Delta f_\lambda/\partial k_\gamma \approx D_{\gamma,\lambda,\lambda'}\Delta f_\lambda \tag{2.9}$$

where $D_{\gamma,\lambda,\lambda'}$ is the finite difference matrix (FDM). With the linearized collision integral and FDM substituted into the BTE, we obtain:

$$\sum_{\lambda'}\Theta_{\lambda,\lambda'}\Delta f_{\lambda'} - \sum_{\gamma}\sum_{\lambda'}\frac{qE_\gamma}{\hbar}D_{\gamma,\lambda,\lambda'}\Delta f_{\lambda'} = \sum_{\gamma}\frac{eE_\gamma}{k_BT}v_\lambda f^0_\lambda \tag{2.10}$$

For simplicity, we define the relaxation operator $\Lambda_{\lambda\lambda'}$ as:

$$\Lambda_{\lambda,\lambda'} \equiv \Theta_{\lambda,\lambda'} - \sum_{\gamma}\frac{q\mathrm{E}_\gamma}{\hbar}D_{\gamma,\lambda,\lambda'} \tag{2.11}$$

Then, since this work deals with holes, $q = e$ and we arrive at the final form of the BTE:

$$\sum_{\lambda'}\Lambda_{\lambda\lambda'}\Delta f_{\lambda'} = \sum_{\gamma}\frac{e\mathrm{E}_\gamma}{k_BT}v_{\lambda,\gamma}f^0_\lambda \tag{2.12}$$

The solution to the linear system, $\Delta f_{\lambda,\alpha}$ (where α is the field direction) can then be expressed as:

$$\Delta f_{\lambda,\alpha} = \frac{eE_\alpha}{k_BT}\sum_{\lambda'}\Lambda^{-1}_{\lambda,\lambda'}\left(v_{\lambda',\alpha}f^0_{\lambda'}\right) \tag{2.13}$$

The scattering matrix

Here we choose to include only electron-phonon scattering with single-phonon interactions. This neglects other forms of scattering such as ionized impurities, quadrupole, multi-phonon scattering, defect scattering, and electron-electron interactions. While work on modeling these other interactions from first principles is underway [35–39, 41], it is nevertheless not well established. Furthermore, these

effects can largely be ignored in the experimental transport data where high purity, lightly doped semiconductors are used. Then, the scattering matrix is given by:

$$\Theta_{\lambda\lambda'} = \frac{2\pi}{N\hbar}\sum_{\mathbf{q}}\left|g_{\lambda,\lambda+\mathbf{q}}\right|^2\left(\delta(\epsilon_\lambda - \hbar\omega_{\mathbf{q}} - \epsilon_{\lambda+q})H_{em}(f_\lambda) + \delta(\epsilon_\lambda + \hbar\omega_{\mathbf{q}} - \epsilon_{\lambda+q})H_{abs}(f_\lambda)\right) \tag{2.14}$$

where N is the total number of $\mathbf{q}$ points, which represent the phonon wavevectors, $g_{\lambda,\lambda+\mathbf{q}}$ is the electron-phonon coupling matrix element which couples the electronic wavevector λ to another state $\lambda+\mathbf{q}$, $\omega_{\mathbf{q}}$ is the frequency of a phonon with wavevector $\mathbf{q}$. The δ functions represent the conservation of energy during scattering events. $H_{em}(f_\lambda)$ and $H_{abs}(f_\lambda)$ are the emission and absorption weights, respectively, which are given by:

$$H_{em}(f_\lambda) = f_\lambda(1 - f_{\lambda+\mathbf{q}})(N_{\mathbf{q}} + 1) - f_{\lambda+\mathbf{q}}(1 - f_\lambda)N_{\mathbf{q}} \tag{2.15}$$

$$H_{abs}(f_\lambda) = f_\lambda(1 - f_{\lambda+\mathbf{q}})N_{\mathbf{q}} - f_{\lambda+\mathbf{q}}(1 - f_\lambda)(N_{\mathbf{q}} + 1) \tag{2.16}$$

where $N_{\mathbf{q}}$ is the phonon distribution function.

Notably, these terms depend on the phonon populations, which may be perturbed by Joule heating, an effect known as the hot phonon effect [119, 120]. Owing to the small free carrier densities in the relevant experiments ($\lesssim 10^{14}\,\mathrm{cm}^{-3}$), this effect may be neglected as the non-equilibrium phonon generation rate is too small to affect hole transport properties [7]. Therefore, we assume $N_{\mathbf{q}}$ is the Bose-Einstein distribution. We can then substitute in $f^s_\lambda \equiv f^0_\lambda + \Delta f_\lambda$ and neglect second order terms on Δf_λ since we assume the deviational occupancy is negligible in size. With these changes we get:

$$H_{em}(\Delta f_\lambda) = \Delta f_\lambda(N_{\mathbf{q}} + 1 - f^0_{\lambda+\mathbf{q}}) - \Delta f_{\lambda+\mathbf{q}}(N_{\mathbf{q}} + f^0_\lambda) \tag{2.17}$$

$$H_{abs}(\Delta f_\lambda) = \Delta f_\lambda(N_{\mathbf{q}} + f^0_\lambda) - \Delta f_{\lambda+\mathbf{q}}(N_{\mathbf{q}} + 1 - f^0_{\lambda+\mathbf{q}}) \tag{2.18}$$

The finite difference matrix

In a finite difference approximation, the derivative is calculated by using a sum of the nearest neighbor values with appropriate weightings. As a simple example, let us consider a finite difference scheme for a 1D chain of 7 points. The FDM for the centered, first derivative to the lowest order of accuracy is shown in Fig. 2.1, neglecting edge points. If the array of points, shown adjacent to the matrix, is multiplied against the FDM the derivative is approximated as shown in the right of the figure. For all points except the edges, an approximation for the derivative is achieved.

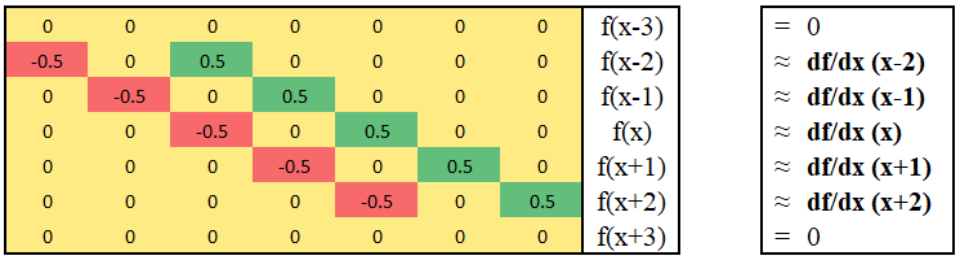

Figure 2.1: A schematic representation of a simple finite difference scheme for a 1D chain of 7 points. The matrix is shown as the colored entries, with the discrete data array adjacent. The results of their product are shown on the right.

In this work we use a similar but slightly more complex scheme. Within the Monkhorst-Pack Brillouin zone (BZ) discretization scheme [121], the reciprocal-space gradient can be approximated by an FDM as defined by Eqns. 8 and B2 of Refs. [122, 123], respectively. In the first sections of this chapter, we consider only nearest-neighbors, which for an FCC silicon lattice consists of the eight neighbors on the corners of the momentum-space BCC lattice.

In this linearized BTE formalism, all column sums of the FDM must also be zero in order to ensure that the total occupation is preserved, but this is not a property that comes automatically for an FDM as seen in Fig. 2.1. Three methods of fixing the FDM matrix column sum issue have been tested, which are shown in Fig. 2.2. First, sacrificing accuracy around the point in momentum-space with the highest energy by setting its corresponding row values to cancel the column sum, shown in Fig. 2.2a. In theory, this fixes the problem numerically and only sacrifices numerical accuracy at the point with the least probable occupation. The second method was to spread out the modified matrix elements to all boundary points, spreading out the inaccuracy across all of the edge states, as shown in Fig. 2.2b. The third method was simply to transpose the matrix and flip the sign of all elements. This fix, as shown in Fig. 2.2c, means that accuracy is explicitly lost for not just the boundary points but also points neighboring the boundaries.

The numerical effect of each column sum fixing scheme is hard to estimate, so we calculated the mobility versus electric field at 40 K with these various FDM fix schemes and show the results in Fig. 2.3. We found that not fixing the column sums resulted in divergence after $\sim$ 0.2 kV cm^{-1}, the maximum energy fix diverged after $\sim$ 0.7 kV cm^{-1}, the boundary point fix diverges after $\sim$ 5 kV cm^{-1}, and the transposition fix does not diverge even at 10 kV cm^{-1}. This result was not expected since the last scheme also reduces accuracy at the boundary point nearest-neighbors,

0.5	0.5	0	0	0	-0.5	-0.5	f(x-3)
-0.5	0	0.5	0	0	0	0	f(x-2)
0	-0.5	0	0.5	0	0	0	f(x-1)
0	0	-0.5	0	0.5	0	0	f(x)
0	0	0	-0.5	0	0.5	0	f(x+1)
0	0	0	0	-0.5	0	0.5	f(x+2)
0	0	0	0	0	0	0	f(x+3)

= [f(x-3)+f(x-2)-f(x+2)-f(x+3)]/2
≈ **df/dx (x-2)**
≈ **df/dx (x-1)**
≈ **df/dx (x)**
≈ **df/dx (x+1)**
≈ **df/dx (x+2)**
= 0

0.5	0.5	0	0	0	0	0	f(x-3)
-0.5	0	0.5	0	0	0	0	f(x-2)
0	-0.5	0	0.5	0	0	0	f(x-1)
0	0	-0.5	0	0.5	0	0	f(x)
0	0	0	-0.5	0	0.5	0	f(x+1)
0	0	0	0	-0.5	0	0.5	f(x+2)
0	0	0	0	0	-0.5	-0.5	f(x+3)

= [f(x-3)+f(x-2)]/2
≈ **df/dx (x-2)**
≈ **df/dx (x-1)**
≈ **df/dx (x)**
≈ **df/dx (x+1)**
≈ **df/dx (x+2)**
= [-f(x+3)-f(x+2)]/2

0	0.5	0	0	0	0	0	f(x-3)
0	0	0.5	0	0	0	0	f(x-2)
0	-0.5	0	0.5	0	0	0	f(x-1)
0	0	-0.5	0	0.5	0	0	f(x)
0	0	0	-0.5	0	0.5	0	f(x+1)
0	0	0	0	-0.5	0	0	f(x+2)
0	0	0	0	0	-0.5	0	f(x+3)

= f(x-2)/2
= f(x-1)/2
≈ **df/dx (x-1)**
≈ **df/dx (x)**
≈ **df/dx (x+1)**
= -f(x+1)/2
= -f(x+2)/2

Figure 2.2: Possible fixes to set the FDM column sum to zero. Top: the maximum energy fix, in which the column sums are fixed via the row corresponding to the single highest-energy state. Middle: the boundary fix, in which the column sums are fixed in the rows corresponding to boundary points. Bottom: The transpose fix, in which the matrix is transposed and signs reversed.

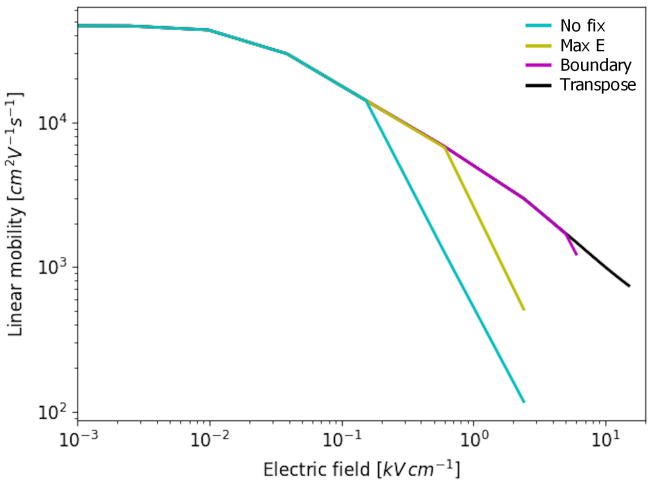

Figure 2.3: The DC mobility versus electric field at 40 K calculated using different column sum fixes for the FDM. No fix (cyan) diverges first, then the maximum energy fix (gold), then the boundary fix (magenta), and the transposition fix (black) shows no divergence at the highest field.

but nevertheless, it results in the most numerically stable result. Therefore, it was this last solution that was employed in this and other works [84–87].

Calculating transport quantities

This solution to the BTE can be used to calculate various observables. For instance, the mobility is given by the average velocity (the drift velocity) divided by the electric field:

$$\mu_{\alpha\beta}(\mathbf{E}) = \frac{2}{E_\beta \mathcal{V}} \sum_\lambda v_{\lambda,\alpha} \Delta f_{\lambda,\beta} \tag{2.19}$$

where $\mathcal{V}$ is the supercell volume, α is the direction along which the current is measured, and β is the direction along which the electric field is applied. The factor of two accounts for spin degeneracy. Expressed using the solution for Δf_λ is [24]:

$$\mu_{\alpha\beta}(\mathbf{E}) = \frac{2e}{k_B T \mathcal{V}} \sum_\lambda v_{\lambda,\alpha} \sum_{\lambda'} \Lambda^{-1}_{\lambda\lambda'} \left(v_{\lambda',\beta} f^0_{\lambda'} \right) \tag{2.20}$$

The AC mobility is also of importance as it describes the response of the system to a perturbing electric field $\delta E_\alpha e^{i\omega t}$ (where ω is the angular frequency of the perturbing field) under a steady state condition induced by a DC electric field E_β. The behavior of this quantity reveals information about relaxation times within the system. The AC mobility can also be calculated using the BTE. Given that the time-dependent part of the occupation function takes the form of $\delta f_\lambda(t) = \delta f_\lambda(\omega) e^{i\omega t}$, with $f = f^s + \delta f(t)$ and $\mathbf{E} = \mathbf{E}_{DC} + \delta\mathbf{E}(t)$, we obtain:

$$i\omega \delta f_\lambda + \frac{e}{\hbar} \mathbf{E} \cdot \nabla_{\mathbf{k}} f_\lambda = \left(\frac{\partial f}{\partial t} \right)_{coll} \tag{2.21}$$

Running through the same derivation given prior, noting that unlike f^0_λ the derivative of f^s_λ cannot be analytically taken, we obtain the solution:

$$\delta f_{\lambda,\alpha} = -\frac{e \delta E_\alpha}{\hbar} \sum_{\lambda'} (i\omega \mathbb{I} + \Lambda)^{-1}_{\lambda,\lambda'} \left(D_{\alpha,\lambda,\lambda'} f^s_{\lambda'} \right) \tag{2.22}$$

where $\mathbb{I}$ is the identity matrix. This solution can then be used to calculate the AC mobility:

$$\mu_{\alpha\beta}(\mathbf{E}) = -\frac{2e}{\hbar \mathcal{V}} \sum_\lambda v_{\lambda,\alpha} \sum_{\lambda'} (i\omega \mathbb{I} + \Lambda)^{-1}_{\lambda,\lambda'} \left(D_{\alpha,\lambda,\lambda'} f^s_{\lambda'} \right) \tag{2.23}$$

Calculating noise quantities

In addition to mobility, which represents a mean characteristic of the steady-state distribution, the current PSD, which quantifies the random fluctuations of carriers about the non-equilibrium steady-state distribution, is obtainable through the BTE. The PSD can be computed as the Fourier transform of the autocorrelation function through the Wiener-Khintchine theorem [12]:

$$S_{j_\alpha j_\beta}(\mathbf{E},\omega) \equiv (\delta j_\alpha j_\beta)_\omega = 2\int_{-\infty}^{\infty} \overline{\delta j_\alpha(t)\delta j_\beta} e^{-i\omega t} dt \tag{2.24}$$

where j represents the current density, and δj represents a fluctuation in the current density ($\delta j(t) = j(t) - j^s$). The overline indicates the ensemble average. Since current density can be expressed in terms of the occupancy (in the same manner that the mobility is in Eq. (2.20)), it follows that this can be done for $\overline{\delta j_\alpha(t)\delta j_\beta}$ [56]:

$$\overline{\delta j_\alpha(t)\delta j_\beta} = \left(\frac{2e}{\mathcal{V}}\right)^2 \sum_{\lambda_1}\sum_{\lambda_2} v_{\lambda_1,\alpha} v_{\lambda_2,\beta} \overline{\delta f_{\lambda_1}(t)\delta f_{\lambda_2}} \tag{2.25}$$

where $\overline{\delta f_{\lambda_1}(t)\delta f_{\lambda_2}}$ is known as the time-displaced two-particle correlation function. Taking the Fourier transform of both sides of Eq. (2.25) we get the relationship:

$$(\delta j_\alpha j_\beta)_\omega = \left(\frac{2e}{\mathcal{V}}\right)^2 \sum_{\lambda_1}\sum_{\lambda_2} v_{\lambda_1,\alpha} v_{\lambda_2,\beta} \left(\delta f_{\lambda_1}\delta f_{\lambda_2}\right)_\omega \tag{2.26}$$

Thus, to solve for $(\delta j_\alpha j_\beta)_\omega$ we must find $\left(\delta f_{\lambda_1}\delta f_{\lambda_2}\right)_\omega$.

Let us consider Onsager's regression hypothesis [124] which proposes that the behavior of fluctuations in a system obey the same physical laws of the system itself. In terms of the system described here, this means $\overline{\delta f_{\lambda_1}(t)\delta f_{\lambda_2}}$ obeys the BTE. A rigorous derivation is possible but beyond the scope of this work [56]. Therefore:

$$\left[\frac{\partial}{\partial t} + \sum_{\lambda} \Lambda_{\lambda,\lambda'}\right] \overline{\delta f_{\lambda_1}(t)\delta f_{\lambda_2}} = 0 \tag{2.27}$$

Now, this equation dictates the necessary form of $\overline{\delta f_{\lambda_1}(t)\delta f_{\lambda_2}}$:

$$\overline{\delta f_{\lambda_1}(t)\delta f_{\lambda_2}} = \overline{\delta f_{\lambda_1}\delta f_{\lambda_2}} e^{-\Lambda t} \tag{2.28}$$

where $\overline{\delta f_{\lambda_1}\delta f_{\lambda_2}}$ represents the initial condition of the system ($\overline{\delta f_{\lambda_1}(t)\delta f_{\lambda_2}}|_{t=0}$) and is known as the one-time two-particle correlation function. From here we can take the Fourier transform:

$$\left(\delta f_{\lambda_1}\delta f_{\lambda_2}\right)_\omega = \int_{-\infty}^{\infty} \overline{\delta f_{\lambda_1}\delta f_{\lambda_2}} e^{-\Lambda t} e^{-i\omega t} dt \tag{2.29}$$

Owing to the real valued and stationary properties of the autocorrelation function (namely even symmetry owing to $\overline{\delta f_{\lambda_1}(t)\delta f_{\lambda_2}} = \overline{\delta f_{\lambda_1}(-t)\delta f_{\lambda_2}}$):

$$\int_{-\infty}^{\infty} \overline{\delta f_{\lambda_1}\delta f_{\lambda_2}} e^{-\Lambda t} e^{-i\omega t} dt = 2\Re\left[\int_0^{\infty} e^{-t(i\omega+\Lambda)}\overline{\delta f_{\lambda_1}\delta f_{\lambda_2}} dt\right] \tag{2.30}$$

therefore:

$$\left(\delta f_{\lambda_1}\delta f_{\lambda_2}\right)_\omega = 2\Re\left[\sum_{\lambda_1'} (i\omega\mathbb{I} + \Lambda)^{-1}_{\lambda_1,\lambda_1'}\overline{\delta f_{\lambda_1'}\delta f_{\lambda_2}}\right] \tag{2.31}$$

Now all that remains is to find an expression for $\overline{\delta f_{\lambda_1}\delta f_{\lambda_2}}$. Fortunately, this has been previously solved by Refs. [9, 125] and is also explained in detail in [56]. This problem, for a non-degenerate system consisting of N indistinguishable particles, is equivalent to the problem of distributing balls among a set of bins, with any given bin having the probability f_λ/N. This leads to the standard multinomial distribution, and the quantity we are after is equivalent to the variance, therefore:

$$\overline{\delta f_{\lambda_1}\delta f_{\lambda_2}} = f_{\lambda_1}\delta_{\lambda_1,\lambda_2} - \frac{f_{\lambda_1}f_{\lambda_2}}{N} \tag{2.32}$$

where $N = \sum_\lambda f_\lambda$ is the number of holes in the Brillouin zone. Combining Eq. (2.26), Eq. (2.31), and Eq. (2.32), we obtain:

$$(\delta j_\alpha j_\beta)_\omega = 2\left(\frac{2e}{\mathcal{V}}\right)^2 \Re\left[\sum_{\lambda_1} v_{\lambda_1,\alpha}\sum_{\lambda_1'}(i\omega\mathbb{I} + \Lambda)^{-1}_{\lambda_1,\lambda_1'}\sum_{\lambda_2} v_{\lambda_2,\beta}\left(f^s_{\lambda_1'}\delta_{\lambda_1',\lambda_2} - \frac{f_{\lambda_1'}f_{\lambda_2}}{N}\right)\right] \tag{2.33}$$

the last sum over λ_2 can be taken analytically:

$$\sum_{\lambda_2} v_{\lambda_2,\beta}\left(f^s_{\lambda_1'}\delta_{\lambda_1',\lambda_2} - \frac{f_{\lambda_1'}f_{\lambda_2}}{N}\right) = f^s_{\lambda_1'}\left(v_{\lambda_1',\beta} - V_\beta\right) \tag{2.34}$$

where V_β is the drift velocity along axis β defined by:

$$V_\beta = \frac{1}{N}\sum_\lambda v_{\lambda,\beta} f^s_\lambda \tag{2.35}$$

Substituting Eq. (2.34) into Eq. (2.33), the PSD of current fluctuations can finally be expressed as:

$$S_{j_\alpha j_\beta}(\mathbf{E},\omega) = 2\left(\frac{2e}{\mathcal{V}}\right)^2 \Re\left[\sum_\lambda v_{\lambda,\alpha}\sum_{\lambda'}(i\omega\mathbb{I} + \Lambda)^{-1}_{\lambda\lambda'}\left(f^s_{\lambda'}\left(v_{\lambda',\beta} - V_\beta\right)\right)\right] \tag{2.36}$$

Lastly, it is worth noting that this derivation can also be performed using Langevin dynamics and Green's functions. However, the derivation given here is the mathematically simpler of the two and is also easier to physically intuit. The other derivations are discussed in Refs. [9, 56].

Why p-type silicon?

In this work, we apply this high-field charge transport formalism to holes in silicon. Recent findings using this technique have revealed that two-phonon scattering is important in both GaAs [85] and Si [86, 87], which are material systems with multiple conduction band minima (for GaAs these are separated by a small energy gap, and in Si they occur as identical "pockets" in momentum-space). The *ab-initio* treatment of high-field transport has not yet been applied to *p*-type semiconductors in general, and the accuracy of the simulations has not been tested for systems with a single band extrema (for *p*-type semiconductors, the valence band maximum (VBM)), multiple bands at the same wave vector, or in systems with warped, highly non-parabolic bands.

The valence band structure of silicon allows a test of the theory against all three of these features, as shown in Fig. 2.4. Fig. 2.4a shows a large picture of the electronic bands in Si. In electron transport, the minimum near X is most relevant, and itself is rich with transport phenomena owing to the six pockets which occur due to symmetry. In hole transport, however, a single maximum occurs at Γ. This maximum is shown in detail in Fig. 2.4b. Three bands are (nearly) degenerate at this point: the heavy, light, and split-off bands. Due to the effect of spin-orbit coupling (SOC), the split-off band is separated from the other two bands by a small energy gap ($\approx$ 44 meV). The bands are non-parabolic, meaning that the hole energy is not simply related to the square of the wavevector magnitude. Lastly, heavy and light hole bands are heavily warped, meaning the energy-wavevector relationship is dependent on the wavevector direction, not just its magnitude. This latter feature is captured in Fig. 2.4c, which shows the isoenergy contours for the heavy and light holes. The heavy hole band forms a ten-lobed shape while the light hole band is nearly cubical in momentum-space. Therefore, anisotropy in *p*-Si is largely driven by this feature, as opposed to *n*-Si where the pockets exhibit different behavior in field orientations which break their symmetry. Finally, *p*-Si makes for a good testbed for these high-field calculations as it has been one of the most historically investigated semiconductors, so there is a large amount of experimental data to compare against.

Charge transport in *p*-Si at cryogenic temperatures and microwave frequencies is of particular interest due to two anomalous transport characteristics which appear in the experimental data. First, at large electric fields of tens of kV cm^{-1}, semiconductors generally exhibit drift velocity saturation in which the drift velocity no longer

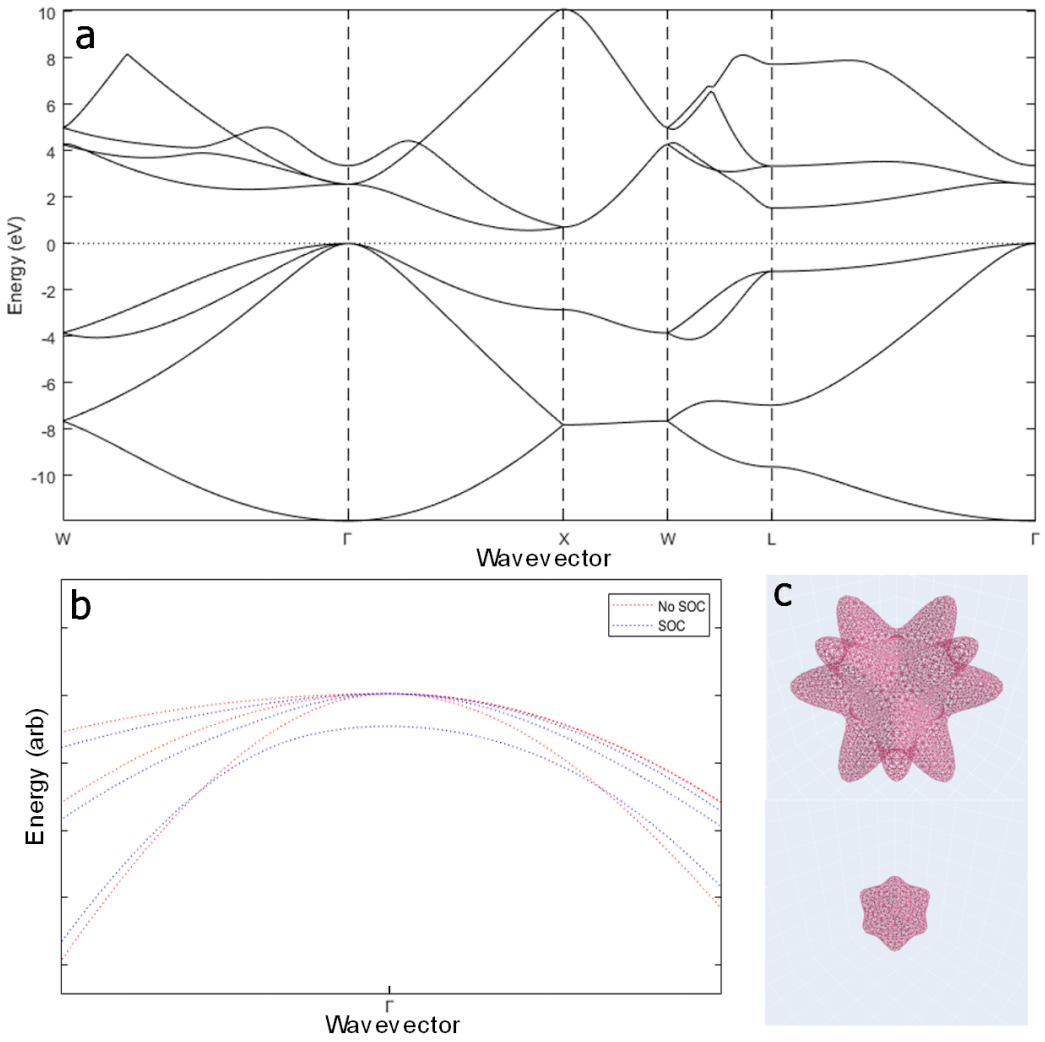

Figure 2.4: (a) *Ab-initio* Si bandstructure with the fermi level set to the VBM for reference. Three bands are relevant at the VBM, at Γ: the heavy, light, and split-off bands. (b) Close-up of the VBM. Calculations using SOC in blue and without SOC in red. Without SOC, all three valence bands are degenerate at Γ, however including SOC separates the aptly named split-off band. (c) Rendering of the iso-energy contours of the heavy (upper) and light (lower) bands in momentum-space. The heavy band forms a 10-lobed shape, while the light band is nearly cubical.

increases with field [14]. In *p*-Si below 40 K, an additional regime of drift velocity saturation occurs at considerably smaller fields, approximately 0.1 kV cm^{-1} [7]. This feature has been studied numerically by semi-analytical [126, 127] and full-band Monte-Carlo methods [79]. While an initial investigation attributed the feature to the non-parabolic hole dispersion and Bose-Einstein distribution occupation of phonons [126], a later study instead attributed the behavior solely to population of the spin-orbit band at high fields [127]. The “shoulder" feature has more recently been computationally reproduced using full-band Monte Carlo [79], but without analysis. Therefore, the explanation of the anomalous saturation regime remains unresolved.

The second anomalous feature appears in the PSD. It has been observed experimentally that in *p*-Si at 10 GHz and 77 K, a non-monotonic (peak) trend with increasing DC electric field is observed for current noise both longitudinal and transverse to the field. This feature has also been observed in *n*-Si and Ge [54, 128]. The trend was originally ascribed to an initial increase due to carrier heating followed by a decrease due to a decreasing momentum relaxation time at high fields [128]. In Sec. 9.3 of Ref. [12], the trend was attributed to a field-dependent energy relaxation time which influences the convective noise mechanism (described in section 7.2 of the same reference). The convective mechanism arises from the coupling of velocity and energy fluctuations of the charge carriers, leading to a decrease in the PSD with increasing electric field for materials with a sublinear current-voltage characteristic. Given these differing explanations, the origin of the peak remains unclear.

2.2 Computational details

The numerical details used here are identical to those in Refs. [84, 85]. The calculation of electronic structure and electron-phonon matrix elements are performed with Quantum Espresso [129, 130] using a coarse 8×8×8 grid, wave function energy cutoff of 60 Ryd, and a lattice constant of 5.430 Å. The spin-orbit interaction is included. The interpolation to fine grids is performed using PERTURBO [22].

The linearized BTE is solved using the GMRES algorithm [131]. Other algorithms including MinRes, LGMRes, QMR, and GCROTMK were also investigated, but the difference in both the computational cost and end results were negligible. Observables are calculated using a Brillouin zone sum. Transport and noise properties are calculated for lattice temperatures of 300 K and 77 K, with carrier densities of 10^{16} cm^{-3} and 10^{14} cm^{-3}, maximum energy of 192 meV and 92 meV, Gaussian smearing

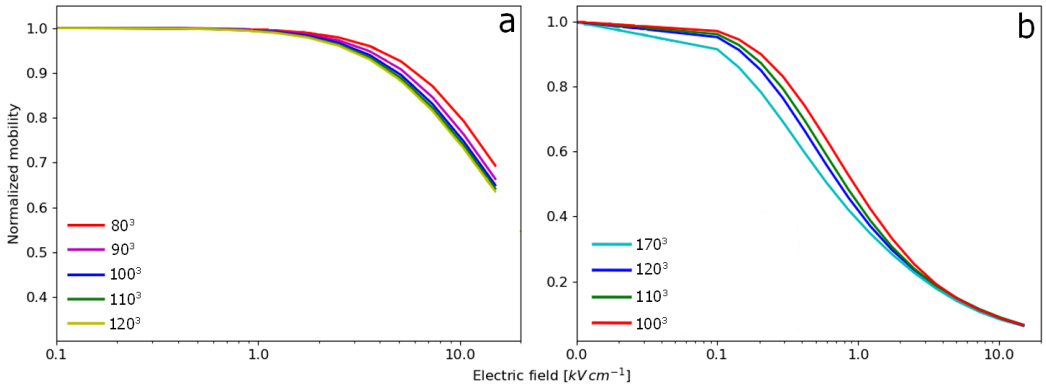

Figure 2.5: (a) Normalized DC mobility vs electric field at 300 K, using various grid densities. Convergence is achieved at 120^3. (b) Normalized DC mobility vs electric field at 77 K, using various grid densities. At this lower temperature, convergence is achieved at around 170^3. No points were calculated between 0 and 0.1 kV/cm, so lines are a guide within this region.

parameters of 5 meV and 2.5 meV, and grid densities of 120^3 and 180^3, respectively. Increasing the grid densities to 130^3 and 190^3, respectively, resulted in less than a 1% change in mobility and PSD with the exception of the 77 K PSD, which exhibited a 3% change at the highest fields. We show representative convergence results for the mobility at 300 and 77 K in Fig. 2.5.

These convergence results are in agreement with a recent low-field study [82]. Only the heavy and light valence bands were included in the calculations presented as the split-off band was found to contribute negligibly to all quantities while considerably increasing computational costs. Where normalization of transport quantities is performed, quantities are shown relative to their value at 1 V cm^{-1}. Furthermore, we define error between calculations and experiments for arbitrary property y as a function of some parameter as $||y_{exp} - y_{calc}||_2 \,/\, ||y_{exp}||_2$. The anisotropy for a property along different crystallographic directions is defined at a parameter value x for direction α as $|y(x)_{[100]} - y(x)_{\alpha}| \,/\, |y(x)_{[100]}|$.

2.3 Results: standard properties

Transport

We begin by examining the electric field dependence of the DC mobility at 300 K. The calculated low-field mobility is 525 cm^2 V^{-1} s^{-1}, overestimated compared to the experimental value of $\sim$ 450 cm^2 V^{-1} s^{-1} [50, 58]. We find that calculations yield the same overestimate at all fields, so the mobilities have been normalized to facilitate the comparison of trends; computed data are normalized to the calculated

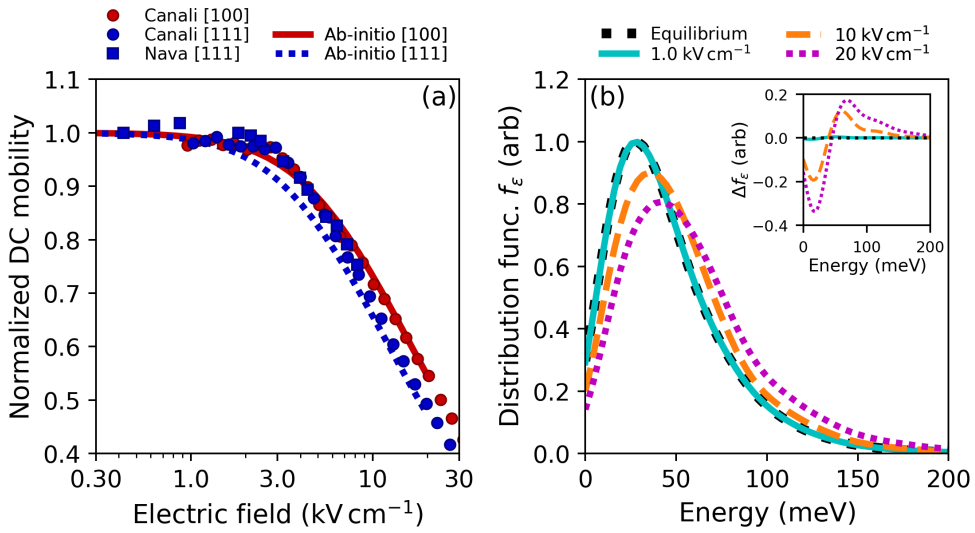

Figure 2.6: (a) Normalized DC mobility versus electric field at 300 K. Calculated data normalized to their values at 1 V cm^{-1}, experimental data normalized to the low field value of Ref. [50] (450 cm^2 V^{-1} s^{-1}). Calculated data shown for electric fields in various crystallographic axes including [100] (solid red line) and [111] (dotted blue line). Experimental data shown from Canali et al. [58] ([100] as red circles, [111] as blue circles), and Nava et al. [50] ([111] as blue squares). (b) Hole distribution function versus energy (f_ϵ), from the valence band maximum at 300 K for electric fields of 1 kV cm^{-1}(solid light blue line), 10 kV cm^{-1} (dashed orange line), and 20 kV cm^{-1} (dotted magenta line) applied along the [100] crystallographic axis. The equilibrium distribution is shown as a dashed black line. The distribution function was calculated using kernel density estimation. Inset: deviation from the equilibrium distribution function $\Delta f_\epsilon = f_\epsilon - f_\epsilon^0$. The redistribution of holes to higher energies with increased field strength is evident, leading to the decrease in mobility in (a).

low-field mobility, while experimental data are normalized to the low-field mobility measured by Ref. [50] (450 cm^2 V^{-1} s^{-1}).

The calculated DC mobility versus electric field in various crystallographic axes is shown in Fig. 2.6a along with experimental data from Refs. [50, 58]. At low fields $\lesssim$ 1 kV cm^{-1}, the mobility is nearly constant as expected in the Ohmic regime. At fields $\gtrsim$ 1 kV cm^{-1}, the mobility decreases with increasing field. We find the normalized mobilities are in quantitative agreement with experiment, with errors of only 2.5% and 5.4% for the [100] and [111] directions, respectively (compared to Ref. [58]). Additional data can be found in Ref. [7], which is not shown but is also in similar agreement. There is a minor discrepancy in the onset of anisotropy, which occurs at fields $\sim$ 80% lower than predicted by experiment for the

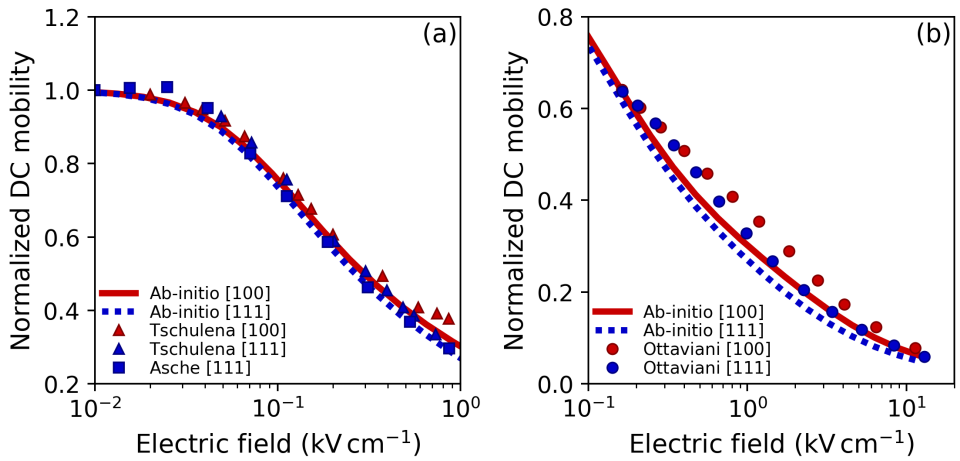

Figure 2.7: (a) Normalized DC mobility versus electric field at 77 K. Calculated data shown for electric fields along the crystallographic axes [100] (solid red line) and [111] (dotted blue line). Calculated data normalized to their values at 1 V cm^{-1}. Experimental data shown from Tschulena [59] ([100] red triangles, [111] blue triangles) and Asche et al. [57] ([111] blue squares). (b) Same as (a) but for data from Ref. [7] ([100] red circles, [111] blue circles), normalized to 9800 cm^2 V^{-1} s^{-1}.

[111] direction. However, the anisotropy at high fields is in good agreement with experiment; at 20 kV cm^{-1} the [111] anisotropy is 13% and 11% for the calculations and measurements, respectively. It was also found that the properties along the [110] and [111] directions are degenerate at all fields, in agreement with data from Ref. [7].

The decrease in mobility with increasing field is attributable to the heating of the holes owing to their finite energy relaxation time and because hole scattering rates increase with energy (see Fig. 6b of Ref. [82]). Thus, the mobility decreases as holes are heated by the applied electric field. To illustrate this point, we computed the hole distribution versus energy (f_ϵ) at various electric fields in Fig. 2.6b. At low fields ($\lesssim$ 3 kV cm^{-1}), the steady-state distribution of holes coincides with the thermal distribution, and $\Delta f_\epsilon \approx 0$. At higher fields, Δf_ϵ becomes non-negligible and the steady-state distribution f_ϵ is shifted to higher energies, ultimately leading to a nonlinear response between drift velocity and electric field.

Next, we show the mobility versus electric field at 77 K in Fig. 2.7. Data from Refs. [57, 59] were originally reported in normalized form, and are thus presented separately from Ref. [7] for which the absolute high-field mobility was reported but not the low-field mobility, complicating the normalization. At this temperature the

low-field mobility is again overestimated, with a value of 12300 cm^2 V^{-1} s^{-1} compared to the experimental value of $\sim$ 9800 cm^2 V^{-1} s^{-1} [7, 132]. Mobility versus field at 77 K for Refs. [57, 59] are presented in Fig. 2.7a, along with calculations. Quantitative agreement with experiment is observed from 0 – 0.6 kV cm^{-1}. Above this field there is a minor discrepancy in the [100] direction from Ref. [59], but other data remain in agreement with calculations. The overall error between calculations in the [100] direction with data from Ref. [59] is 3.6%.

Experimental data from Ref. [7], which do not reach the Ohmic regime, have been normalized to 9800 cm^2 V^{-1} s^{-1} and are presented in Fig. 2.7b along with calculated data. While the computed [111] anisotropy is once again in good quantitative agreement, being 20% (15%) for calculations (measurements) at 12 kV cm^{-1}, the mobility-field values only agree qualitatively, with an error of $\sim$12.5% in all crystallographic directions. At 77 K, the [110] mobility is not degenerate with the [111] mobility, with 23 % (29%) calculated (measured) anisotropy, but data for this field direction is omitted for clarity. It should be noted, however, that comparing experimental data from both figures in the region of 0.1–0.7 kV cm^{-1}, the data from Refs. [57, 59] agree quantitatively with the calculations while the data from Ref. [7] do not. Some inconsistency therefore exists between measurements in these references, and the appropriate reference for comparison is not presently clear.

Noise

We next examine the PSD in the low-frequency limit, defined as frequencies for which $\omega\tau \ll 1$. Here, τ is a characteristic relaxation time of energy, momentum, or similar parameter. In this limit, the current PSD is proportional to the diffusion coefficient through the fluctuation-diffusion relation (see Eqn. 2.49 of Ref. [56]). Experimentally, the diffusion coefficient has been obtained by the TOF method [89] and from low-frequency noise measurements [50, 55]. We calculate the diffusion coefficient through the current PSD, which was computed at 1 GHz to obtain the low-frequency value; negligible differences were observed between 1 GHz and 100 MHz.

The hole diffusion coefficient versus electric field at 300 K is shown in Fig. 2.8a. Experimental measurements from TOF and noise data from Ref. [50] are also shown normalized to the equilibrium value reported by the same study (11.6 cm^2 s^{-1}). The calculations are in reasonable quantitative agreement with experiment, with an error of 5.5%, although the data from noise measurements are much closer to calculations,

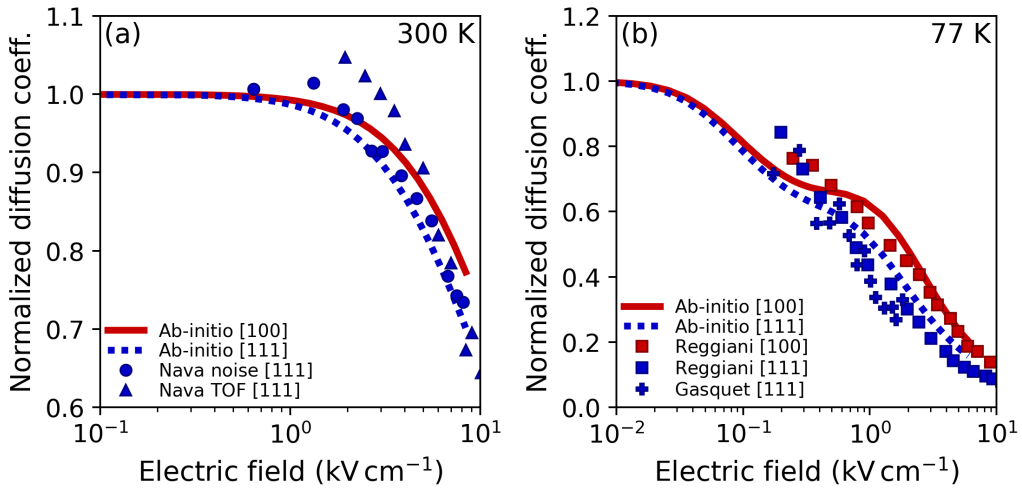

Figure 2.8: (a) Normalized hole diffusion coefficient versus electric field at 300 K. Calculated data normalized to their values at 1 V cm^{-1}. Calculated data shown for electric fields applied in the crystallographic axes [100] (solid red line) and [111] (dotted blue line). Experimental data shown from Nava et al. [50] ([111], noise measurements as blue circles, TOF measurements as blue triangles) and normalized to 11.6 cm^2 s^{-1}. (b) Same as (a) at 77 K. Experimental data shown from Reggiani et al. [133] ([100] as red squares, [111] as blue squares) and Gasquet et al. [55] ([111] as blue crosses).

with an error of only 2.5%. At 300 K, comparing Figs. 2.6a and 2.8a, we observe that the decrease in diffusion coefficient with increasing electric field follows the same trend as that of the mobility. This result is expected as the system remains in the warm carrier regime for all fields considered. At the highest field presented here, the mean energy of the steady-state distribution is greater than that of the equilibrium distribution by only $\sim$ 10%, indicating that the steady-state distribution remains close to the equilibrium distribution. In this case, the fluctuation-dissipation relation remains approximately valid [84], so the diffusion coefficient is related to the mobility through Eq. (1.2).

At 77 K and high fields ($\gtrsim$ 0.1 kV cm^{-1}), holes enter the hot carrier regime, with mean energies exceeding the equilibrium value by up to 200% at 6 kV cm^{-1}. Thus, in contrast to the 300 K case, it is expected that the mobility and diffusion coefficient exhibit distinct dependencies on electric field. We present the diffusion coefficient versus field at 77 K in Fig. 2.8b. Experimental data have been normalized to the approximate low-field diffusion coefficient obtained from the Einstein relationship assuming 9800 cm^2 V^{-1} s^{-1} as the low-field mobility (yielding 65 cm^2 s^{-1}). The calculations predict an initial decrease, followed by a plateau around $\sim$ 0.5 kV

cm^{-1}, and a subsequent decrease. This trend has been previously attributed to the rapid increase in energy relaxation rate once optical phonon emission becomes possible (see Ref. [134] and p.70 of Ref. [12]). The differing trends of mobility and diffusion coefficient highlight the failure of equilibrium relationships for hot carriers, and hence the utility of calculating both steady-state and fluctuation properties at high fields.

The 77 K diffusion coefficient calculations exhibit qualitative agreement with experiment, but discrepancies are clearly present. At 3 kV cm^{-1}, the calculated (experimental) [111] anisotropy is 26% (39%), indicating the anisotropy has been reasonably captured. However, the plateau feature in the calculation is not evident in the data. We note that experimental details are not available for data from Ref. [133], and data from both Refs. [55, 133], obtained from TOF measurements, have uncertainties on the order of 25% [135]. Comparison of the trends is therefore challenging considering the uncertainties in experiment.

Energy relaxation time

At low temperatures the mechanisms by which carriers lose energy depend on the electric field strength. At low fields and at the temperatures in this study, scattering is dominated by acoustic phonons because holes lack sufficient energy to emit optical phonons, and the energy relaxation time (ERT) achieves its maximum value with little dependence on field strength. At high fields, the carriers are heated to energies sufficient to emit optical phonons, and the ERT decreases by orders of magnitude [136] since, with respect to energy, optical phonon emission is a far more efficient relaxation process than acoustic phonon emission. Experimentally, the field-dependent ERT has been estimated by measuring the transverse noise temperature and using a phenomenological energy balance equation as:

$$\tau_\epsilon(\mathrm{E}) = \frac{3k_B}{2e}\frac{\left(T_\perp^n - T_0\right)}{\mu \mathrm{E}^2} \tag{2.37}$$

where μ is the DC mobility at electric field E, $T_\perp^n$ is the transverse noise temperature, and T_0 is the lattice temperature (see Sec. 9.2 of [12] or Sec. 4.5 of Ref. [10]). However, computationally the energy relaxation time is obtained more straightforwardly though the energy PSD; this property follows the form of the current PSD in Eq. (2.36) but with the quantity of interest being energy instead of velocity, as follows:

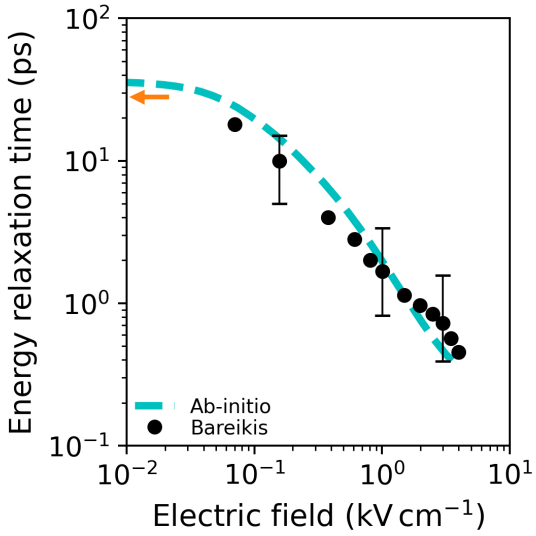

Figure 2.9: Hole energy relaxation time versus electric field applied in the [110] direction at 77 K from calculation (dashed light blue line) and experiment (black circles, Ref. [54]). Also shown is the equilibrium (zero field) value of τ_ϵ measured by Ref. [137] (orange arrow).

$$S_{\epsilon\epsilon}(\mathbf{E},\omega) = 2\left(\frac{2}{\mathcal{V}}\right)^2 \Re\left[\sum_\lambda \epsilon_\lambda \sum_{\lambda'}\left((i\omega\mathbb{I}+\Lambda)^{-1}_{\lambda,\lambda'}(f^s_{\lambda'}(\epsilon_{\lambda'}-\mathcal{E}))\right)\right] \tag{2.38}$$

where ϵ_λ is the energy of a hole relative to the energy at the valence band maximum, and $\mathcal{E}$ is the mean energy given by:

$$\mathcal{E} = \frac{1}{N}\sum_\lambda \epsilon_\lambda f^s_\lambda \tag{2.39}$$

A representative calculated energy PSD is shown in Fig. 3b of Ref. [84]. The ERT is then obtained from a Lorentzian fit of the computed energy PSD [12]:

$$S_{\epsilon\epsilon}(\mathbf{E},\omega) = \frac{S_{\epsilon\epsilon}(\mathbf{E},0)}{1+(\omega\tau_\epsilon)^2} \tag{2.40}$$

We compare our ERT calculations to the experimental data reported in Ref. [54]. The experimental and calculated ERT are shown in Fig. 2.9. We find the equilibrium energy relaxation time at zero electric field to be within $\sim 30\%$ of the value obtained from [137]. High-field calculations are also in quantitative agreement with experiment considering the experimental uncertainty. As expected, the ERT shows a rapid

decrease with field once optical phonon emission becomes possible around $\sim$ 0.1 kV cm^{-1}, consistent with the start of the diffusion coefficient plateau in Fig. 2.8b.

2.4 Adaptation of computations for cryogenic temperatures

Previously in this work, and in other prior high-field works [84–87], the inclusion of only first-nearest-neighbors in the finite difference scheme provided adequate accuracy at $T \geq 77$ K. At temperatures below 77 K, we found the quality of this numerical finite difference approximation to be poor. This manifested either as an inability to converge the GMRES solution or unphysical transport and noise trends. This latter issue stemmed from a nonphysical hole occupation function. In Fig. 2.10 we show the raw occupation function data at 20 K with various field strengths and FDM accuracy levels; moving down a column is an increase in field strength, and right across a row is an increase in FDM accuracy, which will be explained below. We observe that for 1 shell of nearest neighbors, the distribution function quickly becomes nonphysical: even at 0.15 kV cm^{-1}, negative occupation is observed. Because we are dealing with holes, this indicates an occupation greater than unity for the corresponding electron occupation function, which violates the Pauli exclusion principle. Furthermore, at higher electric fields such as 2.4 kV cm^{-1}, a significant number of outliers are observed. The distribution function must be be a smooth function given there are no discontinuous features of the electronic band structure. Although f_ϵ is shown instead of the single-valued function $f_{\mathbf{k}}$, resulting in a dispersion at any given energy, outliers should still not occur.

Both the negative occupation and discontinuous occupation function manifest in the transport properties as nonphysical results: for instance, a negative PSD. However, nonphysical trends are not always obvious so calculations near the limits of the numerical technique would be considered suspect. This issue could, in principle, be addressed by increasing the grid density. In the past this was the method used at higher temperatures and the convergence of transport properties was used as the measure to address the underlying numerical problem. However, for $T < 77$ K the grid density cannot be made sufficiently large to achieve the accuracy needed due to three problems:

1. The multi-band structure of p-Si increases the number of k-points over similar calculations for n-GaAs and n-Si by a large factor. Due to SOC, the bands are doubled, and the inclusion of both light and heavy holes again doubles the number of bands. This results in a 16x increase in the size of the matrices

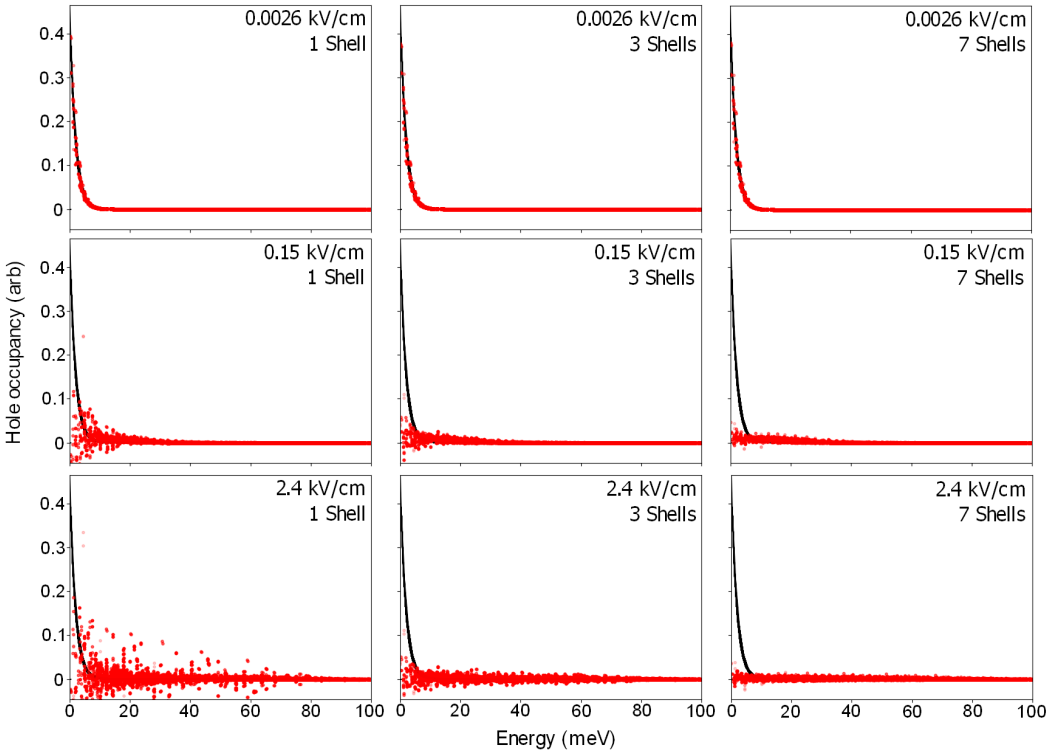

Figure 2.10: Raw hole occupation function versus energy at various electric fields using varying FDM shells at 20 K. With 1 and 3 shells, negative occupation is observed at 0.15 and 2.4 kV/cm. The equilibrium distribution is shown as a black line, for reference. The use of 1 shell also results in a significant number of outlying points. However, both of these issues are almost completely mitigated by using 7 shells.

involved. This square scaling is also the reason why the split-off band was omitted.

2. The energy window cannot be made much smaller than the optical phonon energy, approximately 60 meV. This is because acoustic phonons cannot sufficiently relax carrier energy at high fields. Therefore, if the energy window is too small such that carriers don't emit optical phonons, calculations quickly diverge as carriers collect at the edge of the energy window.

3. The equilibrium distribution function becomes increasingly exponential as temperatures are decreased, meaning that at low fields the f_λ^0 becomes increasingly concentrated at low energies, and the derivative becomes steeper. Therefore, to maintain accuracy the compensation in grid density would have to be similarly exponential, quickly outscaling the available computational resources.

0	0	0	0	0	0	0	f(x-3)
-0.5	0	0.5	0	0	0	0	f(x-2)
0.08333	-0.6667	0	0.66667	-0.0833	0	0	f(x-1)
-0.0167	0.15	-0.75	0	0.5	-0.15	0.01667	f(x)
0	0	0.08333	-0.6667	0	0.66667	-0.0833	f(x+1)
0	0	0	0	-0.5	0	0.5	f(x+2)
0	0	0	0	0	0	0	f(x+3)

=	0	
≈	**df/dx (x-2)**	O(2)
≈	**df/dx (x-1)**	O(4)
≈	**df/dx (x)**	O(6)
≈	**df/dx (x+1)**	O(4)
≈	**df/dx (x+2)**	O(2)
=	0	

Figure 2.11: (Left) Maximum-order FDM for a 1D chain of 7 points. Each row has the highest finite difference scheme available given the existing neighbors (neglecting the edges). (Center) The array of point values to be multiplied against the FDM. (Right) The result of multiplying the FDM with the array of values, and associated accuracy of the finite difference approximation.

As a solution to these numerical issues, we utilize the same prior FDM method used in previous calculations but use multiple shells for the finite difference approximation. Such a scheme was originally proposed in Ref. [123]. In principle the change is simple, however the implementation of this scheme requires a complex algorithm to maintain the highest possible accuracy near the edges of the finite k-space grid. While the use of a nearly arbitrary number of nearest neighbor shells is possible in the center of the grid, near the edge not all neighbors are defined. This leaves two options: effectively decrease the size of the grid by neglecting points near the edges without a fully defined number of shells, or adjust the FDM scheme near the edges such that the number of shells used for any point corresponds to the largest number of nearest neighbor shells defined. Since the first option effectively wastes computational power, we chose the second approach. Using the FDM shown in Fig. 2.1 as a reference, we show a schematic high-order FDM using this scheme in Fig. 2.11.

To determine the shell weights, an analytical method cannot be used (such as the method used to derive the weights in Fig. 2.11) since the combination of a BCC Monkhorst-Pack mesh for Si and the use of multiple nearest-neighbor shells leaves low-order mixed partial derivatives which cannot be eliminated using a finite number of shells. To overcome this limitation, we solve the shell weights for a selected electronic band by the minimization of an objective function measuring the difference between exact and approximate derivatives, weighted by the equilibrium distribution function to boost accuracy near the points with the highest occupation through the warm carrier regime. We used the following equation:

$$\text{Error}(T, \{w_b\}) = \frac{\sum_\lambda \left(\left[\frac{\partial f_\lambda^0}{\partial k_\gamma} \right] - \left[D_\gamma(\{w_b\})\, f_\lambda^0 \right] \right)^2 f_\lambda^0}{\sum_\lambda \left[\frac{\partial f_\lambda^0}{\partial k_\gamma} \right]^2 f_\lambda^0} \tag{2.41}$$

where $\frac{\partial f_\lambda^0}{\partial k_\gamma}$ is the analytical derivative of the Fermi-Dirac function f_λ^0 and $D_\gamma(\{w_b\})$ is the FDM representation of the operator $\frac{\partial}{\partial k_\gamma}$. The temperature-dependence of the objective function arises from the temperature-dependence of f_λ^0. The FDM is defined using $\{w_b\}$, which is the set of shell weights and are the minimization parameters, subject to the constraint $\sum_b w_b = 1$. The subscript b identifies the nearest-neighbor shell. We define the total number of shells in a scheme by B.

As a visual representation of this optimization scheme, we show both $\partial f^0/\partial k_x$ versus energy and its absolute value at both 300 K and 77 K in Fig. 2.12. We observe that the FDM reproduces the analytical results with generally quantitative accuracy, there being only a few outlying points near the edges of the k-space grid. With shell weights optimized to each temperature, accuracy is also maintained at both 300 and 77 K.

It was found that relative to the one-shell case ($B = 1$) at $T \leq 77$ K, the error defined by Eq. 2.41 decreased by 96% with the inclusion of three shells ($B = 3$), and by a further 77% with seven shells ($B = 7$). These accuracy gains are reflected in Fig. 2.13, where order-of-magnitude decreases in the error are observed for the inclusion of 3 and 7 shells. For only 2, 4, 5, and 6 shells, negligible decreases in the error are observed. Similarly, beyond seven shells, the gain in accuracy was negligible.

We show the effect of this higher-accuracy FDM in Fig. 2.10. Moving right through any row increases the number of shells used in the scheme, and a clear reduction in both negative occupation and outliers is observed. This apparently solves the issue underlying the divergence of calculations and the resulting transport quantities. To be sure, however, we also compare transport properties to find the minimum number of shells required to maintain accuracy. We compare the high-field DC mobility in different cases via RMS difference (defined as $||y_1 - y_2||_2 \,/\, ||y_1||_2$, where y is the property of interest). The mobility obtained using $B = 3$ and $B = 7$ agreed with the $B = 1$ case to within 2.1% even at 20 K and up to 10 kV cm^{-1}. The RMS difference between $B = 3$ and $B = 7$ was 0.3%. This agreement indicates that, despite being optimized to accurately calculate the gradient of the Fermi-Dirac function f_λ^0, the

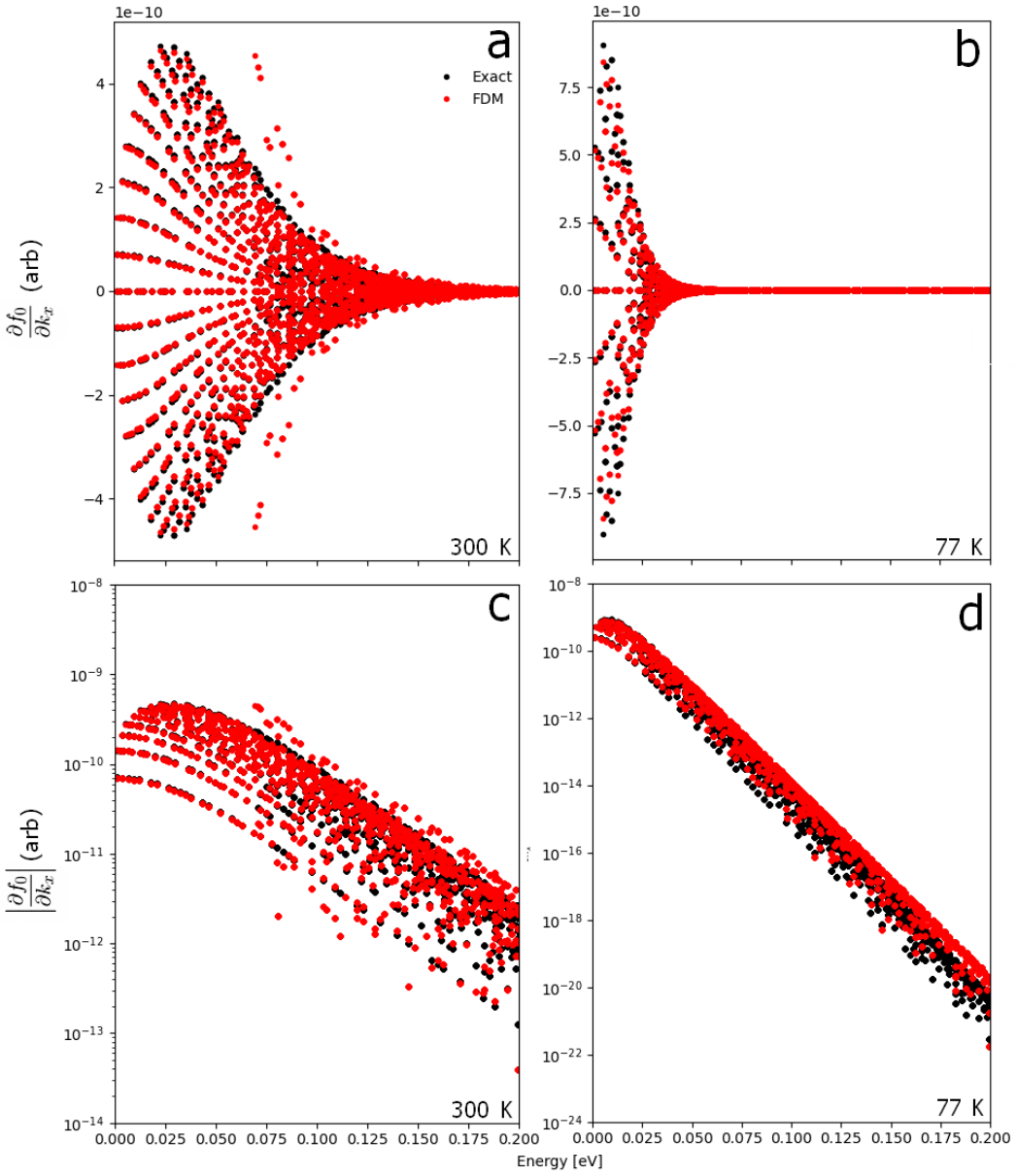

Figure 2.12: (a) and (b) Partial derivative of the Fermi-Dirac distribution with respect to momentum in the x-direction at 300 K and 77 K, respectively. FDM-calculated values shown in red, and exact values are shown in black. (c) and (d) Same data as in (a) and (b) but in absolute value.

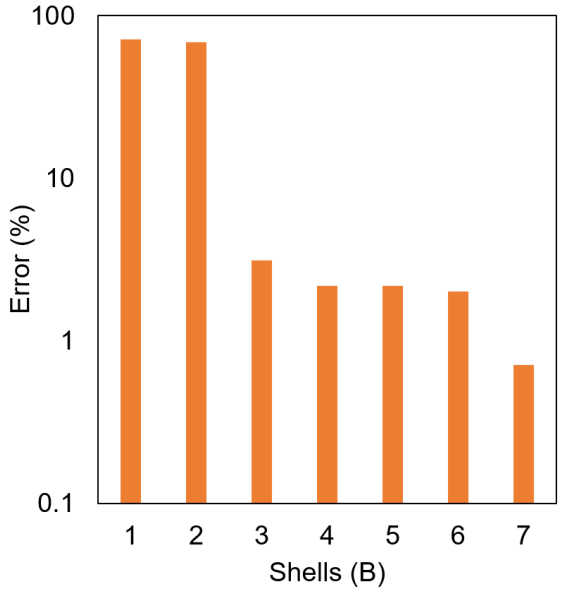

Figure 2.13: Error according to Eq. (2.41) multiplied by 100% for various numbers of nearest neighbor shells. Order-of-magnitude decreases are observed for the inclusion of 3 and 7 shells, while including only 2, 4, 5, or 6 shells results in very little accuracy gains.

	Shell (b)						
Total shells (B)	1	2	3	4	5	6	7
1	1.000						
2	0.725	0.275					
3	1.390	0.530	-0.920				
4	1.270	0.600	-0.490	-0.380			
5	1.280	0.590	-0.480	-0.370	-0.020		
6	1.310	0.590	-0.420	-0.680	0.030	0.170	
7	1.380	0.730	-0.330	-0.980	-0.450	0.100	0.550

Table 2.1: Calculated FDM shell weights w_b using Eq. (2.41) and $T = 77$ K for various numbers of shells B.

higher-order FDM still provides an accurate result when applied to the hot carrier distribution function f_λ.

For noise properties, however, $B \geq 3$ was found to be necessary to remove numerical artifacts. Therefore, we used $B = 3$ at 77 K and $B = 7$ for $T < 77$ K. For points near the edge of the defined grid for which the default number of shells (B) is not possible, we used the maximum number of shells with fully defined neighboring points. For uniformity, the shell weights were calculated using $T = 77$ K, as temperature had only a negligible effect on $\{w_b\}$. For example, calculating $\{w_b\}$ for $B = 7$ at $T = 20$

K results in an RMS difference in the 20 K drift velocities of only 3.7% compared to calculations using shell weights optimized at 77 K. Shell weights w_b for each value of b and B are as shown in Table 2.1.

The algorithm to apply this approach for a 3D BCC system with multiple, separate bands was written to function as follows:

1. A loop is initiated over the shells, starting from the largest shell and decremented to the smallest. A list is initialized to track which k-points have valid neighbors in this shell.

2. Another loop is initiated over the electronic bands. Because charge carriers cannot be moved between bands without scattering, states should only be linked within each individual band. Points from each band are pulled from the master dataframe and used for the remainder of this loop.

3. A final loop is initiated over each k-point.

4. The following is attempted:

5. The shell neighbors are found and their respective weights are pulled from a pre-calculated dataset. Shell weights are assigned according to the highest scheme possible for this k-point. Meaning, if this k-point has defined neighbors up to shell B, then the shell weights used are those defined for B. However, if the point is near the boundary of the grid such that not all shells up to B are fully defined, the accuracy scheme is reduced to the highest number of shells available. Meaning if $B = 7$ but only 3 shells are valid, the shell weights for $B = 3$ are used for this point.

6. If the above fails, it means that the k-point does not have a full set of defined neighbors in the given shell for the energy window used in the calculation. In this case, nothing is done.

Cryogenic computational details

For the calculations in the remainder of this chapter, the numerical details are as follows. Band structure and phonon calculations were performed in Quantum ESPRESSO [129] as in Ref. [138]. Fine-grid interpolation and scattering rate calculations were performed via Perturbo [22]. A 250^3 ($250 \times 250 \times 250$) grid with 2.5 meV Gaussian smearing were used for $T > 6$ K, and 325^3 grid with 1.25

meV smearing for $T = 6$ K. Increasing the Gaussian width to 1.55 meV at 6 K resulted in a maximum change in drift velocity of 1.7% at any field. The energy windows for scattering rate calculations were 80 and 57 meV for $T > 6$ K and $T = 6$ K, respectively. Increasing the energy window to 90 meV at 77 K and a grid of 180^3 resulted in a 3% difference at the maximum field studied (10 kV cm^{-1}), and increasing the window to 70 meV at 6 K and a grid of 200^3 resulted in a similar 3.5% difference at 0.84 kV cm^{-1}. Only the heavy holes were included to reduce computational costs; it was found that at 77 K omitting the light hole band resulted in an RMS difference of only 1.5% compared to results with both the heavy and light holes, and this error decreases with decreasing temperature owing to the decreasing occupation of the light and split-off bands.

2.5 Results: properties at cryogenic temperatures

Drift velocity

We first investigate the drift velocity characteristics between 6 and 45 K; we show these drift velocity-field curves in Fig. 2.14. We observe that the *ab-initio* calculations reproduce two experimentally observed regimes of velocity saturation. At $\lesssim$ 10 V cm^{-1}, the drift velocity increases linearly with field following the Ohmic trend, followed by an increase with lesser slope from 10 - 200 V cm^{-1} corresponding to an anomalous saturation regime. At $\sim$ 200 V cm^{-1}, the drift velocity increases further with nearly the same slope as in the Ohmic regime, but eventually enters another saturation regime at $\sim$ 500 V cm^{-1}. Near-quantitative agreement with experiment is achieved to within 8% (RMS) over all temperatures. This agreement, achieved by only considering e-ph scattering, indicates that ionized impurity scattering is negligible in the high-purity samples ($\gtrsim$ 100 kΩ cm) even at cryogenic temperatures, as originally concluded in the experimental studies [7, 8].

To gain insight into the origin of the low-field saturation regime, we show the calculated hole-phonon scattering rates versus energy in Fig. 2.15a. In the following discussion, we focus only on the 20 K case for simplicity. At this temperature, we observe that the scattering rates increase rapidly with increasing energy; from hole energies of 0 to 20 meV there is an increase in scattering rates by a factor exceeding 200. However, from 20 to 60 meV the rates are relatively constant, only rising by a factor of 4. Above 60 meV optical phonon emission becomes possible and the scattering rates again rapidly rise with energy.

These differing trends below and above $\sim$ 20 meV arise due to two factors. First,

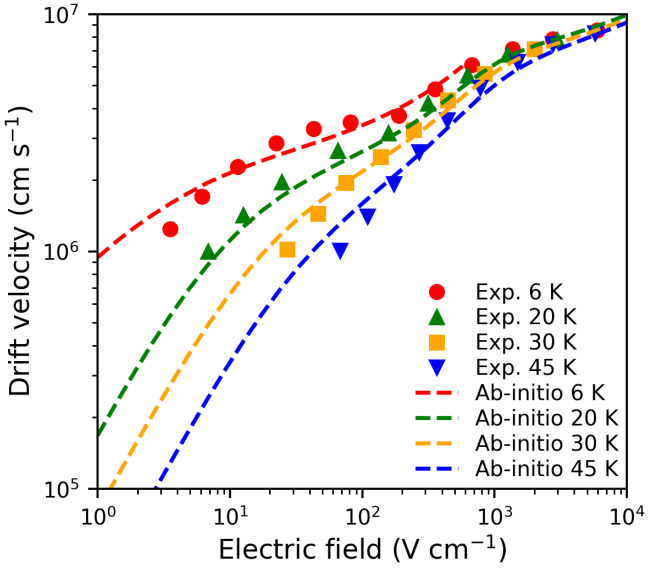

Figure 2.14: Hole drift velocity versus electric field in the [100] direction. Experimental values from Ref. [7] (6 K as red circles, 20 K as green upward triangles, 30 K as yellow squares, 45 K as blue downward triangles). Calculated values also shown (dashed lines with identical color scheme to experiment).

below $\sim$ 40 K, the population of zone-edge acoustic phonons, which have the largest density of states among acoustic phonons, rapidly diminishes with temperature. Consequently, the acoustic phonon absorption rate approaches zero while the acoustic phonon emission rate approaches a constant, which causes a large disparity in scattering rates between low and high energies where absorption and emission are dominant, respectively. Second, the phonon density of states, which increases quadratically with energy up to a maximum at $\sim$ 20 meV [139], causes a corresponding increase in scattering rates with energy from 0 – 20 meV. These factors together result in an strongly temperature-dependent increase in scattering rates from 0 to $\sim$ 20 meV and relatively constant rates at higher energies up to $\sim$ 60 meV.

We next examine the occupation function at various fields to establish which hole energies and corresponding scattering rates are relevant when the saturation feature occurs. We plot the hole occupation function versus energy and applied electric field in Fig. 2.15b. At 1 V cm^{-1}, we observe that nearly all holes are confined to energies less than 10 meV, and the hole occupation exhibits a clear dependence on temperature. For sufficiently strong electric fields ($\gtrsim$ 10 V cm^{-1}), the weight of the distribution shifts towards 10-30 meV as shown in Fig. 2.15b at 100 V cm^{-1}, where the slope of drift velocity with field reaches a local minimum. In this energy range, we observe the rapid increase in scattering rates due to zone-edge acoustic phonon

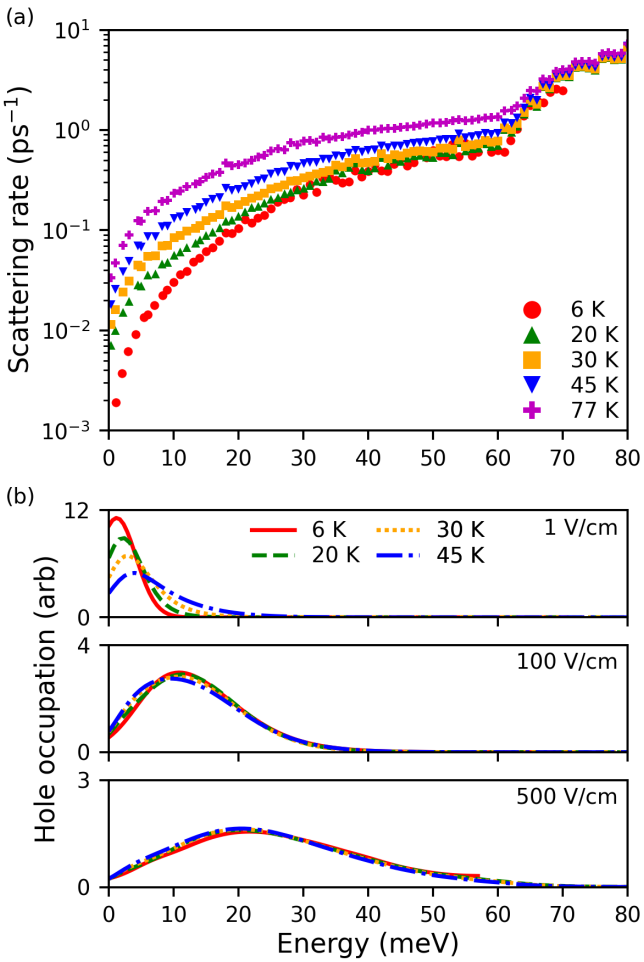

Figure 2.15: (a) Calculated hole-phonon scattering rate versus energy from the valence band maximum at temperatures of 6 K (red circles), 20 K (green upward triangles), 30 K (yellow squares), 45 K (blue downward triangles), and 77 K (magenta crosses). (b) Hole occupation function versus energy from the valence band maximum at various electric fields applied in the [100] direction. The occupation is obtained using a kernel density estimate. Colors correspond to the same lattice temperatures as in (a). Data at 6 K are shown up to the 57 meV energy window at that temperature.

emission. At 500 V cm^{-1}, shown also in Fig. 2.15b, the hole distribution has weight in the 30-60 meV region, where scattering rates are relatively constant. Above 500 V cm^{-1}, some holes have energy exceeding $\sim$ 60 meV and may undergo optical phonon emission processes.

We may now explain the relationship between acoustic phonon scattering and the first regime of drift velocity saturation. At low fields ($\lesssim$ 10 V cm^{-1}), the drift velocity is linear with field corresponding to the Ohmic regime, as holes are approximately in equilibrium with the lattice and the mean scattering rate remains independent of field, a trend which occurs at all temperatures. However, at cryogenic temperatures and high fields ($\sim 40-200$ V cm^{-1}), carrier heating shifts the occupation to energies where the scattering rates are 1-2 orders of magnitude larger than those relevant at low fields. The higher scattering rates at these energies more than compensates the higher band velocity, causing a decrease in mobility and the drift velocity saturation.

At higher fields, above $\sim$ 200 V cm^{-1}, the increasing band velocity with energy compensates the relatively smaller increase in scattering rates. Therefore, the saturation "shoulder" ends, and drift velocity again increases with increasing field. Finally, at about $\sim$ 500 V cm^{-1}, optical phonon emission begins and another regime of drift velocity saturation occurs. At higher temperatures $\gtrsim$ 77 K, the scattering rates below 20 meV do not show a pronounced increase, and therefore the anomalous saturation regime does not occur. From these findings, we conclude that it is the energy-dependence of the acoustic phonon scattering rates at cryogenic temperatures which cause the saturation "shoulder" in *p*-Si between 10 and 200 V cm^{-1} for $T \lesssim 40$ K, in agreement with a prior work [126].

Power spectral density

We now turn to the non-monotonic trend of the microwave PSD versus electric field. This feature appears in the experimental 10 GHz PSD, which first increases and then decreases with an increasing electric field, leading to a peak at around 20 V cm^{-1} [54, 128]. We have calculated the 10 GHz PSD for longitudinal and transverse measurement directions ([110] and [1$\bar{1}$0], respectively) versus [110] electric field strength, shown in Fig. 2.16. Normalized values are shown to facilitate the comparison of trends. The absolute PSD values would be uniformly overestimated by around 25% based on previous calculations of the mobility and diffusion coefficient and considering the Nyquist and Einstein relations linking the PSD, diffusion coefficient, and mobility at equilibrium [138]. The calculations do not agree quan-

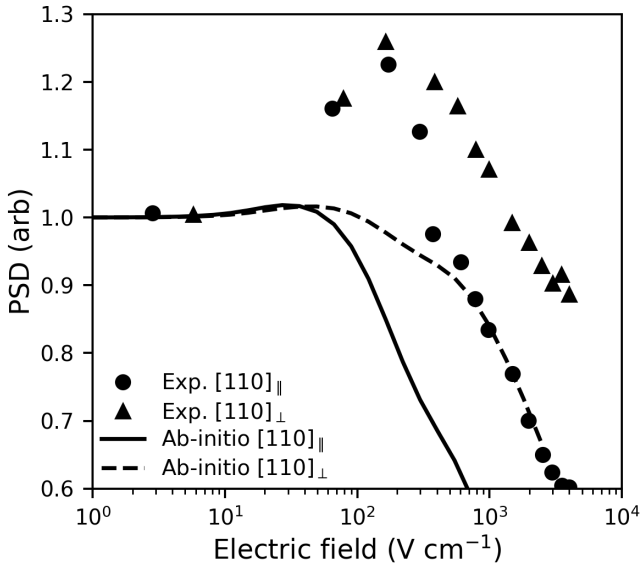

Figure 2.16: 80 K PSD of current noise versus electric field applied in the [110] direction at 10 GHz. Experimental values from Ref. [128] (measurements taken parallel to [110] as upward triangles, measurements taken in the transverse direction $[1\bar{1}0]$ as circles). Calculated data also shown (parallel ($\|$) as solid line, perpendicular ($\perp$) as dashed line).

titatively with experiment but show a qualitatively similar non-monotonic trend. A firm conclusion regarding the origin of the discrepancy is difficult to draw owing to discrepancies between experimental reports (c.f. Fig. 1b of [54] and the various other experimental reports of the diffusion coefficient, namely Fig. 2a of Ref. [133] and Fig. 3 of Ref. [55]) and the fact that only one reference exists for this particular data set. In the following discussion, we therefore consider the qualitative experimental trends rather than focusing on quantitative agreement.

Previous studies have attributed the trend to the competition of carrier heating (increasing PSD) and decreasing relaxation time (decreasing PSD) [128], as well as the convective noise mechanism which is influenced by the field-dependent energy relaxation time [12]. However, each explanation has inconsistencies. Regarding the first explanation, we note that the 10 GHz PSD measurements by Ref. [54, 128] were used to calculate the diffusion coefficient, which is valid only in the low-frequency limit [56] ($\omega\tau_m \ll 1$, where τ_m is the momentum relaxation time appearing in the Drude conductivity expression [140]). In this limit, an increase in transport properties with increasing electric field due to carrier heating would be expected in not just the PSD but also in DC quantities such as mobility. However, the hole mobility in Si is observed to decrease with increasing field. Therefore, this explanation is

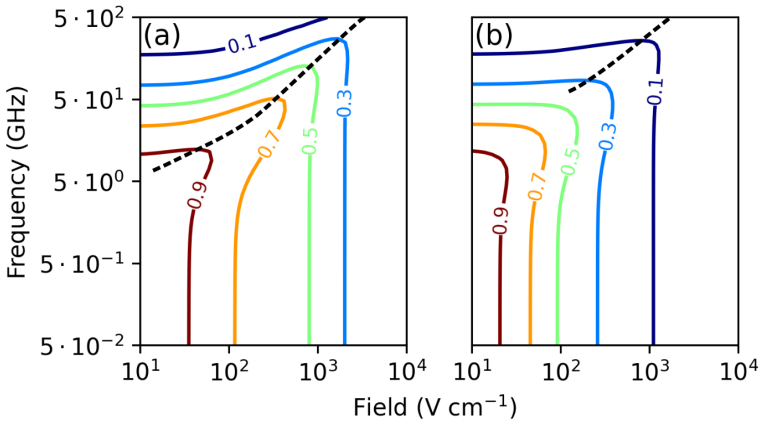

Figure 2.17: (a) PSD versus frequency and electric field. Above approximately 7 GHz, a peak occurs in the PSD versus field data, represented by a "ridge" in the contour plot consisting of lines sloping upward before dropping off. The location of the peak in the PSD-field curves is shown as a dotted line. (b) AC mobility on the same axis as (a). In this case, a peak only occurs above approximately 60 GHz. The location of the peak in the AC mobility-field curves is shown as a dotted line.

inconsistent with the assumptions made in the original work and observed trends of other transport properties. Regarding the second explanation, the convective noise mechanism only affects the longitudinal PSD, not the transverse PSD (see section 7.2 of Ref. [12]). Because the PSD peak appears in both measurement directions, the convective mechanism cannot be responsible for the peak. Therefore, the underlying cause of the non-monotonic PSD feature remains unclear.

To identify the origin of the peak, we calculated the PSD versus both electric field and frequency. The result is shown in Fig. 2.21a. The longitudinal PSD calculation in Fig. 2.17a corresponds to a horizontal slice of this plot at 10 GHz. The location of the peak, given by the dotted line, is observed to depend on both electric field and frequency. Because the peak is observed in our calculations which include only the heavy hole band, interband scattering is ruled out. Additionally, the feature is also observed when optical phonons are omitted, eliminating carrier streaming noise as the origin (see Sec. 7.4 of Ref. [12]). Therefore, we conclude that the peak must arise from qualities of the hole and phonon dispersion and acoustic phonon scattering rates.

Knowing that the convective mechanism cannot be responsible for the PSD peak, and without any other mechanism by which energy relaxation may produce the feature, we take as a working hypothesis that the energy-dependence of the momentum relaxation time leads to the trend. However, within the fully *ab-initio* framework,

testing this hypothesis is difficult. Furthermore, the physics underlying the PSD are hard to capture in a more qualitative model, compared to a simpler quantity such as the AC mobility. However, the PSD and AC mobility do share similarities as they are related at low fields through the Johnson-Nyquist relationship. In fact, we observe that a similar peak occurs in the *ab-initio* AC mobility, as shown in Fig. 2.17b. While the "ridge" feature in the PSD, which gives rise to the peak, is not as pronounced, it does still occur in the AC mobility. Additionally, for the peak to occur it must need be that $\partial^2 S_j(\omega, E)/\partial E^2 > 0$ at low fields. Since at these fields the Nyquist relationship is approximately valid, it must also mean that $\partial^2 \mu_{AC}(\omega, E)/\partial E^2 > 0$, so an investigation of the AC mobility, a much simpler quantity to understand than the PSD, may yield an answer as to the origin of the field-dependent peak in both quantities.

The AC mobility can be modeled with various levels of approximation. In order to test whether the momentum or energy relaxation time is responsible for the peak, we first try a model which includes both of these quantities. Here, we treat the mean velocity and mean energy of the holes as they evolve over time with the Drude model:

$$\frac{d}{dt}v_{AC} = \frac{e}{m}(E_{DC} + E_{AC}e^{i\omega t}) - \frac{v_{DC} + v_{AC}}{\tau_m} \tag{2.42}$$

$$\frac{d}{dt}\epsilon_{AC} = \frac{e}{m}(v_{DC} + v_{AC})(E_{DC} + E_{AC}e^{i\omega t}) - \frac{\epsilon_{DC} + \epsilon_{AC} - \epsilon_0}{\tau_\epsilon} \tag{2.43}$$

where v_{DC} and v_{AC} are the velocities induced by the DC and AC electric fields, respectively. m is the hole mass, ϵ_{DC} and ϵ_{AC} are the energies over the thermal energy ϵ_0 induced by the DC and AC electric fields, respectively. While not immediately obvious, the two equations are linked through the energy dependence of τ_m. This system can be solved by first solving for the DC quantities when $E_{AC} = 0$. Then, the set of equations is time-stepped with a perturbing AC field by using a 4-th order Runge–Kutta scheme. Finally, with enough time steps the Fourier transform is taken:

$$\mu_{AC} = \frac{e}{E_{AC}} \int_{-\infty}^{\infty} v_{AC}(t) e^{-i\omega t} dt \tag{2.44}$$

which must be taken numerically through the fast Fourier transform algorithm for the discrete, limited simulated data. To ensure accuracy across the different orders of magnitude of frequencies, the system was simulated through a transient period followed by 20π oscillatory periods of the AC field with 1000 time steps.

As a test of this model, we simulate the *ab-initio* system to the best of our ability by using the effective hole mass and interpolating $\tau_m(\epsilon)$ and $\tau_\epsilon(\epsilon)$ from the *ab-initio*

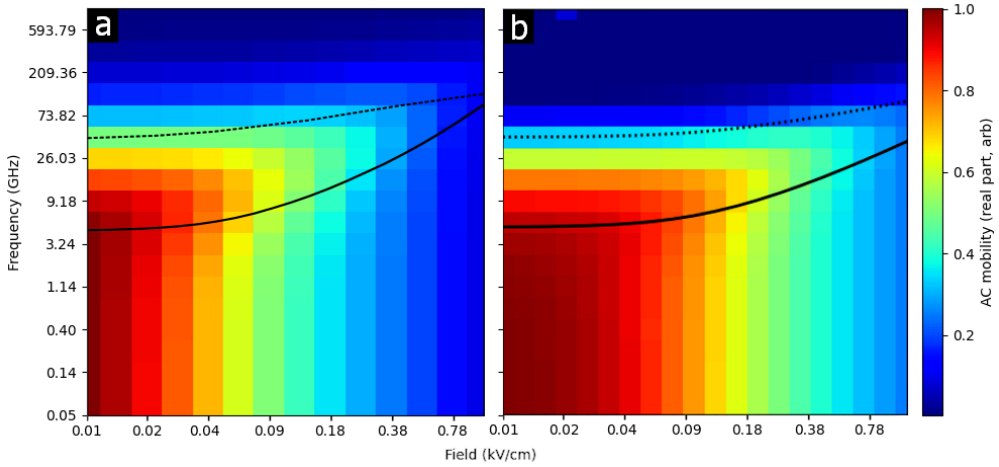

Figure 2.18: (a) Real part of the *ab-initio* 77 K AC mobility as a function of frequency and field. The energy relaxation time is shown as a solid line. (b) Modeled real part of the AC mobility at 77 K on the same axis as (a). The energy relaxation time is shown as a solid line, while the momentum relaxation time is a dashed line.

values. The results are shown in Fig. 2.18. While the results are not identical, most likely owing to the collapse of the entire system of holes into a single mean value, a peak is still observed in the field-dependent AC mobility at sufficiently high frequencies, and the "ridge" feature is qualitatively preserved.

This model is convenient as we are able to define the momentum and energy relaxation times in an arbitrary manner. Starting with the most realistic case of $\tau_m = c\tau_\epsilon$ and $\tau_\epsilon = a\epsilon^b$, we again see the ridge in Fig. 2.19a. To eliminate the possibility that the energy-dependence of the energy relaxation time is the cause, we simply set τ_ϵ to a constant and shift the energy dependence into τ_m. This result is shown in Fig. 2.19b. In this case, the ridge is only qualitatively changed, and a peak still occurs in the field-dependent AC mobility. Furthermore, we show that the peak still occurs regardless of the value of the energy relaxation time by setting it to a value much smaller than τ_m (an unphysical but mathematically possible scenario) and a value much larger than τ_m, which results are shown in Fig. 2.19c and Fig. 2.19d, respectively. While the changes to the ridge in each case are dramatic owing to the changes in hole heating (being suppressed and increased, respectively), the peak still occurs with $\partial^2\mu_{AC}(\omega, E)/\partial E^2 > 0$ at low fields for sufficiently high frequencies. Therefore, we conclude that, while the energy relaxation time plays an important role in the shape and position of the peak, a peak in the AC mobility versus electric field (and similarly the PSD), will always occur for sufficiently high frequencies given that τ_m decreases with carrier energy.

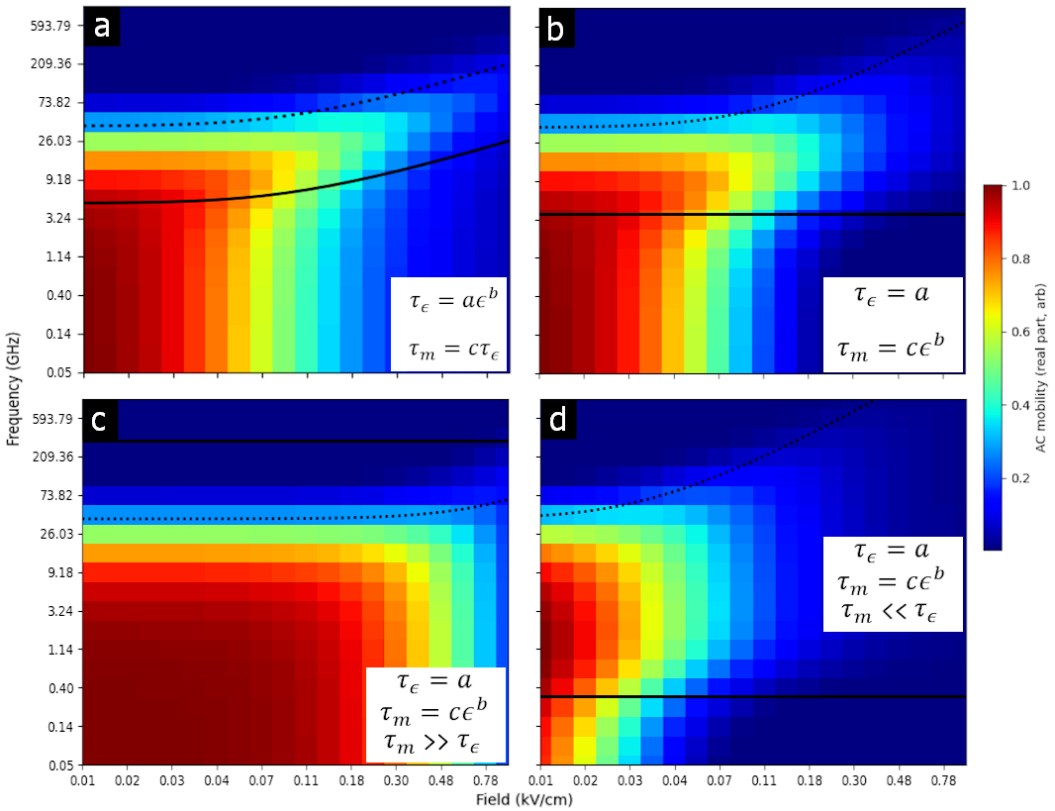

Figure 2.19: Effect of momentum and energy relaxation time on AC mobility. (a) Energy and momentum relaxation time change with the mean hole energy, the two being related by a constant. (b) τ_m changes with mean hole energy, but τ_ϵ is constant at the equilibrium value. (c) Same as (b) but τ_ϵ is set to a constant much smaller than τ_m. (d) Same as (b) but τ_ϵ is much larger than τ_m.

This effect can be understood by simplifying the model. Since we started with the differential, full form of the Drude model, we now consider the simple model derived when τ_m is constant, but as a rough approximation substitute in $\tau_m = e^{-E}$. This yields, for the real part of the AC mobility:

$$\mu_{AC} \propto \frac{e^{-E}}{1 + (\omega e^{-E})^2} \tag{2.45}$$

We show a map of this function over frequencies and fields in Fig. 2.20, with a dotted line to show e^{-E}. We see that the ridge features follows perfectly our expression for the momentum relaxation time, in fact the peak is located exactly at $\omega = 2\pi/e^{-E}$.

This behavior can be understood by inspecting the relative magnitude of the numerator $\tau_m(E)$ (e^{-E}) and the denominator $1 + (\omega\tau_m(E))^2$, which represent carrier scattering and carrier inertia [141], respectively. At sufficiently high temperatures and low frequencies such that $\omega\tau_m(E) \ll 1$, the AC mobility is proportional to $\tau_m(E)$

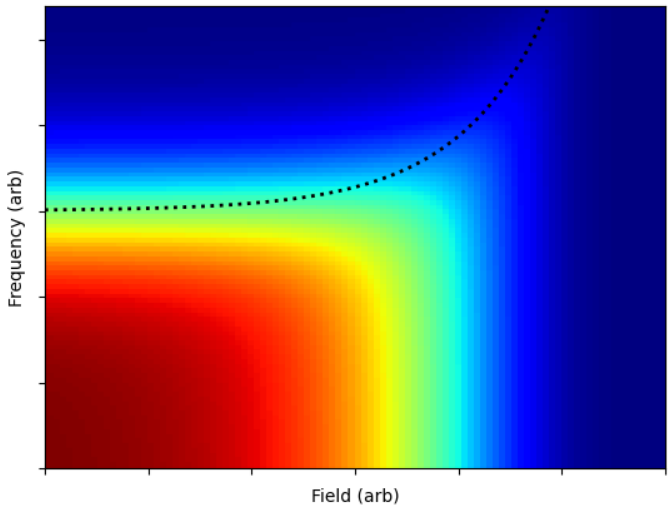

Figure 2.20: Modified Drude model incorporating the electric-field dependence of the momentum relaxation time. At frequencies where $\omega > 2\pi/\tau_m(E)$, a peak occurs in the field-dependent AC mobility at $\omega = 2\pi/\tau_m(E)$ (dotted line).

and decreases with field due to $\tau_m(E)$ decreasing. However, when $\omega\tau_m(E) \gg 1$ is satisfied, which occurs at some combinations of sufficiently low temperatures, high frequencies, and low fields, then, with increasing field, as $\tau_m(E)$ decreases the inertial term $1 + (\omega\tau_m(E))^2$ decreases faster than $\tau_m(E)$ itself. Thus, the AC mobility rises as $\mu_{AC}(\omega, E) \sim \tau_m(E)^{-1}$. Once $\omega\tau_m(E) \ll 1$ is satisfied again at high enough fields, which will occur regardless of temperature and frequency, the AC mobility again decreases with field.

We note that the role of the field-dependence of the momentum relaxation time in producing non-monotonic trends of AC mobility with electric field has been previously reported [142]. Various studies have incorporated field-dependence into the momentum relaxation time of AC mobility models and observed different trends depending on the frequency. At low frequencies such that $\omega\tau_m(E = 0) \ll 1$, the AC mobility is both theoretically predicted [143, 144] and experimentally observed [145] to decrease monotonically with increasing electric field, as expected for systems with sublinear current-voltage characteristics. However, at frequencies such that $\omega\tau_m(E = 0) \geq 1$, other studies predicted a non-monotonic dependence of AC mobility on electric field [146, 147].

Experimentally, non-monotonic trends of AC mobility with electric field have been reported for *n*-InSb [142, 148]. These experiments measured AC mobility at 77 K as a function of field from 0 – 165 V cm^{-1} and from 0 – 83.7 GHz, which includes the case $\omega\tau_m(E = 0) \approx 1$. The measurements show non-monotonic behavior when

$\omega\tau_m(E = 0) > 1$, with an initial rise in the AC mobility at low fields ($\lesssim 50$ V cm^{-1}), in contrast to the decreasing trend at lower frequencies. Furthermore, the data agree qualitatively with a hydrodynamic model [148] which predicts non-monotonicity in the high-field AC mobility for frequencies above ~ 50 GHz.

Relating the AC mobility back to the PSD, we can derive an approximation for $S_j(\omega, E)$ that is practically identical to Eq. (2.45). This simplified model comes from relating the PSD to $\tau_m(E)$ by assuming equipartition and neglecting anisotropy. The PSD then takes the form [149]:

$$S_j(\omega, E) = \frac{S_j(0, E)}{1 + (\omega\tau)^2} \tag{2.46}$$

where τ represents a characteristic relaxation time of the system (for instance momentum, energy, or intervalley relaxation), and E represents the electric field strength. A derivation of this expression, considering the constant relaxation time to be τ_m, can be found in sections 3 and 7 of Ref. [12]. A simple although less-rigorous derivation can be performed by combining the Nyquist current noise (Refs. [150, 151], Eqns. 6 and 1, respectively) and Drude AC conductivity (Ref. [140], Eqn. 1.29) to yield Eq. (2.46), also neglecting the field-dependence.

For our model, we assume a mono-energetic hole distribution characterized by a momentum relaxation time depending on electric field, $\tau_m(E)$. For simplicity, we further approximate $S_j(0, E) \propto \tau_m(E)$ as the low-frequency PSD is directly proportional to the momentum relaxation time through the fluctuation-diffusion [56] and Einstein [4] relationships. These assumptions yield:

$$S_j(\omega, E) \propto \frac{\tau_m(E)}{1 + (\omega\tau_m(E))^2} \tag{2.47}$$

Now, the Einstein relationship holds only in the low-field limit, but it remains approximately valid at fields where the carrier distribution is sufficiently close to the equilibrium one. In the present case, the mean carrier energy at 20 V cm^{-1}, where non-monotonic behavior is apparent, is only 2.2% larger than the equilibrium value, so the error arising from the use of the Einstein relationship should be on the order of this difference ($\lesssim 10\%$). Furthermore, the existence of this peak necessitates that $\partial^2 S_j(\omega, E)/\partial E^2 > 0$ at low fields, where the Einstein relationship is valid. Therefore, it is expected that Eq. (2.47) provides a qualitatively accurate description of PSD behavior at the electric fields of interest.

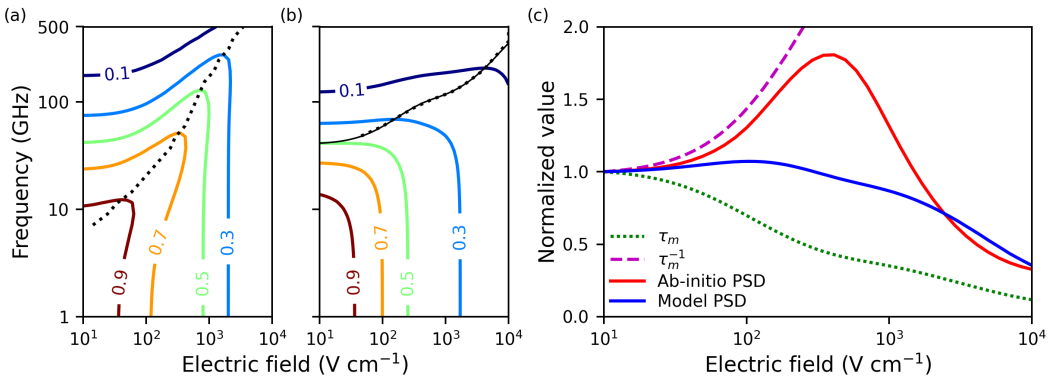

Figure 2.21: (a) Contour map of normalized *ab-initio* PSD of current fluctuations versus frequency and electric field. Location of peak in the horizontal slices (PSD vs field curves) also shown (dotted black line) (b) Contour map of normalized model PSD (Eq. (2.47)) versus frequency and electric field. An analogous peak feature is observed as the *ab-initio* PSD. Location of peak in the horizontal slices shown (dotted black line), as well as $\omega\tau_m(E) = 1$ (solid black line). (c) *Ab-initio* PSD vs. electric field in (a) (solid red line) and modeled PSD in (b) (solid blue line) at 60 GHz. The normalized momentum relaxation time is shown (dotted green line) as well as its inverse (dashed magenta line). The normalization constant for $\tau_m(E)$ is 3.86 ps.

To plot Eq. (2.47), an expression for $\tau_m(E)$ is needed. From our *ab-initio* results, we calculated the momentum relaxation time at each electric field by fitting a Lorentzian to the frequency-dependence of the transverse AC mobility with an identical functional form as in Eq. (2.47). The resulting function $\tau_m(E)$ is shown in normalized form in Fig. 2.21c.

Using this function, we compute PSD versus frequency and electric field strength using Eq. (2.47). The *ab-initio* PSD is shown in Fig. 2.21a, and the modeled result is given in Fig. 2.21b. We observe a qualitatively similar “ridge" trend as seen in the *ab-initio* PSD. Horizontal slices, which yield PSD versus field strength, taken at high frequencies display a peak, the location of which follows the same trend as in Fig. 2.21a. Within this model, the location of the peak corresponds to $\omega\tau_m(E) = 1$, providing evidence that the field-dependence of the momentum relaxation time $\tau_m(E)$ is responsible for the non-monotonic PSD trend.

We show a slice of both Fig. 2.21a and Fig. 2.21b in Fig. 2.21c, taken at 60 GHz to make the relevant features more visible. We also show the relative behaviors of $\tau_m(E)$ and $\tau_m(E)^{-1}$, for reference. We observe that at low fields, both the modeled and *ab-initio* PSD exhibit $\tau_m(E)^{-1}$ behavior, increasing with electric field, as described previously. Furthermore, the PSD follows $\tau_m(E)$ behavior at high

fields, decreasing with electric field. These different trends enable a peak in the PSD, driven solely by the field-dependence of the momentum relaxation time.

Since the AC mobility is proportional to the PSD at low electric fields through the Nyquist relationship, the prior findings regarding the non-monotonic trend in AC mobility are consistent with our conclusions regarding the PSD. On the other hand, prior studies of the microwave PSD concluded the non-monotonic trend was due to a competition between carrier heating and decreasing relaxation time with increasing field [128], and convective noise [12]. While carrier heating is not exclusive of the momentum relaxation time decreasing, it is not as specific a mechanism. Our study and prior AC mobility studies support that the field-dependence of the momentum relaxation time is the only necessary condition to enable this non-monotonic trend.

We now discuss why the *ab-initio* PSD results display a peak even when $\omega\tau_m(E = 0) \gtrsim 1$ is not satisfied, a condition strictly necessary for a peak to appear in the model. In a real system, the hole distribution is not characterized by a single energy, as was assumed in the model. Therefore, although the momentum relaxation time $\tau_m(E)$ may satisfy $\omega\tau_m(E) \sim 1$, the lifetime of some states $\tau_\lambda = \Theta_{\lambda,\lambda}^{-1}$ span a range of values of $\omega\tau_\lambda$. Therefore, even at frequencies where $\omega\tau_m(E = 0) < 1$, for the system as a whole, some electronic states for which $\omega\tau_\lambda \gg 1$ have non-negligible occupation. The carriers in these states then contribute to the occurrence of a non-monotonic PSD trend, even at lower frequencies than are required to satisfy $\omega\tau_m(E = 0) \gtrsim 1$.

2.6 Discussion

Previous studies of both polar and nonpolar semiconductors using the formalism described here have reported that single-phonon scattering is insufficient to reproduce a number of experimental trends [85–87]. Therefore, it comes as a surprise that this level of theory provides quantitative agreement for most normalized transport properties with experiment in p-Si. This finding indicates that momentum and energy relaxation scattering processes of hot holes in Si are adequately described by the lowest level of pertubation theory in the electron-phonon interactions used in prior works for non-polar semiconductors [24, 82, 83]. Additionally, the relative differences in curvature of the valence band structure in different crystallographic directions appear to be captured as evidenced by the agreement of the high-field anisotropy.

There is no obvious answer as to why the theory works well for this material

system but not *n*-GaAs [85] or *n*-Si [86, 87]. However, there are a number of significant differences between the systems, which must necessarily be related to the discrepancy in findings. Namely, *p*-Si does not have multiple valleys, whether degenerate (as in *n*-Si) or spaced by a small energy gap (as in *n*-GaAs). While multiple bands are relevant to transport in *p*-Si, they all gather at Γ in momentum-space. In the other material systems, there is a wide swath of virtual energy states between distinct conducting band pockets or valleys that could be accessed through two-phonon scattering. However, in this system, all states are relatively close in momentum and therefore are readily accessible by single-phonon scattering events. To investigate this hypothesis, additional material systems will need to be investigated. Ideally, the results would first be reproduced for similar systems such as Ge. Calculating transport properties for *p*-GaAs would provide a test of whether the results here hold for polar materials with a similar bandstructure. Finally, measuring and calculating the transport properties of more exotic materials such as IV-VI semiconductors would test whether the single-phonon theory holds for *p*-type multi-pocket semiconductors.

As in low-field studies [82, 83], absolute transport properties are still uniformly overestimated by $\sim$ 25% at all fields. The low-field mobility overestimate has previously been attributed to an inaccurate valence band structure [83]. Examination of our valence band structure and that of Ref. [83] (Fig. 2b, 'SOC' case) indicates that the two are in quantitative agreement to within 5% as measured by the average root-mean square difference of the dispersions, excepting the heavy holes in the $\Gamma-K$ direction which exhibit a $\sim$ 20% heavier mass compared to those in Ref. [83]. This difference is several times smaller than the difference with the required dispersion which yields a mobility in agreement with experiment. Additionally, our computed scattering rates are in similar quantitative agreement with prior literature, with the values falling within the range of those reported in Fig. 6b of Ref. [82]. Therefore, our results support the findings from low-field studies in which the overestimated transport properties can be attributed to inaccuracies in the DFT valence band structure.

The findings at cryogenic temperatures demonstrate the usefulness of *ab-initio* calculations as a means for discovering and understanding emergent transport phenomena. While the theory behind a non-monotonic trend in the PSD driven by the energy-dependence of the momentum relaxation time existed, the level of analysis achievable through these calculations was useful in ruling out every other potential

cause. Furthermore, finding that the "shoulder" in the cryogenic drift velocity arises from the acoustic phonon scattering rates was only possible thanks to the detailed picture of both the scattering rates and field-dependent occupation function obtained through calculations such as these. While no model is yet perfect and experiments must be done to validate predictions, no set of experiments can yet probe the microscopic phenomena underlying transport to such a fine resolution as can be achieved through *ab-initio* calculations. Therefore, this technique may provide useful for both materials discovery, analysis of experimental findings, and in informing the physical models used for device simulation.

2.7 Summary

We have presented a study of hot hole transport and noise in silicon using a recently developed *ab-initio* formalism. We find that the calculations quantitatively reproduce various experimental trends in the DC mobility, carrier diffusion coefficient, energy relaxation time, PSD, and drift velocity up to 20 kV $cm^{-1}$and from 300 K down to 6 K. Absolute properties are generally overestimated by $\sim 25\%$, consistent with prior low-field studies. This agreement may be improved by the use of a more accurate valence band structure.

Furthermore, we have investigated the origin of anomalous high-field transport and noise characteristics in *p*-Si at cryogenic temperatures using a modified high-field formalism for *ab-initio* charge transport. We find that the additional regime of drift velocity saturation that occurs for $T < 40$ K is due to acoustic phonon emission, in agreement with a prior work. We also find that the peak in the power spectral density of current fluctuations which occurs at 77 K and 10 GHz is due to the field-dependence of the momentum relaxation time, contrary to the conclusions of prior studies.

This work highlights the use of high-field transport and noise properties not only as a rigorous test of the theory of electron-phonon interactions in semiconductors, but also as a tool to understand the microscopic phenomenon underlying transport and noise in semiconductors. With further investigation it may be possible to find an origin for why single-phonon scattering is sufficient here but not in other material systems, a critical question if calculations such as these are to be used for materials discovery. It is evident, however, that this technique is useful for probing the microscopic origins for phenomena which require accurate models for today's semiconductor devices.

Chapter 3

A NEW RECIPE FOR ATOMIC LAYER ETCHING OF SiO_2

This chapter has been adapted from

David S. Catherall, Azmain A. Hossain, Anthony J. Ardizzi, and Austin J. Minnich. Atomic layer etching of SiO2 using sequential exposures of Al(CH3)3 and H2/SF6 plasma. *Journal of Vacuum Science & Technology A*, 42(5):052605, 09 2024. ISSN 0734-2101. doi: 10.1116/6.0003793. URL https://doi.org/10.1116/6.0003793.

D.C. co-designed the research, conducted the calculations, analyzed the data, and wrote the manuscript.

3.1 Introduction

Atomic layer etching (ALE) is a dry etching process of increasing interest owing to its ability to solve many of the issues outlined in Sec. 1.2. First, it exhibits extremely fine atomic-scale control and selectivity [98, 152–156], allowing for precise etch depths (typically with a resolution between 0.1 and 10 Å per process cycle [98]) and the protection of both masks and other materials incorporated into complex device structures where near-infinite selectivity is desired [96, 152, 157]. ALE also has the rather unique ability among etch processes to smooth surfaces down to the sub-nanometer scale [158–160], a feature which could reduce interface losses, thickness variations, and surface roughness in all types of devices.

In contrast to continuous etching processes such as RIE, ALE consists of two or more self-limiting surface treatments [98, 152–154]. Whereas a normal chemical etchant will continuously react with a surface (as shown in Fig. 1.2), a self-limiting reaction effectively terminates itself after a certain amount of reaction has occurred. This happens through one of two mechanisms: either the reactant binds only to specific surface sites and therefore cannot react further once all sites are used, or the reaction product forms an effective diffusion barrier against the reactant. The natural oxidation of aluminum metal is an everyday example of a self-limiting reaction, in which Al_2O_3 prevents the diffusion of oxygen and water to the metal-oxide interface.

A schematic of a typical ALE process is shown in Fig. 3.1. In the first self-limiting step, the surface of a material is chemically modified by exposure to a reactant such

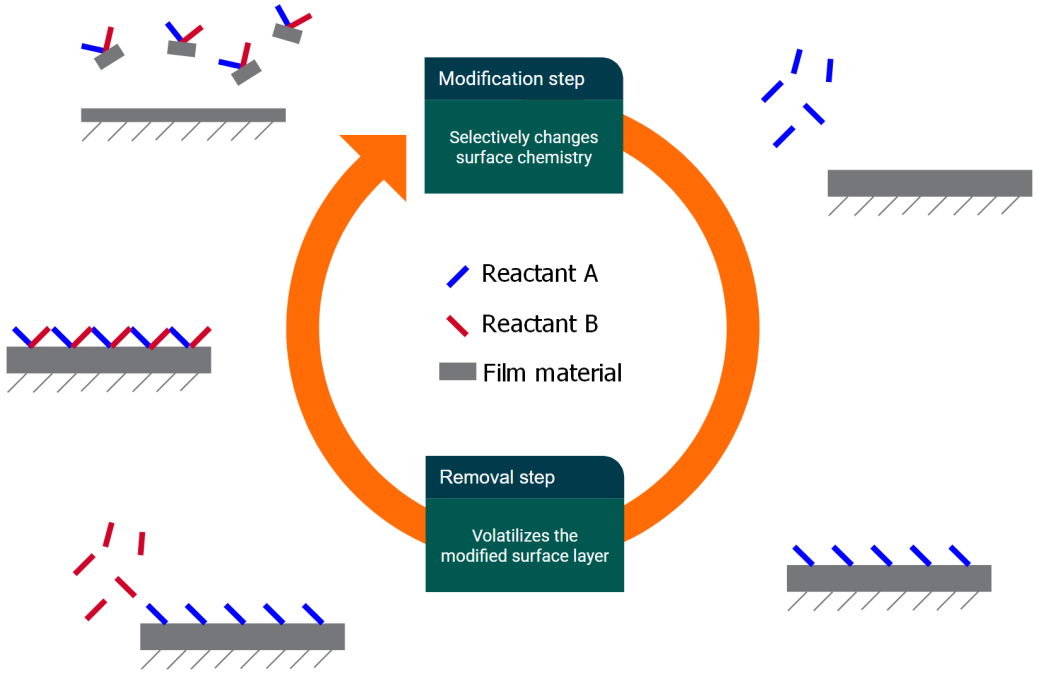

Figure 3.1: The cycle of atomic layer etching. First, a modification step utilizes a self-limiting reaction to change the surface chemistry. Here, reactant A reacts with the surface. Second, a volatilization step uses removes the modified surface by another self limiting chemical reaction, ion bombardment, or heating. Here, reactant B reacts with the modified surface, and forms a volatile compound.

as a gas, plasma, organometallic vapor, or chelating agent. A second step volatilizes only the modified material, and there are a few different means to accomplish this: One, a chemical reaction occurs with a second reactant which forms a volatile compound with the modified surface layer. Two, thermal cycling is performed if the modified surface is volatile at a higher temperature than it was formed. Three, ion bombardment is performed if the bulk of the material is bound together more strongly than to the modified surface, though this method requires careful control of the incident ion energies. In theory, other removal mechanisms are possible including electron or photon-induced reactions [98]. In Fig. 3.1, volatilization is achieved through chemical reaction using a second reactant.

The two ALE steps can then be repeated as many times as desired to achieve a specific etch depth (it is worth noting that some processes require intermediate reaction steps, meaning the total number of steps per cycle is more than two). While ALE is slower than typical wet or dry etches (achieving $\sim 0.1 - 10$ Å/min versus $10 - 1000$ Å/min) its numerous advantages have made it a very active area of research over the past decade. The materials with known ALE processes now include metals

(including Co [161], Cu [162–164], and W [165, 166]), semiconductors (including Si [167, 168], InP [169, 170], InGaAs [109], and GaAs [170–172]), dielectrics (including Al_2O_3 [173–176], SiO_2 [174, 177–179], and HfO_2 [174, 180]), optical materials ([101, 102]), and superconductors (TiN [107], NbN [108]).

Etching methods for SiO_2 are of particular interest in nanofabrication owing to the presence of SiO_2 in semiconductor, superconductor, and optical devices. Processing of SiO_2 with low damage and surface roughness is especially critical when it is the active material in a device, as is the case for on-chip photonic devices such as microcomb systems, microresonator gyroscopes, and microwave sources [181, 182]. These devices all rely on resonators such as silica microresonators which now exhibit quality factors (Q) as high as 10^9 [182, 183], where Q is defined as the ratio of center resonance frequency to the resonance bandwidth. The maximum theoretical Q for these microresonators is $\sim 8 \times 10^9$, however; the difference between this maximum value and the lesser value achieved in practice has been attributed primarily to surface roughness created by fabrication processes [183, 184]. Therefore, to increase the Q, an etch process capable of smoothing to sub-nanometer length scales is needed. ALE has potential to fulfill this need; although ALE etches too slowly to be used as the primary processing etch, it could be used to increase the Q of these devices as a post-processing smoothing step.

Since we intend to develop a recipe primarily for surface smoothing, an isotropic etch is desired. Anisotropic ALE is possible in general but is not within the scope of this work, so we will discuss isotropic etches only. There are two currently known classes of isotropic ALE processes for SiO_2. In the first process class, the SiO_2 surface is modified by conversion to ammonium fluorosilicate ($(NH_4)_2SiF_6$) using a combination of NH_3 and fluorination agent, such as CF_4 plasma [185], NF_3 plasma [185], HF vapor [186, 187], H_2/NF_3 plasma [188, 189], or H_2/SF_6 plasma [186]. This step is followed by desorption via heating using either halogen lamps [185], infrared lamps [186, 187], or a vacuum break and a hot plate [188, 189]. This approach yields etch rates in the range of 10 – 100 Å/cycle. We show a schematic representation of this process in Fig. 3.2a.

The second class of processes uses a "conversion etch" [98] whereby SiO_2 is modified by conversion to alumina and aluminosilicates using trimethylaluminum (TMA) exposures, followed by fluorination induced by HF vapor [190, 191] or CHF_3 [191], which forms fluorinated alumina and aluminosilicate compounds. Another TMA exposure causes transmetalation and volatilization of the modified surface, while

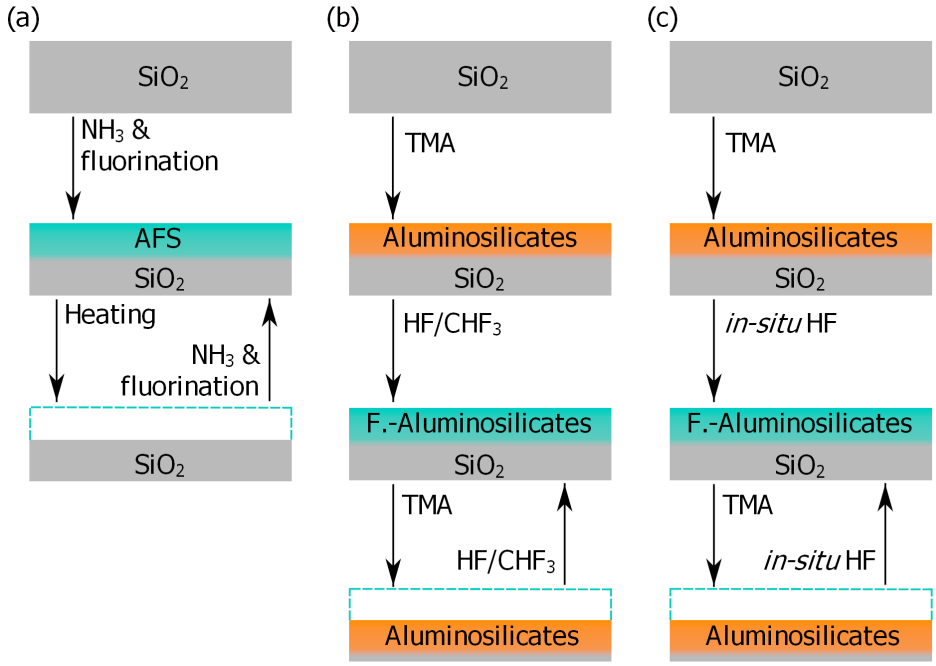

Figure 3.2: SiO_2 ALE process cycle using the process(es) found in: (a) Refs. [185–187, 192]. AFS is an abbreviation of ammonium fluorosilicates. (b) Refs. [190, 191, 193, 194]. F.-Aluminosilicates stands for fluorinated aluminosilicates. (c) This work.

simultaneously forming more alumina and aluminosilicates. This approach yields etch rates of $\sim 0.31 - 0.35$ Å/cycle. We show an example of this process class in Fig. 3.2b.

Each method has practical complications when applied to device fabrication. These issues include the lack of atomic scale control (etch rates are > 5 Å/cycle) [185–189]; long cycle times (from 155 s to over 10 min); inconsistent etch rates [191]; the use of HF vapor [186, 187, 190, 191], which cannot be used in some commercial ALD systems; high pressures (> 250 mTorr) [190, 191], which is outside the process range for some commercial ALD systems; the use of lamp heating [185–187], which requires special system designs and increases cycle time; or breaking vacuum [188, 189]. Additionally, the only measurements of surface roughness show either no effect [189] or an increase after ALE [188]. Therefore, a new process that is compatible with commercial tools is needed to facilitate the practical application of SiO_2 ALE to device fabrication.

Here, we report an ALE process for SiO_2 using sequential exposures of TMA and an $Ar/H_2/SF_6$ plasma. This process falls into the second process class discussed,

and we show it in Fig. 3.2c for comparison. We demonstrate that a sufficient hydrogen content in an Ar/SF_6 plasma reduces the spontaneous etch of SiO_2 to negligible levels while sufficiently modifying the surface for ALE. We observe an etch-per-cycle (EPC) at 400 °C of up to 0.58 Å on thermally oxidized SiO_2, and up to 2.38 Å on sputtered SiO_2. This process exhibits perfect synergy and self-limiting characteristics. We performed surface roughness measurements after ALE and observed a 62% decrease in the roughness of an RIE-roughened surface. Furthermore, XPS reveals less than 2% combined F and Al contamination post-ALE, nearly an order of magnitude less than other reports. Our work paves the way for SiO_2 ALE in device fabrication pipelines using widely available processing tools. For SiO_2 optical devices in particular, this may potentially lead to on-chip photonic devices limited only by intrinsic dissipation.

Overview of characterization techniques

There are three film characterization techniques which will be used both within this work and the work in chapter 4. These deserve some description for the benefit of unfamiliar readers. We give a brief definition for each, providing information on their advantages and disadvantages, and discuss why they are of interest here.

Ellipsometry is a non-destructive method by which a film (or stack of films) are analyzed through their interaction with light. In its most basic form, an ellipsometer reflects a beam of monochromatic light off the surface of interest and measures the change in the polarization state [95, 195]. In most modern ellipsometers the light source is composed of multiple distinct-wavelength sources or a broad spectrum source, allowing for a spectroscopic analysis which yields additional information about the surface being analyzed. Additional data can be obtained by taking multiple measurements at different angles to the surface. A model is then constructed with some number of adjustable parameters and fit to the collected data. Depending on the model and how much data can be taken, values such as the optical coefficients or film thickness may be extracted [95]. This technique can be performed both *in-situ* or *ex-situ* and measurements typically only take a few seconds, making it a versatile technique for the rapid collection of film data. The largest drawback is that films which are too absorbing cannot be analyzed, and the values extracted through the model fit are only as good as the model. Having too many free parameters or unknowns (such as the optical coefficients of the film) can result in incorrect thickness values. The films in this thesis, however, are well characterized and thus the ellipsometric models are ideal for measuring their thickness.

Atomic force microscopy (AFM) is also a non-destructive (typically) *ex-situ* technique which focuses on the morphology (or other characteristics) of surfaces. An atomic force microscope is fitted with a small mm-scale cantilever, at the end of which is a needle-like tip that is sharpened to the single-nanometer scale. In the typical "tapping" mode, this tip is scanned across the surface of interest via piezoelectric actuators, briefly lowering to touch the surface and then raising again. Its position is monitored through a laser which is reflected off the backside of the cantilever. By monitoring the position of the tip each time it contacts the surface, a 3D map of the surface is constructed. This method can be used for a number of purposes, including the measurement of devices too small to be accurately imaged via other techniques, nanoparticle analysis, and roughness characterization [196]. Specialized types of AFM can measure other quantities such as resistivity and magnetization [95]. Here, we use it to measure surface roughness of etched and deposited materials.

X-ray photoelectron spectroscopy (XPS) is a non-destructive *in-situ* or *ex-situ* technique which is capable of determining the elemental composition of the surface of a film [197]. While other techniques exist to perform similar analyses, such as secondary ion mass spectrometry (which are also far more sensitive and capable of detecting elements such as H and He), facilities to conduct these measurements are not as readily available. In an XPS tool, a metal target is bombarded with electrons causing energy transitions which emit x-rays. These rays are cleaned to a single wavelength and focused onto the surface of interest. There, the rays have sufficient energy to remove electrons from the atoms in the surface. By measuring the kinetic energy of these electrons compared to the energy of the incident x-rays, the binding energy of the electrons is calculated. Each element has a unique fingerprint in terms of the electron binding energies in each electron shell, allowing for the determination of the elemental species in the surface. Furthermore, the technique is sensitive enough that minor changes in binding energy corresponding to specific bonds (for instance, Ni-Ni vs Ni-O) are detectable, which is useful for identifying the specific compounds in the sample surface. Although x-rays penetrate quite far into the sample, the electrons which are emitted only escape from the uppermost $\sim$ 10 nm of material, making it a surface-sensitive technique. While XPS itself is non-destructive, it may also be coupled with destructive ion milling to evaluate the composition of a sample as a function of depth. Here, an XPS scan is initiated after some amount of surface material is removed by an ion beam. This is typically called depth-profiling XPS. Depth profiling can also be performed in a non-destructive manner using specialized tools which take measurements of the emitted electrons

at multiple angles. By using the differences in spectra and the fact that electrons emitting from deeper in the material will be less likely to be picked up at angles far from sample normal, a profile of the top ~ 10 nm can be reconstructed. We use both surface and depth-profiling XPS to measure contamination from etch and deposition processes.

These three techniques cover the essential thin film characterization needs in this work. ellipsometry is a very useful technique for the measurement of etch and deposition rates since the measurement of film thickness before and after processing are straightforward without having to perform any patterning or post-processing to create features measurable via other techniques like AFM. Furthermore, measurements can be taken at multiple points on the film, reducing uncertainty. AFM is useful for quantifying surface roughness, which is of interest as ALE is known to cause smoothing. Furthermore, in chapter 4, understanding the surface morphology of fabricated films reveals the mode of film growth and is critical for creating good devices (typically, smoother is better). Finally, because ALE is a chemical process, the possibility of contamination is present. XPS is useful to quantify the degree to which the chemicals used remain on the surface after treatment, and to what depth. In chapter 4 it is useful for a similar reason, except to measure contaminants coming from non-process sources (e.g. oxygen or water outgassing from the chamber walls or the deposition source).

3.2 Experimental details

All ALE processes were conducted in an Oxford FlexAL II system unless otherwise stated. The process chamber was preconditioned by an $Ar/O_2/SF_6$ plasma clean (120 sccm Ar, 40 sccm O_2, 40 sccm SF_6) for 6 minutes to remove contaminants with volatile fluorides. This cleaning was followed by 300 cycles of Al_2O_3 ALD per four hours of ALE to coat the chamber in a material with a nonvolatile fluoride. Next, the ICP and chamber were conditioned to the ALE plasma by running a 2 minute $Ar/H_2/SF_6$ plasma (150 sccm Ar, 42 sccm H_2, 8 sccm SF_6). Lastly, 10 cycles of ALE were performed with an oxidized silicon carrier wafer in the chamber. Samples were then inserted into the reactor for processing. Except where otherwise specified, the table temperature was 400 °C, and plasma steps were operated with an ICP power of 100 W at a pressure of 100 mTorr.

Our ALE process is motivated by ALE processes for SiO_2 based on HF and TMA exposures. However, HF vapor is both hazardous and incompatible with commercial

ALD tools including the Oxford FlexAL. To address these issues, one recent work utilized fluorine radicals produced from a plasma containing SF_6 or NF_3 [176]. However, fluorine radicals readily etch SiO_2. Instead, we employed an $Ar/H_2/SF_6$ plasma to supply the necessary HF chemistry. The inclusion of H_2 in the plasma mixture results in the scavenging of fluorine radicals to form vibrationally excited HF *in situ* [198–203]. The resulting HF(v) functions in the etching process similarly to HF delivered from a vapor source while posing far less of a safety hazard and engineering problem. Despite having been known for some time owing to chemical laser research [198–200], this reaction has only recently been employed for both dry etching [201–203] and ALE [107, 108, 186, 188, 189].

The ALE process was performed using the following sequence of steps. First, all valves were closed except the automatic pressure control valve (APC), the chamber was pumped down for 5 s, the APC valve was closed, and an initial TMA pulse of 610 ms was used to bring the chamber to $\sim 200 \pm 10$ mTorr. After 390 ms, another 10 ms TMA pulse was admitted to maintain the TMA pressure in the chamber, and this boosting pulse was repeated every 2 seconds thereafter until the total TMA dose time was 51 seconds. This dose and hold process was chosen because of the 250 mTorr maximum system pressure and to minimize usage of the precursor. The TMA dose was followed by a 2 s purge step with Ar. The TMA purge was followed by a plasma exposure of 42 sccm H_2, 8 sccm SF_6, and 150 sccm Ar (gases stabilized for 3 seconds before striking). The plasma dose time was 15 s. The $Ar/H_2/SF_6$ plasma mixture is hereafter referred to as "*in-situ* HF". The plasma exposure was followed by another 2 s purge to end the cycle. No change in etch rates was observed for purge times ranging from 2-10 s, and 2 s was chosen to minimize the cycle time. The overall process was terminated with a final TMA step.

Except where specified, SiO_2 thin film samples used for ALE experiments were prepared by dry-oxidizing high-resistivity (> 20 kΩcm) prime-grade (100) silicon wafer (University Wafer) to a measured oxide thickness of $70-80$ nm. Film thickness was measured via *ex-situ* ellipsometry using a J.A. Woolam M-2000 spectroscopic ellipsometer. Measurements were taken in a 3×3 grid across the center 10×10 mm of a 13×13 mm sample. Each measurement was taken using a wavelength sweep between $370-1000$ nm, at 60°, 65°, and 70°, and using a dwell time of 2 s. No focusing probes were used, resulting in a beam diameter of ≈ 3 mm. The thickness of SiO_2 was determined using a fit to a film stack consisting of Si wafer, Si/SiO_2 interface, and thermal SiO_2 film, with all model data from Ref. [204]. Samples were

oriented in the same position for each scan, and the uncertainty is taken as the sum of the fit error as reported by the ellipsometer and two standard deviations of the distribution of etch depths measured across the nine points.

Surface mapping was conducted using a Bruker Dimension Icon atomic force microscope (AFM) in PeakForce Tapping mode using a ScanAsyst-Air AFM probe. Two types of scans were taken: 500×500 nm with a scan rate of 0.5 Hz and 256 samples per line, and 1000×20 nm with a scan rate of 0.1 Hz and 1024 samples per line. Post-processing was performed on the 500×500 nm scans via the Bruker Analysis flatten operation at first order, and the roughness parameters R_q and R_a (defined as the root mean square and average deviations, respectively) were then taken from the resulting surface map. The other scans were used for a surface noise analysis described in Sec. 3.3.

XPS was performed using a Kratos Axis Ultra X-ray photoelectron spectrometer and monochromatic Al Kα source. XPS data was analyzed using CASA-XPS (Casa Software Ltd.) with a U 2 Tougaard background. RSF values were taken from the internal CASA library for Kratos tools.

3.3 Results

Native surface etching and wall effect

We first discuss the etching of the surface material on an SiO_2 film. In non-oxide materials, it is expected that the uppermost section of the surface, ranging from a few angstrom to a few nanometers, will oxidize upon exposure to atmosphere and form a native oxide. This layer will then etch differently than the bulk material and is a factor that has to be accounted for without *in-situ* thickness monitoring. Although SiO_2 is, of course, already an oxide, it was discovered that the top few angstroms etch more readily than the bulk material. This effect is shown in Fig. 3.3a, in which we show the etch depth for the same process ran three consecutive times on a single SiO_2 film sample. In the first etch run, the rate was 1.1 Å /cycle. In the two subsequent runs, the rate was 0.6 Å /cycle. This effect was observed for every sample used and is an important factor to consider in experimental design. To this end, most samples were pre-treated with ALE before they were used for an experiment.

Another critical discovery was the importance of proper preconditioning for this process. In some ALE works, the condition of the chamber walls has been a notable contributor to the etch process [175, 205, 206]. Because the tool used was in a shared

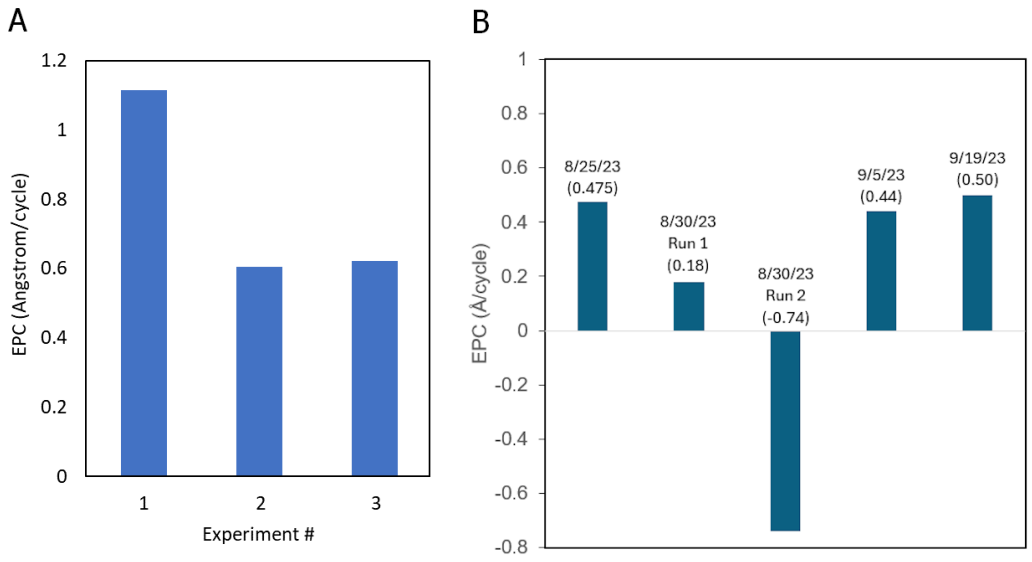

Figure 3.3: (A) Etch rates measured on the same sample using the same ALE recipe for consecutive processes. The initial surface etches much faster than the bulk, resulting in an increased etch rate for the first process. Afterwards, the etch rate stabilizes. (B) Etch rates for the same ALE process measured on different dates using various preconditioning processes.

facility, the chemical condition of the chamber walls would vary as other users ran ALD processes including but not limited to Al_2O_3, SiO_2, HfO_2, and NbN. We show the effect of the chamber condition and preconditioning process in Fig. 3.3b. On 8/25/23, preconditioning consisted only of alumina ALD. At this time this was sufficient to neutralize any HfO_2 coatings on the chamber walls, which was found to be deleterious to the ALE process. On 8/30/23, preconditioning included alumina ALD, plasma stabilization, and ten cycles of ALE. However, the tool had been used recently for NbN deposition, and this preconditioning process was insufficient to remove or bury the coating on the chamber walls. Evidently, NbN is sufficiently reactive with one or both ALE steps that it would form volatile compounds and redeposit on the SiO_2 film in sufficient quantities that Nb could be detected via XPS. Although the first ALE process ran after preconditioning still showed a positive but reduced etch rate, the next run showed a significant amount of deposition. On 9/5/23, an O_2/SF_6 plasma was incorporated to help remove NbN films, but the recipe did not have the plasma stabilization or ALE steps and still showed a reduced EPC. On 9/19/23, the recipe was finalized as detailed in Sec. 3.2, and the observed etch rate was within the expected range.

It should be noted that under ideal conditions, the ICP discharge color of the *in-situ*

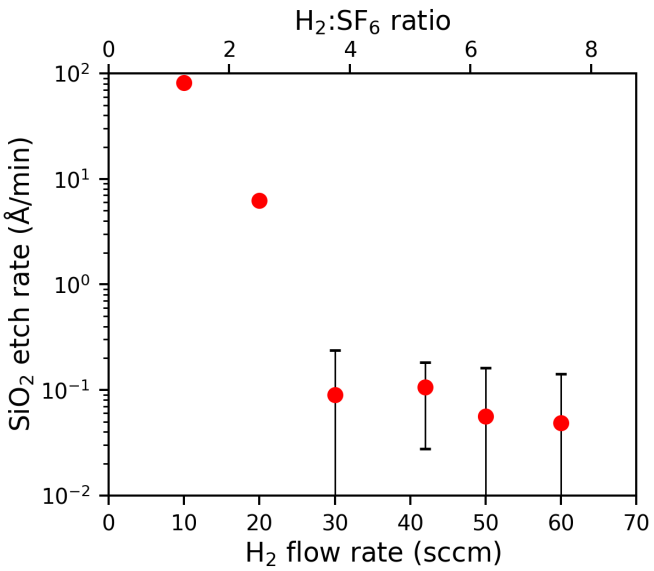

Figure 3.4: Spontaneous etch rate of SiO_2 when exposed to an $Ar/H_2/SF_6$ plasma versus H_2 flow rate. Ar and SF_6 flow rates were held constant at 150 and 8 sccm, respectively. At 30 sccm H_2 and above spontaneous etching of SiO_2 is practically eliminated. The point at 42 sccm H_2 is referred to throughout this work as "*in-situ* HF".

HF is brilliant red, but when the etch chemistry is altered by Nb compounds the discharge was pink, more akin to the typical argon plasma. While techniques such as optical emission spectroscopy were unavailable, this color change could indicate that wall contamination results in the disruption of the HF-forming plasma reactions. Even with a compatible chamber condition (such as an alumina coating), this color shift is also present at the beginning of processing and is the reason for running the 2 minute $Ar/H_2/SF_6$ plasma and 10 cycles of ALE during preconditioning. These steps allow the plasma chemistry to equilibrate with the wall coating, stabilizing into its visually red state.

SF_6:H_2 flow rate ratio and SiO_2 spontaneous etching

We next characterize the spontaneous etch rate of SiO_2 versus the hydrogen flow rate into an Ar/SF_6 plasma, to determine the H_2 flow rate which eliminates spontaneous etching and thereby facilitates ALE. An $Ar/H_2/SF_6$ plasma has been used for ALE of SiO_2 previously, but the effect of the plasma exposure half-cycle was not reported [186]. The spontaneous etch rate of SiO_2 in Ar/SF_6 was measured by exposing SiO_2 samples to plasmas with varying H_2 flow rate. The Ar and SF_6 flow rates were 150 and 8 sccm, respectively. For these experiments, samples were pre-treated by a 2 min 150 sccm Ar, 35 sccm H_2, 15 sccm SF_6 plasma, followed by a 1 min 150 sccm

Ar, 42 sccm H_2, 8 sccm SF_6 plasma to begin etching into the bulk and clean the surface.

The measured etch rate versus H_2 flow rate is shown in Fig. 3.4. The data indicate that for H_2 flow rates at or exceeding 30 sccm, corresponding to an H_2:SF_6 flow rate ratio ≥ 4, the etch rate is negligible. This result is compatible with the findings of Refs. [201, 202], which hypothesized that the addition of a sufficient quantity of H_2 in an Ar/SF_6 plasma yields vibrationally-excited HF, which does not spontaneously etch SiO_2. Recent ALE works using a similar chemistry also found a similar ratio prevented spontaneous etching of TiN [107] and NbN [108]. The HF formed *in situ* can then be used for ALE.

Synergistic etching and saturation curves

We next show the thickness change of SiO_2 after repetitions of each half cycle (TMA and *in-situ* HF) as well as the full ALE process in Fig. 3.5. Because samples were not preconditioned, the first 20 cycles are omitted from the analysis to account for the initial surface etching issue described previously. First, with only TMA half cycle exposures, we observe an increase in film thickness of ≈ 0.09 Å /cycle. This increase could be attributed to the formation of alumina and aluminosilicates due to TMA reacting with SiO_2, and adsorbed aluminum species oxidizing during ex-situ ellipsometry. With only *in-situ* HF exposures, we observe a negligible change in the film thickness. With both half cycles, we observe a linear ($R^2 = 0.99997$) decrease in the film thickness with an etch rate of 0.53 Å /cycle. Because neither half cycle results in etching, the recipe exhibits perfect synergy.

To ensure that each ALE half cycle is self-limiting, we measured the EPC versus dose time and show the data in Fig. 3.6. When the TMA exposure time is varied independent of the *in-situ* HF time (constant at 15 s), saturation occurs after $\sim$ 80 s as shown in Fig. 3.6a. When the *in-situ* HF exposure time is varied while the TMA time is kept constant (51 s), saturation is observed after $\sim$ 8 s. In this latter case, we also find deposition occurs when the dose time is zero, possibly due to the formation of alumina and aluminosilicates. The fully saturated etch rate was found to be $\sim$ 0.58 Å per cycle.

EPC variation with temperature and pressure

Next, we present the dependence of EPC on table temperature in Fig. 3.7a. Temperature was measured by a thermocouple integrated into the sample stage. Samples were preconditioned with 10 cycles of ALE $\sim$ 24 hours prior to usage. We observe

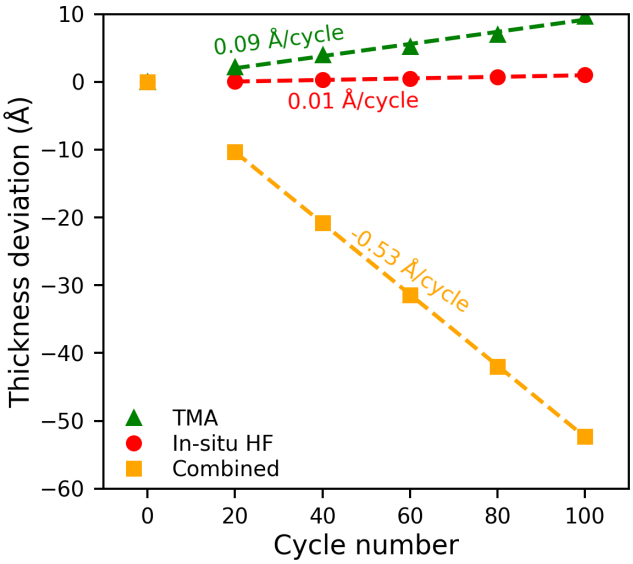

Figure 3.5: Thickness change versus cycle number using only *in-situ* HF (red circles), only TMA (green triangles), and both half-cycles together (gold squares) measured using ex-situ ellipsometry. Dashed lines of the same color are linear fits to the points from 20 – 100 cycles. The per-cycle thickness changes for TMA only, *in-situ* HF only, and both half-cycles are 0.09, 0.01, and -0.53 Å /cycle, respectively. This indicates perfect synergy; while neither half step results in etching, taken together etching is achieved.

that at 150 °C deposition occurs, possibly due to the formation of AlF_3 as was reported in a previous ALE study of alumina [176]. At ≥200 °C etching occurs, and the EPC increases approximately linearly with increasing temperature.

We additionally show the dependence of EPC on TMA pressure in Fig. 3.7b. In these experiments the TMA dose time was fixed at 51 s and the temperature at 400 °C. The TMA pressure was varied by decreasing the TMA dose time below 610 ms such that the pulse brought the chamber to the desired pressure. Some variation in the chamber pressure during the TMA hold was observed; this uncertainty is indicated in Fig. 3.7b as a horizontal error bar. The effect of a shorter initial dose time versus that of a lower pressure could not be distinguished. We observe a linear trend between 50 and 200 mTorr. We note that it is expected that the etch rate decreases to zero at zero pressure to be consistent with the findings in Figs. 3.5 and 3.6. The EPC does not plateau for pressures up to 200 mTorr, which suggests that reactors capable of higher pressures could achieve either faster EPC saturation or a larger EPC above 200 mTorr. We were unable to test higher pressures due to the maximum system pressure of 250 mTorr. These findings differ from prior HF/TMA

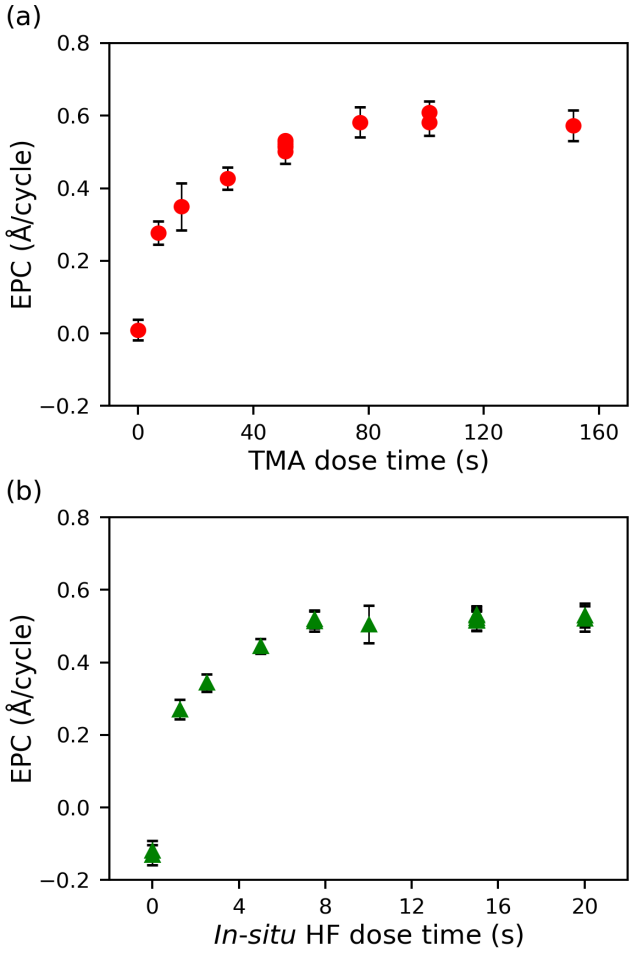

Figure 3.6: (a) Etch per cycle versus TMA dose time with *in-situ* HF exposure time fixed at 15 s. Self-limiting behavior is observed with the etch rate saturating after 80 s of exposure. (b) Etch per cycle versus *in-situ* HF dose time when the TMA dose was fixed at 51 s. This step is also self-limiting with etch rate saturating after 8 s.

SiO_2 ALE works as we observe significant etching (> 0.2 Å/cycle) at pressures below 800 mTorr [190, 191].

Post-ALE surface composition

We used surface XPS to characterize the composition of three different samples: untreated SiO_2, ALE treated SiO_2 (300 cycles of "rapid" ALE described below), and ALE treated SiO_2 with a post-process O_2 plasma (5 min, 60 sccm O_2, 400 °C, 15 mTorr, 400 W ICP power). The post-processing step on the last sample was done in an effort to replace surface fluorine species with oxides, decreasing F surface contamination. The XPS spectra are shown in Fig. 3.8 and film compositions are tabulated in Table 3.1. Spectra for the oxygen plasma-treated sample are qualitatively

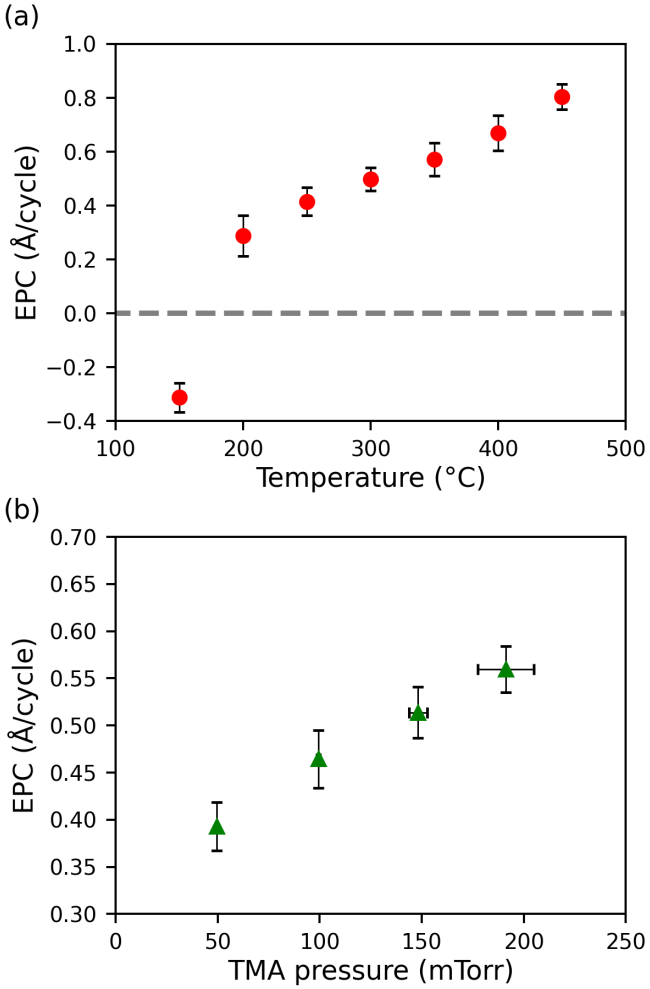

Figure 3.7: (a) Etch per cycle versus table temperature. At 150 °C deposition was observed, while at 200 °C and higher etching was observed. Etch rates are larger than reported in other figures due to ∼ 24 hours of sample exposure to atmosphere between preconditioning and the experiment. (b) Etch per cycle versus TMA pressure. Horizontal error represents the two-sigma deviation from the mean pressure during the experiment.

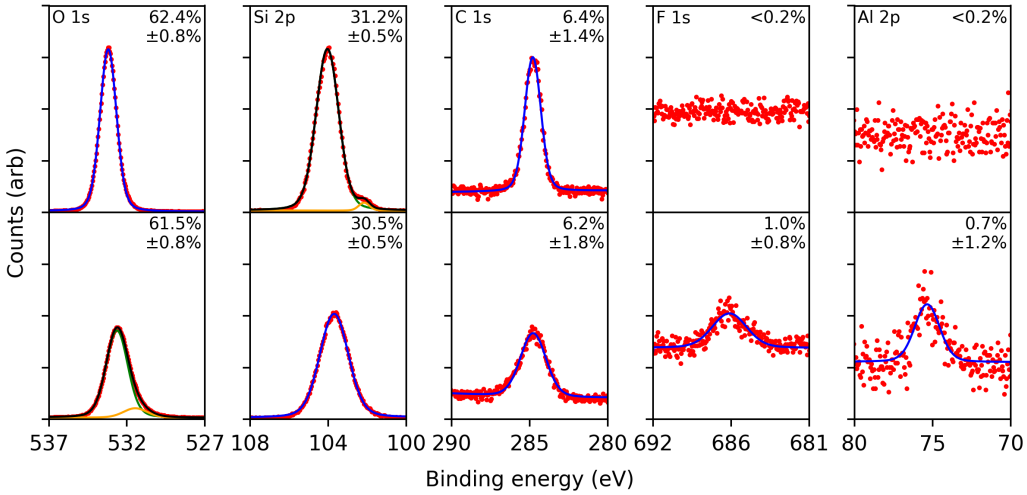

Figure 3.8: Surface XPS data for an untreated (upper plots) and ALE treated (lower plots) SiO_2 film. From left to right, peaks correspond to O 1s, Si 2p, C 1s, F 1s, and Al 2p. Sulfur not shown as it was not detected. Experimental data shown as red points, and blue lines represent the peak fit for single peaks. Where two sub-peaks are present they are shown as green and yellow lines, with a black envelope.

similar to those of the ALE-treated sample and are therefore not shown. For the untreated film, oxygen and silicon are detected at 2:1 as expected for SiO_2. Some carbon from adventitious sources is detected. Neither fluorine nor aluminum are present above the detection limit ($\approx 0.2\%$), and sulfur is not shown in any plots as it was not found in any sample. Note that the silicon peak consists of two subpeaks; the larger peak at ~104 eV corresponds to SiO_2, while the smaller peak at 102 eV could be attributed to surface contamination from either silicon (oxy)nitride or organic bonds formed at the end of thermal oxidation [207].

After ALE, the O:Si ratio is unchanged at 2:1, and the overall quantity of these elements decreases by 1.6%. The carbon concentration in the ALE-treated film is the same as in the untreated film to within uncertainty. Fluorine and aluminum are found to compose less than 2% of the sample surface. The Si sub-peak is not observed, consistent with it originating from a surface contaminant. An oxygen sub-peak appears at 531.5 eV, comprising 11% of the total peak area, which we assign to aluminum species [207].

After oxygen plasma post-treatment, the surface is found to contain decreased concentrations of carbon and fluorine, with the fluorine concentration decreasing from $1.0 \pm 0.8\%$ to $0.4 \pm 0.5\%$. No other contaminants were observed. To determine whether this difference is statistically significant, we performed a T-test, which takes

Sample	O (%)	Si (%)	C (%)	F (%)	Al (%)
Untreated	62.4±0.8	31.2±0.5	6.4 ± 1.4	< 0.2	< 0.2
ALE	61.5±0.8	30.5±0.5	6.2 ± 1.8	1.0 ± 0.8	0.7 ± 1.2
ALE and O_2 plasma	62.6±0.7	30.8±0.6	5.3 ± 1.7	0.40±0.5	0.96±1.1

Table 3.1: XPS surface composition of untreated SiO_2, ALE treated, and ALE treated with a post-process oxygen plasma step. Values derived from plots as shown in Fig. 3.8. The estimated detection limit is 0.2%.

as input two sets of evaluations of a single variable and outputs the probability that there is no statistically significant difference (null hypothesis). We used as input the peak areas from the 200 CasaXPS Monte Carlo data simulations from which the original compositional uncertainties were derived. We find that the probability of the null hypothesis is $< 10^{-4}$, indicating that the observed compositional change is statistically significant despite the overlap in uncertainties. The oxygen sub-peak is still present in the same location at 13% of the area after plasma treatment.

Considering these observations, we find that the oxygen treatment is effective at decreasing the amount of fluorine while leaving the remainder of the film composition unchanged. Similar ALE works using TMA and HF have reported approximately 8.5% F [191] and 4% Al (Refs. [190, 191]) after etching. After oxygen plasma treatment, our process results in 89% less F and Al contamination compared to the other works.

EPC dependence on SiO_2 preparation method

We measured the EPC on four samples prepared by different methods. It has previously been established that oxides generally exhibit different etch rates during ALE depending on their crystallinity [208, 209], and although SiO_2 is typically used in amorphous form, different preparation methods may produce different amorphous structures, compositions, and density. Our first sample was thermally oxidized as described in Sec. 3.2 although with water vapor instead of oxygen. The second sample was made using ALD with BDEAS and O_2 plasma at 200 °C on the Oxford FlexAL. The third sample was made using PECVD with silane and N_2O at 200 °C in an Oxford Instruments Plasma Technology Plasmalab System 100. The fourth sample was fabricated via sputtering at ambient temperature using an SiO_2 target on an AJA Orion ATC 1800 system. The samples were pretreated with 20 cycles of ALE before measurements.

The EPC for each of our four films is shown in Fig. 3.9. We observe that thermally

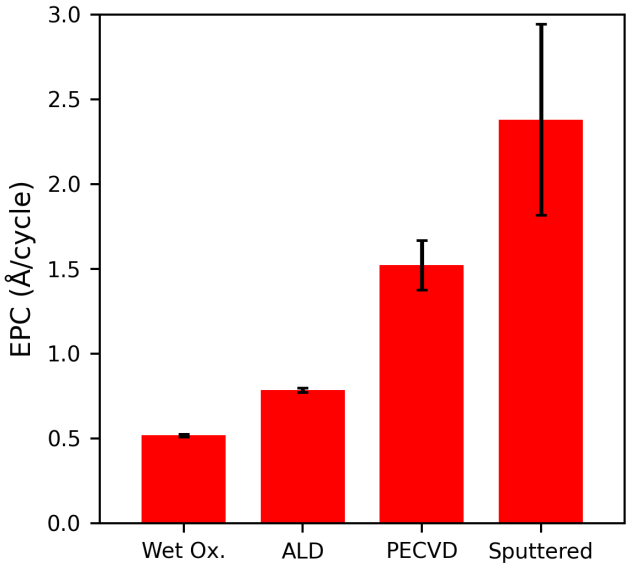

Figure 3.9: ALE etch per cycle for SiO_2 films prepared by different methods: wet oxidized (0.52 Å/cycle), ALD (0.78 Å/cycle), PECVD (1.5 Å/cycle), and sputtering (2.4 Å/cycle).

wet-oxidized SiO_2 etches the slowest at 0.52 ± 0.01 Å/cycle, the same rate for dry-oxidized films. ALD SiO_2 has a comparable etch rate of 0.78 ± 0.01 Å/cycle. PECVD SiO_2 exhibits a larger etch rate of 1.52 ± 0.15 Å/cycle, and sputtered SiO_2 has the largest etch rate of 2.38 ± 0.56 Å/cycle.

A possible explanation for the observed trend is that ALE etch rates are inversely correlated to film density (with lower density films having higher atomic diffusion coefficients), which is in turn affected by the film preparation method. It is known that PECVD [210] and sputtered [211] SiO_2 densities vary based on process conditions and may be less than those of ALD [212] and thermal films. Because thin-film density is difficult to determine directly, we measured the index of refraction (n) of our samples as an indirect measure of density [213, 212], assuming that n is a function of density only. However, no correlation between n and the etch rate was found. Therefore, we are unable to draw a conclusion as to the cause of the varying etch rates. In addition to density, the films may also differ in composition through impurity content (hydrogen [210, 212] or other decomposition byproducts of silane and BDEAS), the amorphous structure formed by each preparation process, and roughness, all of which could affect the etch rate. Due to the difficulty in fabricating samples with systematically varied properties, we are unable to draw conclusions as to which factors are influencing the etch rate of each sample.

Surface roughness

We finally examine the change in surface roughness induced by ALE. Most of the SiO_2 samples previously fabricated had a surface roughness of approximately 0.3 nm or less. We applied the process to these samples but did not detect any roughness change within the AFM resolution of 0.2 nm. Therefore, it was necessary to fabricate a rougher starting surface to observe any changes in roughness. We fabricated these rough SiO_2 films by Si wet-oxidization to a thickness of 227 ± 1.2 nm followed by reactive ion etching (a 315 second plasma exposure using 40 sccm SF_6 and 150 sccm Ar at 50 W RF table bias) to a thickness of 30.6 ± 3.9 nm. The AFM scan of this roughened film is given in Fig. 3.10a. The surface is an order of magnitude rougher than a pristine SiO_2 surface (R_q = 3.49 nm versus $R_q \lesssim 0.30$ nm).

The roughened sample was then treated with 300 cycles of a version of the ALE recipe optimized to minimize the overall process time, which we refer to as "rapid" ALE. This process had the following parameters: 450 °C table temperature, 8 s of *in-situ* HF, 15 s of TMA, 750 ms purge times, 2 s pump and gas stabilization times, and 0.5 s for the APC valve to close before TMA dosing. The ICP was left open to minimize particulates generated by the gate valve. This rapid version of the ALE process has a total cycle time of 29 seconds. After 300 cycles, the SiO_2 thickness was 18.2 ± 3.7 nm, corresponding to an etch depth of 12.4 ± 0.3 nm and EPC of 0.41 ± 0.01 Å/cycle. The post-ALE AFM scan is shown in Fig. 3.10b. The surface is visibly smoother, with a 62% decrease in roughness to R_q = 1.33 nm. Therefore, the isotropic ALE of SiO_2 using the recipe reported here was found to exhibit a surface smoothing effect. We note that this smoothing effect is expected to depend on the initial surface topology, a topic which will investigated in a future study. The post-treatment oxygen plasma was not found to roughen the surface, indicating that it can be used additionally to reduce surface contamination.

To be applied to optical devices, it must also be determined whether the smoothing effect occurs for feature sizes relevant to optical scattering. In SiO_2 resonators, the relevant optical wavelengths are generally much larger than the characteristic dimensions of surface features, resulting in a $\sigma^{-2}B^{-1}$ dependence of the roughness-limited Q (Ref. [214]), where σ is the root mean square roughness of surface and B is the correlation length of surface features. Therefore, scattering is not only related to the height and quantity of surface features, but also their width, where long period features scatter more strongly than short period ones.

To determine the degree of smoothing across various feature widths, we calculated

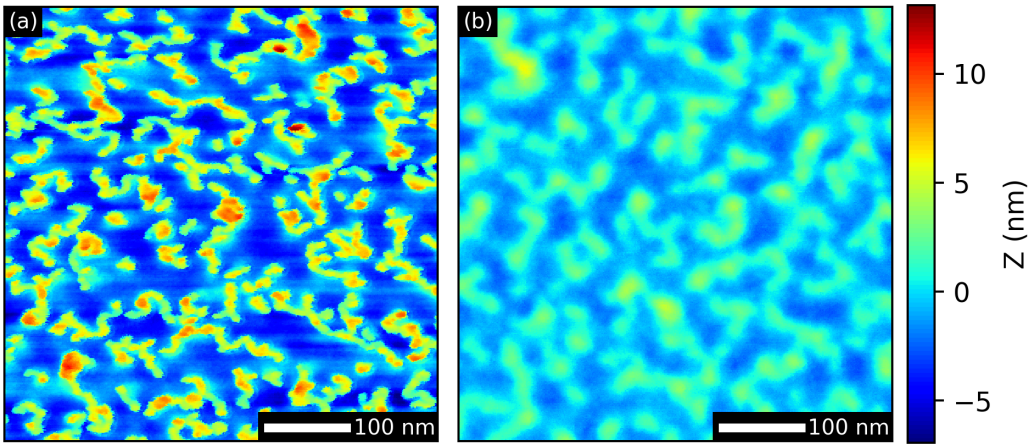

Figure 3.10: (a) Surface topography of SiO_2 roughened via rapid SF_6 etching, with R_q = 3.49 nm, R_a = 2.95 nm. (b) After treatment with 300 cycles of ALE, corresponding to an etch depth of 12.4 ± 0.3 nm. The roughness has decreased, with R_q = 1.33 nm, R_a = 1.08 nm.

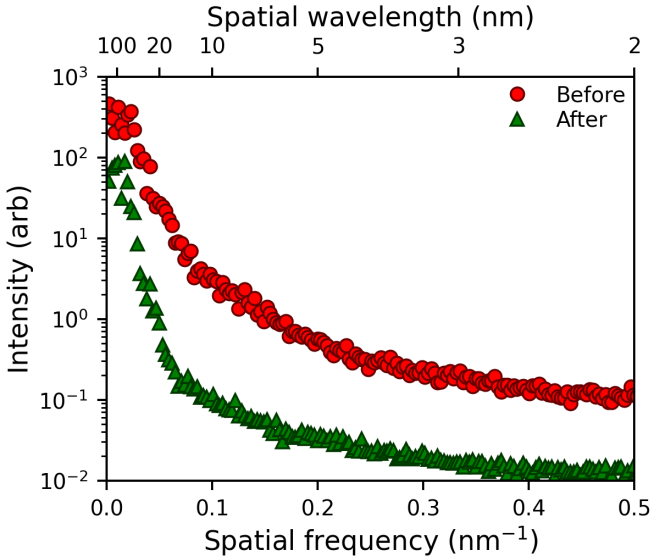

Figure 3.11: Power spectral density of surface roughness versus spatial frequency and wavelength for roughened SiO_2 surface (red circles) and after 300 cycles of ALE (green triangles).

the surface power spectral density (PSD) of the roughened SiO_2 sample before and after etching the roughened sample. The PSD represents the intensity of surface features versus their spatial wavelength (or frequency) and can therefore be used to determine whether ALE smooths features of various sizes. The PSD was calculated by decomposing four 1000×20 nm scans taken across the sample into individual line scans, taking the absolute square of the discrete 1D Fourier transform of these scans (with linear fit subtracted) and averaging the results, which are shown in Fig. 3.11. We observe a decrease in the PSD intensity across all feature sizes present in the scan. This finding indicates that the ALE process should be suitable for smoothing optical device surfaces regardless of the dominant feature size.

3.4 Discussion

In addition to the demonstration of a safer chemistry for SiO_2 ALE, we have also shown that this process can be done on a commercial tool with the ability to treat large wafers. The most obvious next step would be the treatment and characterization of optical devices. However, fabricating these devices to a sufficiently high quality that surface roughness scattering is the dominant loss mechanism is not trivial and outside our expertise. We are currently collaborating with another research group to quantitatively prove the usefulness of ALE smoothing for optical devices.

This work also provides useful information for the deployment of similar recipes for device fabrication:

1. We reaffirm that ALE may be very sensitive to wall conditions. In shared user spaces, measures must be taken to both ensure the process will work and that it will work reproducibly. Prior to the establishment of the preconditioning process described, experiments conducted in the course of this work were generally unreliable on a day-to-day basis. After the final preconditioning recipe was deployed, this process could be repeated a year later, with shared tool use in the meantime, to within 0.01 Å/cycle of the expected EPC.

2. While it is true that ALE may induce less damage than processes such as RIE, it does not leave an entirely pristine surface, as shown in the XPS results. However, process optimizations (such as the ALE chemistry used) can significantly decrease the contamination from the precursors used, sometimes surprisingly. Because the fluorination chemistry in use here is very similar to that in prior works, it was expected that the F content of the remaining surface

would also be similar. However, we observed up to a 92% reduction in F in the post-ALE surface by using a related chemistry. Note, it is still unknown whether the contamination by Al and F would be detrimental, and whether losses induced by these contaminants might outweigh the benefit of surface smoothing.

3. Even for amorphous (or polycrystalline) materials, ALE etch rates might vary significantly. Therefore, calibration of published ALE recipes would be wise when applying them to materials fabricated using different parameters than those used in the original study.

We also note that while this process successfully uses SF_6 and H_2 instead of the more immediately-hazardous HF vapor, SF_6 is known to be a very potent greenhouse gas. While the plasma products may differ in composition, it is unknown what the product gases of this process are. Furthermore, environmental legislation has sought to limit the use of gases like SF_6. A variety of relatively safe alternatives with lower global warming potentials do exist, such as NF_3 and hydrofluorocarbons such as CHF_3. Because some similar ALE works also use SF_6-containing plasmas [101, 107, 108, 176, 215], future work could investigate the use of alternative gases to reduce the potential environmental effects of this and similar processes.

3.5 Summary

In summary, we have reported an isotropic SiO_2 ALE recipe compatible with commercial ALD tools based on sequential exposures of $Ar/H_2/SF_6$ plasma and TMA. The process improves upon prior processes by achieving EPC above 0.5 Å/cycle while simultaneously eliminating the need for vapor HF and exhibiting a short cycle time (under 2 minutes) with low TMA pressure requirements (under 250 mTorr). We observe that each process step exhibits saturation and the overall process has perfect synergy. We also examine the etch rate dependence on the preparation method, finding that sputtered SiO_2 exhibits the highest etch rate of 2.38 Å/cycle compared to PECVD, ALD, and thermal SiO_2. Additionally, our process results in 89% less contamination by F and Al than comparable processes. Surface smoothing of a roughened surface is demonstrated. Lastly, because the process is compatible with commercial ALD hardware, performing the process on the wafer scale is limited only by the maximum wafer size of available ALD tools. With the observation of simultaneously low surface contamination and surface smoothing, this work

paves the way for the use of SiO_2 ALE as a post-processing step to improve device performance especially in photonics.

Chapter 4

A THERMAL LASER EVAPORATION SYSTEM ENABLING NOVEL FILM SYNTHESIS

This chapter has been adapted, in part, from

David S. Catherall, Yifei Yan, Finley B. Donachie, Azmain A. Hossain, and Austin J. Minnich. Characterization of ultrathin nickel films deposited by thermal laser evaporation. *Applied Physics Letters*, 128(8):081902, 02 2026. ISSN 0003-6951. doi: 10.1063/5.0309594. URL https://doi.org/10.1063/5.0309594.

D.C. co-designed the research, designed and co-constructed the experimental apparatus, co-ran the experiments, analyzed the data, and wrote the manuscript.

4.1 Introduction

Physical vapor deposition (PVD) of thin films is performed by various well-established techniques, including thermal and electron beam evaporation (E-beam), sputtering, pulsed laser deposition (PLD), and others [216]. Evaporative methods function by heating source material until it vaporizes or sublimates and the vapors subsequently condensing on a substrate. Sputtering and PLD are non-thermal techniques based on the ejection of material from a target by plasma ion impingement and the ablation of a target with energetic laser pulses, respectively. PVD techniques enable directional or conformal deposition of diverse elemental and compound materials.

Film deposition by evaporation is used routinely, for example in the deposition of metals for devices and in epitaxial growth using molecular beam epitaxy (MBE). However, evaporation of refractory elements is a long-standing challenge owing to their low vapor pressure. For instance, elements like W, Ta, and Mo cannot be deposited using effusion cells, and while E-beam evaporation of these elements is technically possible, the deposition rates are usually well below 1 Å/sec (typical E-beam evaporation rates are between 1 and 50 Å/sec). Additionally, careful monitoring and preparation are required to avoid damaging the evaporation system due to the required high powers and temperatures.

These problems can be understood through the equations for the vapor pressure and deposition rate of a material. Under ultra-high vacuum (UHV), the mass flux $\dot{m}$

from a vaporizing material source is given by the Hertz-Knudsen equation [217]:

$$\dot{m} = \sqrt{\frac{m}{2\pi k_B T}} P(T) \tag{4.1}$$

where m is the atomic mass, k_B is the Boltzmann constant, T is the absolute temperature, and $P(T)$ is the vapor pressure of the material. At the temperatures relevant for metal evaporation the factor $\sqrt{T}^{-1}$ is effectively a constant, meaning that the flux is approximately proportional to the vapor pressure. The vapor pressure, then, may be obtained by two different equations. The first and more thermodynamically sound is the Clausius-Clapeyron equation, which in its integrated indefinite form can be written as [218]:

$$\ln P = c - \frac{\Delta h_{vap}}{RT} \tag{4.2}$$

where c is a constant, R is the ideal gas constant and Δh_{vap} is the enthalpy of vaporization. While this equation is not commonly used in practice, the problem with evaporating the refractory metals can be quickly understood; because the relationship is exponential, to achieve any appreciable vapor pressure RT must be comparable to or larger than Δh_{vap}. Across the solids of the periodic table (at standard temperature and pressure), Δh_{vap} ranges from 9.8 kJ/mol (sulfur [219]) to over 800 kJ/mol (tungsten [220]), normalized to 298 K. All of the refractory metals have extraordinarily large enthalpies of vaporization (and fusion), meaning they vaporize (and melt) at equally extraordinary temperatures. This makes metals like tungsten suitable for applications in high temperature applications such as the filaments of incandescent lights. Other elements with particularly high enthalpies of vaporization include Nb, Mo, Ru, Ta, Re, and Os. To evaporate these metals requires very specialized tools so as not to damage the holding apparatus or other system components.

As a note, the assumptions made to derive Eq. (4.2) are not always valid. These assumptions include: (1) The molar volume of the liquid is negligible with respect to that of the vapor (2) The vapor obeys the ideal gas law, and (3) The enthalpy of vaporization is independent of temperature. Because these assumptions induce errors in the actual calculation of vapor pressures, in practice an empirical model known as the Antoine equation is typically used [217, 218]:

$$\ln P = A - \frac{B}{C + T} \tag{4.3}$$

where A, B, and C are fitting parameters. The coefficients are usually found tabulated in various thermodynamic data resources and are valid over a certain

range of temperatures. While only an empirical equation, the Antoine relationship closely resembles Eq. (4.2) and behaves similarly. Regardless, since vapor pressure and evaporation rate are approximately linearly related per Eq. (4.1), it is clear that very high source temperatures are required to create films containing the refractory metals. The necessary question, then, is how to deliver the necessary energy and how to contain it.

To answer these questions, let us consider heat transfer from the deposition target. The heat flux from a material including conduction and radiative transfer (convection will not occur in a vacuum) is given by Fourier's law and the Stefan-Boltzmann law [221]:

$$Q = Q_{cond} + Q_{rad} = -kA_{cond}\frac{dT}{dx} + A_{rad}\epsilon\sigma T^4 \tag{4.4}$$

where Q is the heat flux, k is the thermal conductivity, $\frac{dT}{dx}$ is the thermal gradient across the conductive pathway, ϵ is the emissivity, σ is the Stefan-Boltzmann constant, A_{cond} is the cross-sectional area of conductive heat transfer, and A_{rad} is surface area of the radiating body. This equation indicates that the conductive heat losses scale linearly with temperature differential while radiative losses scale to the fourth power. These scaling factors determine the necessary source geometry for refractory metal deposition. Unfortunately, the only free parameter for both forms of heat loss is the area, as thermal conductivity and emissivity are inherent materials properties. Conductive heat transfer can be nearly eliminated by minimizing contact between the source and other materials: therefore, the preferred geometry is a free-standing source without a large holding structure.

However, at temperatures relevant for refractory metal evaporation, radiative loss will dominate owing to its quartic scaling, making conductive loss less important. Minimization of radiative heat loss requires minimizing the target size; traditional evaporative sources such as MBE and E-beam crucibles are quite large with critical dimensions of multiple inches, with correspondingly large surface areas, and are therefore not well-suited to this task. We can eliminate the crucible entirely, but this requires precise focusing of the energy delivery mechanism to the center of a small slug of material such that the melt pool is contained within the target itself. Since the target is ideally free-standing to minimize conduction, an electron beam cannot be used due to charging, and an ion beam with the necessary power would result in sputtering rather than efficient heating. Therefore, the natural conclusion for a system to deposit refractory metals consists of a small, freestanding slug of source material heated in a small central area by laser.

The use of continuous-wave (CW) lasers to provide the thermal energy necessary to evaporate source material has been previously demonstrated and has the potential to overcome the limitations of other PVD techniques [222–225]. In recent years, this technique has been termed thermal laser evaporation [225–228] (TLE) following earlier works which termed it variations of laser evaporation [223, 229–236]. The technique has also been called thermal laser epitaxy [237–245], which is also abbreviated TLE. In this work, we take TLE to mean thermal laser evaporation as the deposited films here are non-epitaxial.

A schematic of TLE is shown in Fig. 4.1. In this technique, a substrate is placed upside down facing a cylindrical target. A key feature is that the target is freestanding, meaning it is not contained by a crucible, and the only physical contact to the target is at its base. This configuration limits conductive heat transfer and ensures the majority of dissipated energy is radiative. Then, a laser is focused to a small point on the target surface such that the resulting melt pool is completely contained within the target itself owing to the thermal gradient formed by radiative cooling. In this way, for materials with sufficiently high melting points and low thermal conductivity, the target serves as its own crucible.

The laser is focused outside the chamber while a mirror redirects it onto the target. This mirror is critical as, by necessity, the final optical element must have line of sight to the target and will therefore be deposited upon. While the transmittance of a window would be catastrophically decreased by the deposition of a metal film, the reflectivity of a mirror is only slightly altered. While there is a window to direct the beam into vacuum, it does not have a direct line of sight to the deposition source. Lastly, the laser is not entirely absorbed by the target, and therefore a reflected beam is also created during this process, which must be absorbed and the energy dissipated. In the schematic system this is done by the water-cooled chamber walls.

TLE differs from PLD (or laser-MBE) in that heating is performed using CW rather than pulsed lasers, leading to deposition by thermal evaporation rather than an ablation process [246, 247, 223]. This difference has a number of implications: First, the steady state heat load is far greater in TLE, so the hardware must be designed to accommodate high temperatures. Second, the thermal process is more similar to E-beam and MBE, resulting (in theory) in a molecular flux without particulates, which may be created during PLD ablation. Third, because it is a thermal process, unlike PLD, the use of compounds often results in the constituents exhibiting different vapor pressures and therefore the composition of the flux will not

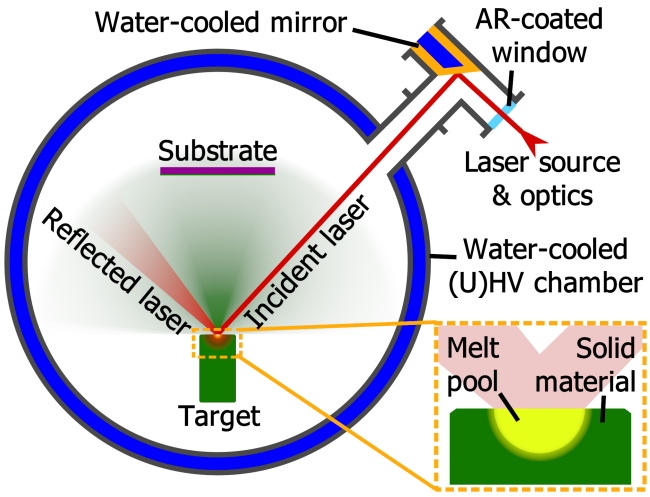

Figure 4.1: Schematic of a TLE system. A laser is focused and passes through a window in a vacuum chamber. The laser is redirected by a mirror and hits the center of an elemental target. The absorbed laser power is sufficient to heat the center of the target to above its melting point such that it slowly evaporates. Above the target is a suspended substrate, upon which vapors condense to form a film. The laser will not be entirely absorbed by the target, and a reflected beam must be intercepted and dissipated, in this case by the water-cooled vacuum chamber walls.

match the composition of the target. Therefore, if compounds are to be deposited, multiple targets are necessary (as is common in MBE). TLE is also well suited for laser-based substrate heating, which can achieve temperatures up to the melting point of the substrate and as such is well suited for high temperature growth and *in-situ* annealing [237, 240–244, 248, 249].

The quasi-stationary nature of deposition by TLE means the deposition process is similar to thermal PVD techniques like e-beam evaporation but with several advantages. TLE requires no crucible for many materials, allowing for the deposition of both refractory metals and elements that may react with a crucible. The lack of a crucible also permits higher source temperatures which would normally damage a crucible or induce contamination, meaning that refractory elements can be deposited at rates typical in PVD systems (0.1 to 1 Å/sec or higher). Because the energy source is located outside of vacuum, the technique is especially suitable for reactive evaporation since there are no hot filaments or resistive heaters that could be degraded by exposure to process gases (e.g. O_2) [224]. Additionally, the source-substrate distance is typically an order of magnitude smaller than in e-beam evaporation or MBE, allowing for higher pressures of reactive background gases without scattering the metallic vapors.

TLE was initially developed contemporaneously with other PVD techniques such as electron-beam evaporation and PLD in the late 1960s. A variety of oxides and compounds were deposited using TLE [222, 223], as well as pure elements including C [231, 250], Os [251], Pt [252], and Te [253]. However, laser technology of the time was inadequate for TLE to compete with other techniques due to two difficulties. First, the most practical CW laser of the time was the CO_2 laser, which was then limited in power to a few hundred watts [253]. Further, its 10.6 µm wavelength is not well absorbed by metals, leading many investigators to focus on oxide or compound targets [223, 254]. Second, the coating of optical elements exposed to the heated target added complexity to the energy delivery system compared to sputtering or electron beam systems [224]. Although this latter drawback could be partially worked around by using mirrors and apertures [224, 233, 253], the other techniques were technically simpler to implement.

Due in large part to the maturation of other PVD techniques, TLE was neglected for decades. Recent developments in laser technology, however, have made the technique increasingly viable. The key development has been the commercial availability of high-power fiber lasers, which emit at micron wavelengths and feature output powers up to and exceeding several kilowatts. Fiber lasers are more useful than the CO_2 laser for evaporating most elements due to the order of magnitude higher absorption of metals at around 1 µm compared to 10.6 µm [254]. Recently, a group at the Max Planck Institute at Stuttgart has developed a modern implementation of TLE using high-power CW fiber lasers and deposited many elements, oxides, and nitrides [225–228, 237–241, 243–245, 249, 255]. However, modern TLE has only been performed by the one group to date, and many of the details of key system components such as the beam delivery system have not been reported. Further, although the deposition of nearly all solid, nonradioactive elements has been reported, the characterization of the non-epitaxial films has been limited to only a few cross-sectional SEM images [225, 226, 239]. Whether TLE can produce non-epitaxial films which meet or exceed the characteristics of those deposited by traditional PVD techniques such as sputtering and electron beam evaporation has not yet been determined.

Here, we report the deposition of ultrathin Ni films using a home-built TLE system employing a 1 kW CW fiber laser with a 1070 nm wavelength. Characterization was performed using ellipsometry, AFM, XPS, and through electrical measurements (see Sec. 3.1). A deposition rate of 0.35 Å/sec was achieved with 177 W of CW laser

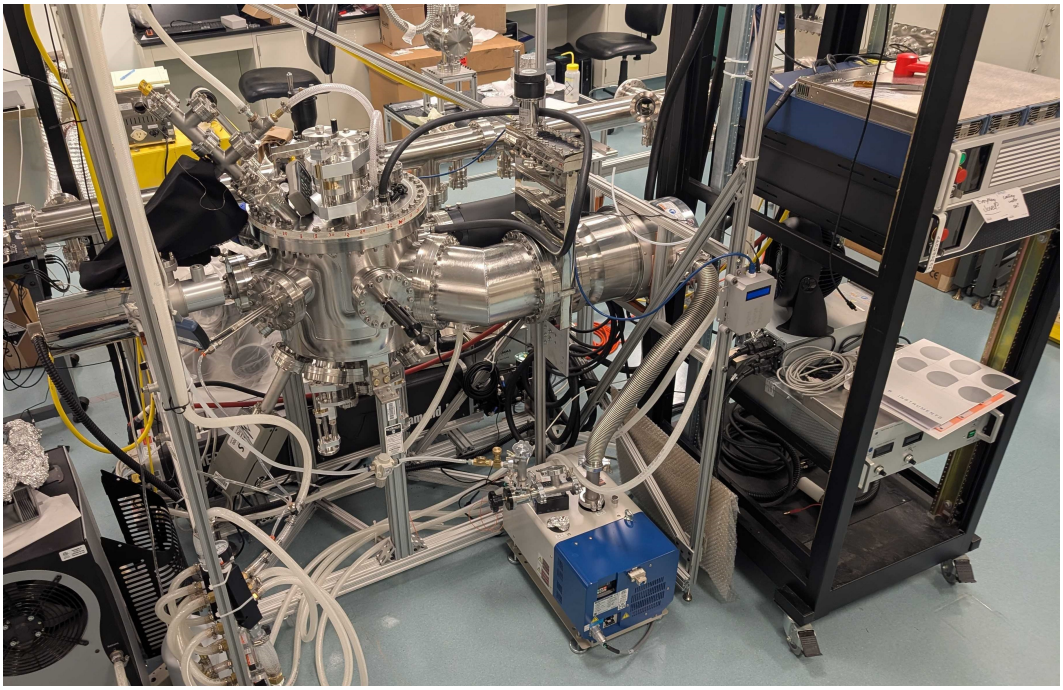

Figure 4.2: Photograph of the TLE system at Caltech. At the top left is the laser delivery system, and to its right (out of the page) is the bellows mounted to the substrate holder. Around the center from the left to right are a RHEED system, QCM, shutter control, turbopump, and RHEED camera (partially obscured), respectively. At bottom are the RGA and two bellows to which the target holders are mounted.

power. The deposited film was 14.7 ± 0.1 nm thick and exhibited RMS roughness $R_q = 1.10 \pm 0.14$ nm. The electrical resistivity, known to be a sensitive probe of the quality of electrically-conducting films, was measured to be 22 ± 0.2 $\mu\Omega$ cm, in quantitative agreement with the best prior value reported for Ni films of a similar thickness. We also provide an overview of the system design and discuss design considerations for key system components such as the beam delivery system. This work indicates that TLE-deposited films are of equal quality to the best films made by other evaporation methods, and the provided system design details will enable broader adoption of the technique, advancing the science and practice of thin film deposition.

4.2 Experimental details

Overall system

We begin by presenting the details of our home-built TLE system. A photograph of the system is shown in Fig. 4.2. It consists of a water-cooled vacuum chamber (Kurt J. Lesker Hydra Cool™) with a turbopump providing a base pressure below

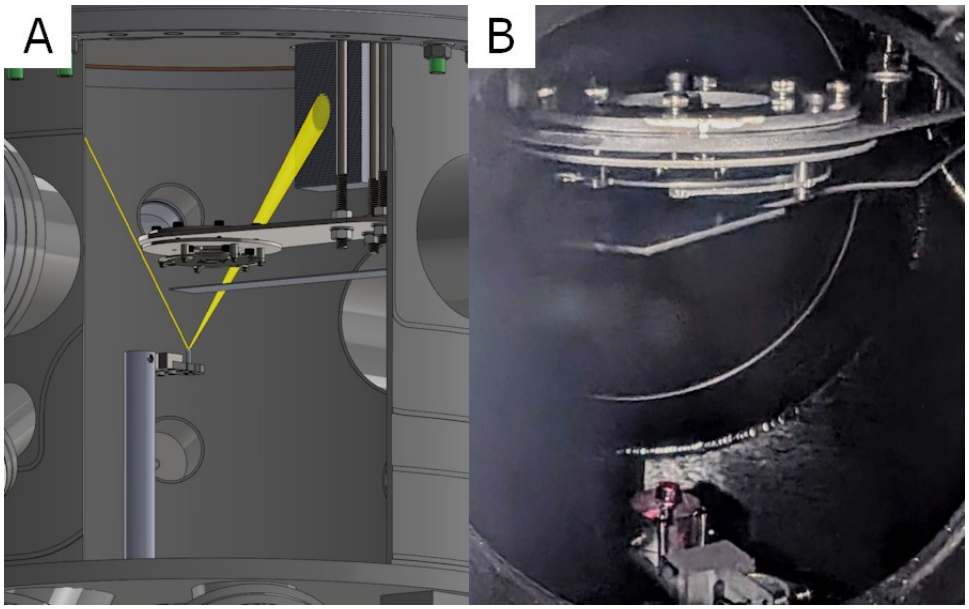

Figure 4.3: (A) Cut-away rendering of the system interior from the position of the QCM. The laser is shown in yellow, specularly reflecting off the target onto the beam dump. Above the target are the shutter and substrate, suspended from its holder. (B) Photograph from a viewport showing the system interior as-built.

10^{-9} mbar. Inside the chamber are a target holder and substrate holder, which are both mounted on bellows to enable target alignment and sample transfer. The relative positioning is shown in Fig. 4.3. In Fig. 4.3a we show a rendering from the position of the QCM in Fig. 4.2. This rendering shows the calculated beam path and its position upon the water-cooled beam dump. In Fig. 4.3b we show a photograph of the chamber internals from the position of the viewport, which is located 90°clockwise from the QCM in Fig. 4.2.

For *in-situ* control, the chamber is equipped with a titanium deposition shutter mounted on a linear push-pull feedthrough. *In-situ* monitoring is provided by a quartz-crystal microbalance (Telemark), a residual gas analyzer (SRS RGA200), and cold-cathode/pirani combination gauge (Edwards nWRG). The chamber is also equipped with a RHEED system, however this was not used in this work.

Target and holder

Three iterations of the target holder were tested, and the final was used for the depositions described within this work. These three versions are shown in Fig. 4.4. Previous works have typically used completely free-standing sources in which the source sits on top of a refractory platform. In our system there is not currently a means to load and unload loose targets without significant effort. Therefore, the

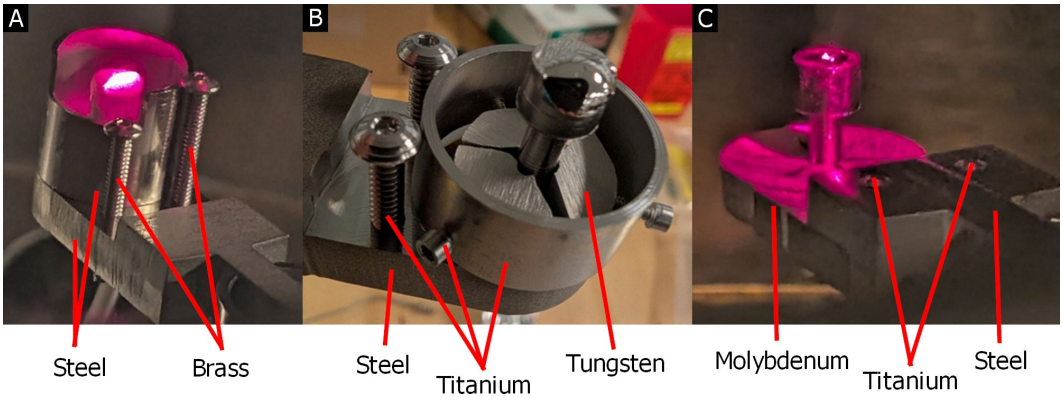

Figure 4.4: (A) First version of the target holder. A steel cantilever is used to hold the assembly together. Tungsten fingers held in place by steel screws (obscured) hold the target in place. A steel shield surrounds the target to limit the flux, and this is held by brass screws. A thermocouple is inserted under the shield and held under the target by a ceramic screw (obscured). (B) The second version of the target holder. The cantilever remains unchanged, as does the thermocouple and ceramic screw. The tungsten fingers have been modified so that they are pressed in from the sides via titanium screws, which are threaded through a titanium shield. The brass screws have been replaced with titanium. (C) The third version of the target holder. All complex hardware on the cantilever has been eliminated. Here, the last half of the cantilever is made of molybdenum with slots cut to increase the length heat must conduct to reach the first, steel portion. The two halves are mated using titanium screws. The target is mounted by a press fit into a hole in the cantilever, in which the thermocouple tip is placed. A rendering of this version is also shown in Fig. 4.5b

design was oriented around insertability through a DN40CF flange. Because the flange was not exactly below the desired position for the target, an offset was required, and the simplest solution was to use a mobile cantilever so that the apparatus would still fit through the mounting flange.

The first iteration, shown in Fig. 4.4a utilized a fully steel cantilever, a cylindrical steel "shield" which was positioned around the target to limit the solid angle of flux, brass screws to hold the shield in place, and tungsten fingers mounted by steel screws to hold the target in place. A monitoring type-C thermocouple was routed between the cantilever and the shield and pressed against the bottom of the target by a ceramic screw. It was found that at the laser powers required to melt niobium, the temperature of components nearby the target was high enough that they were either damaged or had begun to evaporate themselves. For instance, the steel screws holding the tungsten fingers, despite being in 2nd order thermal contact with the target, melted above the cantilever. The brass screws, in 4th order thermal contact with the target, started to have more volatile constituents (lead and zinc) evaporate.

To solve these issues, a second version was fabricated, shown in Fig. 4.4b, and also in Fig. 4.3b. Here, the shield and screw materials were swapped for titanium, which solved problems with evaporation. The shield was also shortened as it was now intended only for mounting the target, rather than limiting the flux. The steel screws holding the tungsten fingers were removed in favor of titanium screws mounted from the side. However, assembly was not easy and the steel cantilever remained, leaving concerns about further contamination if the steel got sufficiently hot.

The third version, which is the version currently in use, is shown in Fig. 4.4c and Fig. 4.5b. Here, all hardware at the end of the cantilever has been eliminated. The cantilever has been split into two halves: the half farthest from the target is made of steel for machinability, and the half which holds the target is made of molybdenum, a refractory metal. The design of the steel half is unchanged from prior versions. The molybdenum half has a blind hole near the end in which the thermocouple tip is placed and then the target is pressed in. This half also has cuts to increase the length that heat must conduct through to reach the steel half of the cantilever. The two halves are affixed using titanium screws.

Finally, the cantilever is supported by a titanium screw which also served as a hinge pin, mounted to the end of a steel tube shown in Fig. 4.5a. Within the tube is routed the type-C thermocouple wires, insulated using ceramic beads. The rod is mounted to an aluminum flange adapter, which is screwed into a type-C conflat thermocouple feedthrough using vented screws.

The target used is shown in Fig. 4.4c. In this work, the target consisted of a 12.7 mm long, 6.35 mm diameter Ni rod (Lesker, 99.995%) which was machined down to 3.13 mm at the base to minimize the thermal conductance to the target holder. We chose Ni for this work to facilitate comparison of electrical data in the literature and because it is less technically challenging to evaporate compared to the refractory elements. Although Ni was primarily chosen for experimental convenience, our findings may be applicable to other metal films, including refractory elements, for which thermal evaporation remains difficult.

We note that without active cooling, the molybdenum half of the cantilever becomes hot enough during deposition that oxidation would be expected if reactive gases such as O_2 were present. In the present case, deposition was performed in vacuum so that this issue is irrelevant; however, future designs will incorporate water cooling of the target holder and a means of exchanging the target without removing and remounting conflat hardware.

Substrate and holder

The substrate and its holder are shown in Fig. 4.5c. A 1×1 cm^2 sapphire substrate (University Wafer, C-plane, SSP) is mounted on a molybdenum disk that suspends the sample upside down. The disk has flags on each end to enable substrate transfer, and molybdenum strips are strung through the corners of a central hole to support the substrate. The disk is suspended by steel fingers that are mounted to a cantilever suspended by steel rods from a flange fitted onto an adjustable bellows. The bellows is lowered so that the substrate is $\sim$ 70 mm above the target. Prior literature used a working distance of $\sim$ 60 mm [225–227, 245], and as such we expect approximately a 25% decreased flux, assuming all other parameters are the same.

Although this design is attractive for simplicity, it does not permit sample rotation. Future implementations will employ a fully concentric design to facilitate sample rotation. While this design is compatible with substrate heating, this was not employed in this work but is under active development using CO_2 laser heating as discussed in Ref. [256]. The substrate was cleaned by rinsing with acetone, isopropanol, and deionized water. It is expected that future work employing both more rigorous cleaning using piranha solution and substrate heating will result in higher film crystallinity, lower surface roughness, and lower O and C contamination.

Deposition procedure

The deposition procedure consisted of the following steps. First, the system was pumped down to a base pressure below 10^{-9} mbar. Because the chamber has not yet had a significant amount of deposition on the walls, no chamber bakeout was required or performed to achieve this pressure. A Ti shutter on a linear translation stage covered the sample for the entire process until deposition was initiated. The laser was turned on and the power was held between 119 and 144 W for approximately an hour to bake out adsorbed gases from the target and its holder. After the pressure stabilized around 10^{-7} mbar, the power was steadily increased until a steady-state deposition rate was measured in the QCM. The shutter was then opened to allow deposition. For the present study, the deposition rate was 0.35 Å/sec.

4.3 Optical delivery design

As in any PVD method, the energy delivery components are the most critical parts of the entire system. Fortunately, with TLE the energy source is located outside of vacuum, an advantage shared only by PLD and sputtering. This feature makes the system easier to modify, as the majority of the hardware does not need to be vacuum

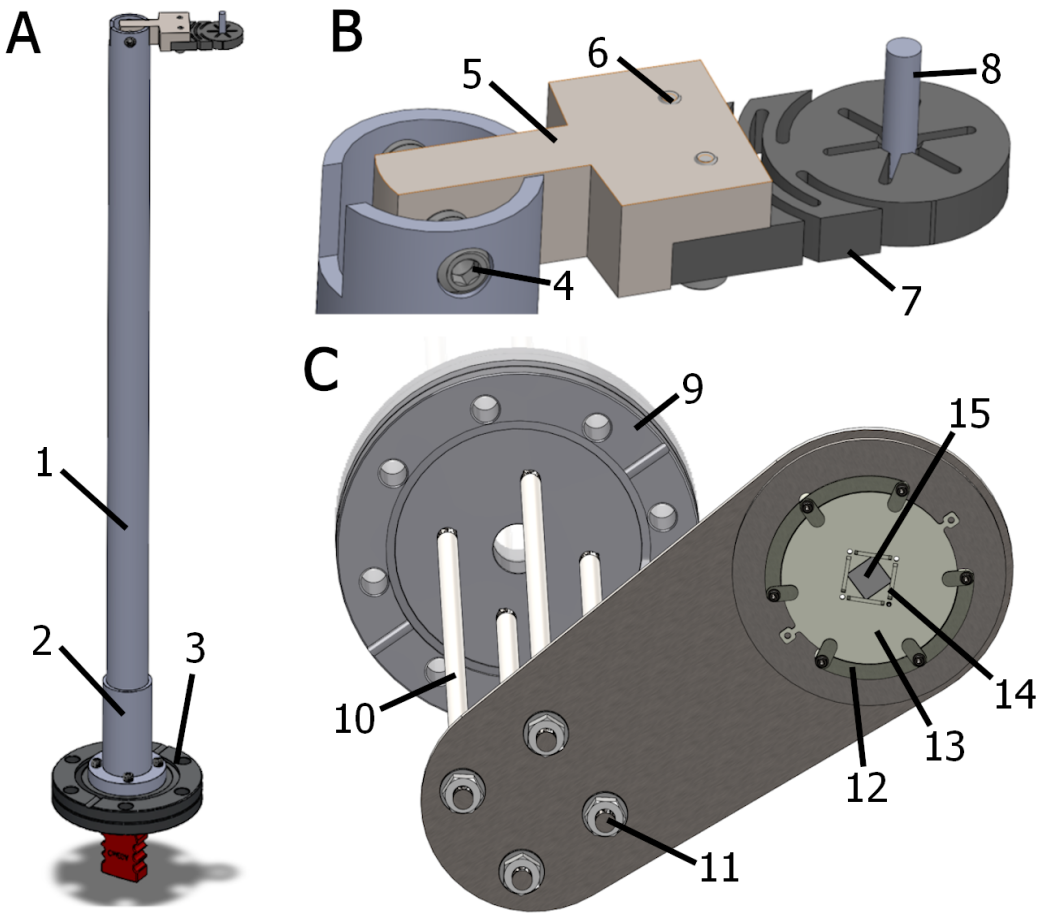

Figure 4.5: (A) Target holder apparatus, with thermocouple routed within the interior. 1. Steel tube 2. Aluminum flange adapter 3. C-type thermocouple feedthrough. (B) Target holder cantilever, with thermocouple routed underneath. 4. Titanium screw used as a hinge 5. Steel cantilever support 6. Titanium screws 7. Molybdenum cantilever, with cut outs to increase conduction path between target and screws, and a press-fit hole drilled for the target 8. Target. A photograph of this holder is also shown in Fig. 4.4c. (C) Substrate holder. 9. Conflat flange 10. Steel rods 11. Nuts and washers to mount the cantilever 12. High-temperature steel fingers 13. Molybdenum substrate disk 14. Molybdenum strips 15. Substrate chip.

compatible. Furthermore, laser light is often used in many different sciences and industries, meaning many components can be purchased off-the-shelf. In our design process, we attempted to use as few custom components as possible.

The first design for the optics used a 3D printed collimator mount which fits on a standard 60 mm optical cage system. A single lens was also placed on the cage system. The rods forming the cage were mounted to an adapter plate on the anti-reflective window. A concave mirror, shown in Fig. 4.6a, was fitted behind the window to redirect the laser beam into the chamber and focus the beam onto the target. A few problems were found with this design: First, the 3D printed mount gave translational degrees of freedom but not rotational. Second, the single lens inadequately focused the beam, resulting in a large beam spot at the target. Third, the cage system was not designed to support the weight of the collimator, resulting in a slow mechanical relaxation after focusing that would result in the beam spot drifting off-target. Fourth, the mirror design was insufficient to dissipate the heat absorbed from the laser beam.

The first mirror used was a gold-plated off-axis parabolic aluminum mirror. This mirror was mounted on an adapter plate using the existing tapped holes in its base, then the adapter was screwed into a rod intended to offset the mirror to the appropriate distance from its mounting flange. The adapter plate and rod were both made of aluminum. It was believed that the rated reflectivity of approximately 97% at 1070 nm was high enough that the mirror could be used for some time before overheating would occur. However, a few things were realized after the mirror was destroyed as shown in Fig. 4.7. First, the reflectivity of metals generally decreases as they are heated, sometimes significantly depending on the material. Second, deposition on the mirror very quickly changes the reflectivity towards that of the deposited material. Third, gold and aluminum will alloy at sufficiently high temperatures forming a non-reflective intermetallic. Lastly, the mounting apparatus was not sufficient to conductively dissipate the heat the mirror absorbed. During operation, the tee which the mirror was inside of got too hot to touch owing to significant radiative heat transfer. After some time the temperature at the target started decreasing rapidly, indicating a complete mirror failure due to thermal runaway from the three previously listed factors. To address this issue, both the mirror and mounting structure had to change.

The second iteration of the optical design featured multiple modifications. First, a single mirror mounting rod was used instead of the two-piece design, which

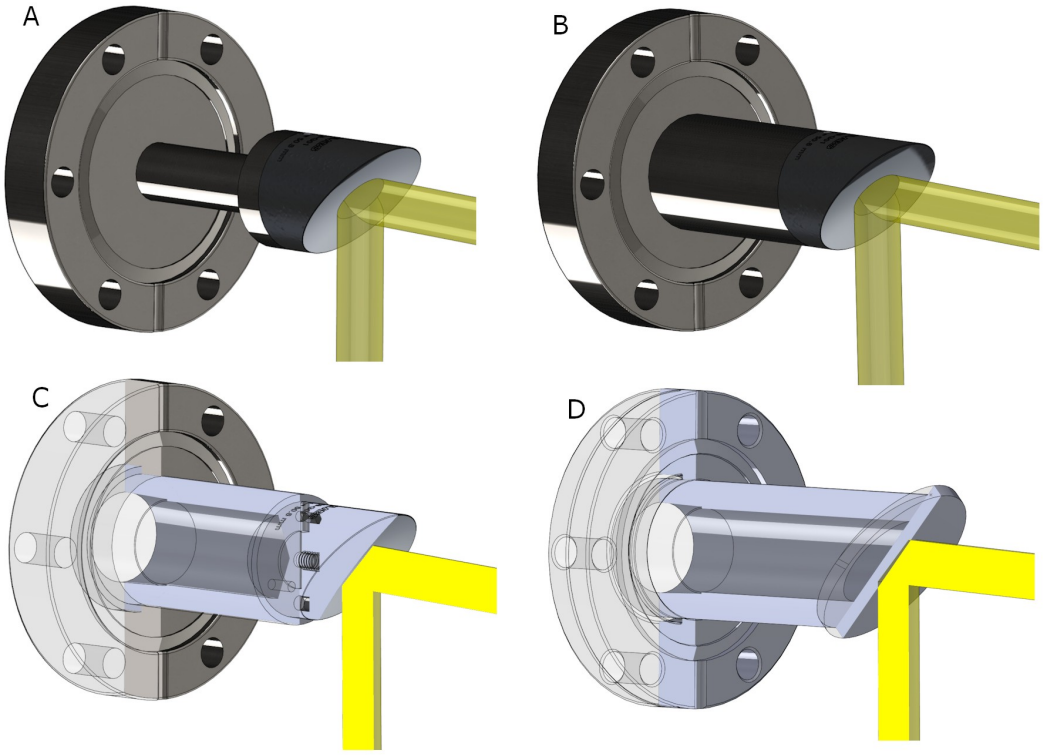

Figure 4.6: Iterations of the TLE mirror design. (a) Off-the-shelf mirror mounted via a small adapter to a standoff rod. This design has three vacuum interfaces from the mirror to the mounting flange. (b) Off-the-shelf mirror mounted via a single standoff rod. This design features two vacuum interfaces from the mirror to the mounting flange. (c) Off-the-shelf mirror mounted via a hollow, water-cooled standoff. This design features one vacuum interface between the mirror and the cooled mount, which can be filled using thermally conductive pastes. (d) Current design with the mirror welded onto a hollow standoff tube. This design has no vacuum interfaces; the mirror backside is directly water-cooled.

Figure 4.7: Mirror failures caused by thermal runaway. From left to right: New gold-plated concave aluminum mirror [257], damaged gold-plated mirror, new protected aluminum mirror [257], damaged protected aluminum mirror.

eliminated a vacuum interface and increased thermal conductivity. Second, the size of the rod connecting the mirror to the flange was also increased, further increasing conductivity. These changes are shown in Fig. 4.6b. Third, a protected aluminum mirror was used rather than a gold coated one, eliminating the possibility of alloying. Fourth, a new 3D printed collimator mount was fabricated which linked the translational and rotational degrees of freedom to allow the collimator to be positioned on a spherical surface with the center-point being at the mirror face. Lastly, a second lens was added to the optical cage which aided in both focusing and mechanical stability. With these changes we found that the new mirror design allowed for longer operation. However, the changes were still insufficient to dissipate heat, and the mirror was eventually destroyed as shown in Fig. 4.7. In this case, thermal runaway due to the decreasing reflectivity of metals with temperature and the large absorption by a niobium film were the cause of failure. It was also found that the 3D printed mount did not adequately allow the laser to be focused on the mirror center, which is clear in Fig. 4.7 and might have contributed to the failure as the heat was concentrated near the mirror edge. Lastly, the drifting of the laser spot due to the mechanical stability of the cage system was still a problem.

The third iteration of the design is shown in Fig. 4.8, minus the thermocouple. Here, we swapped out the off-the-shelf cage system for a custom-made optical mounting system using a slotted baseboard. Rather than a 3D printed collimator mount, we use a kinematic laser mount which gives precise angular control. The kinematic mount is mounted on slots to allow side-to-side adjustment, and the entire optical apparatus is mounted with slots yielding up-and-down adjustment. Therefore, this design allows for independent control over both angular and translational positioning. The two-lens design was kept for focusing. The mirror mount was upgraded by using a custom-fabricated hollow-tube design shown in Fig. 4.6c. Here, cooling water flows through the mounting structure, leaving only a single vacuum interface between the mirror and the water-cooled mount. To attach the mirror, a threaded rod was machined onto the end of the water cooled rod, and a matching central hole was drilled and tapped in the mirror. With these changes stable alignment of the laser was now possible. However, the mirror was still found to overheat and eventually melt. To address this, the thermocouple shown in Fig. 4.8 was added, which monitored the mirror temperature, and platinum paste was used to enhance the thermal conductivity between the mirror and its mount. With these changes it was found that the deposition could be performed for around 45 minutes while limiting the mirror temperature to below 100 °C. This setup was the one used to fabricate

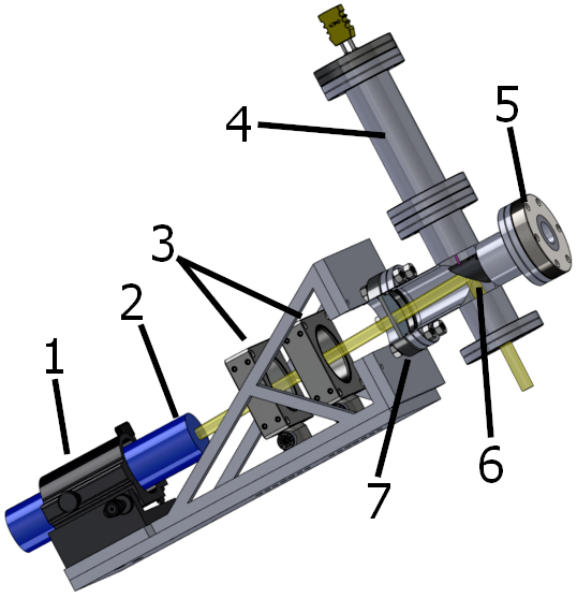

Figure 4.8: Rendering of the fiber laser delivery system. 1. Kinematic laser mount 2. Laser collimator 3. Lenses 4. Thermocouple 5. Water cooled mirror mount 6. Mirror 7. Laser window.

nickel films.

Current and future work is to permanently prevent the mirror from failing by directly water-cooling the backside. To accomplish this, we are investigating the design shown in Fig. 4.6d. This design features a thin (~2 - 4 mm) flat stainless steel or aluminum face plate which is welded directly to the water-cooled mounting structure. The faceplate is polished to a mirror finish, meaning we are able to water-cool the backside of the mirror directly without any vacuum interfaces. Due to the change from an off-axis parabolic mirror to a flat mirror, the lens design will also change to provide the focusing needed. Another advantage of this design is the ability to make the mirror reflect at an angle other than 90°, which in theory allows us to fabricate a mirror such that we can eliminate the need for angular adjustments of the collimator and instead focus the laser onto the target using only the rotation of the mirror mounting flange. Furthermore, we are investigating the use of a pinhole aperture to minimize deposition onto the mirror, and high-quality imaging of the target surface during deposition. These modifications were not used in this work except where mentioned.

The choice of laser wavelength is critical to both the efficiency of target heating as well as the choice of window and lens materials. Although the absorbance of light by metals is a complicated function depending on wavelength and the specific

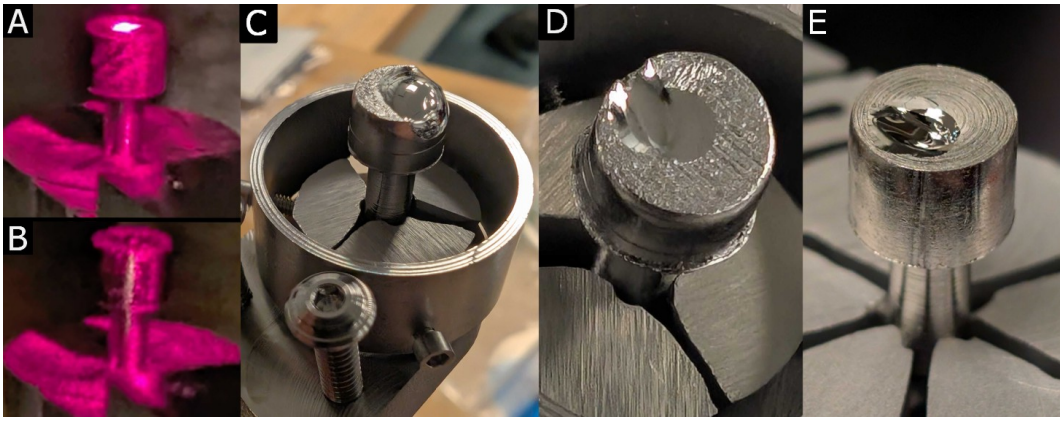

Figure 4.9: Photograph of the Ni target mounted in the chamber (A) before deposition and (B) after deposition. A red guide laser is on in both images. Before deposition, the laser is observable from the camera due to diffuse reflections from the surface before melting. After deposition, the guide beam is not visible due to the increased specularity of the melt pool. (C) A niobium target on which the laser spot was too large, causing the melt pool to reach the edge of the surface. (D) Niobium target with smaller melt pool corresponding to a smaller spot size. The melt reaches the edge due to the spot moving as the optical setup relaxed. (E) Nickel target shown in (A) and (B). The melt pool, while off-center, is well contained within the target top.

element or alloy, shorter wavelengths are generally absorbed better than longer ones [223, 254]. At the time of this writing, the most powerful commercially available CW or QCW lasers at various wavelengths include the CO_2 laser (10.6 µm, up to $\sim$ 20 kW), fiber laser (1070 nm, up to $\sim$ 100 kW), doped YAG (1030 - 1064 nm, up to $\sim$ 20 kW), frequency-doubled doped YAG (515 nm, up to 3 kW), blue diode (445, up to 6 kW), and excimer (193-308 nm, up to $\sim$ 4 kW). The CO_2 laser is not absorbed well enough to be considered as a target heating laser (although it works very well to heat oxides, and as such is useful for substrate heating). YAG technology is generally more expensive than fiber-based lasers of similar powers, making fiber lasers more attractive in the NIR range. Frequency-doubled YAG is even more expensive. While blue diode and excimer lasers make ideal choices in terms of wavelength, both technologies are still being developed, and existing commercial units are more costly than fiber lasers. Due to these factors, and the existing literature already using NIR lasers, we chose to use a fiber laser with wavelength 1070 nm.

A choice must also be made regarding the beam spot size. Prior to melting, the target surface is flat and both diffusely and specularly reflective, as shown in Fig. 4.9a. After melting, a mirror-like melt pool results in nearly complete specular reflection

of any laser power not absorbed, as shown in Fig. 4.9b. To avoid unpredictable angular variations of the specularly reflected beam and to ensure that the melt pool is contained within the target surface, we opted to focus the beam to a sub-mm diameter. This size is slightly smaller than that used in other TLE works (c.f. 1.1 mm [239]). It is known that a large melt pool results in a convex surface due to surface tension [239], which could specularly reflect the beam in an unpredictable direction and potentially damage system components. This was experienced with a niobium target (pictured in Fig. 4.4b and Fig. 4.9c) where the melt pool reach the edge nearest the incident laser, resulting in a surface which reflected the laser upward and onto an aluminum shutter designed to block flux from the substrate, melting it (in the current design this has been replaced with titanium). While a smaller melt pool might also result in a non-planar surface and a similarly unpredictable reflection, this option was ultimately selected. Nearly ideal melt pools are shown for niobium in Fig. 4.9d, which also exhibits the laser drift discussed earlier in the first and second iterations of the optics design, and for nickel in Fig. 4.9e.

A concise description of the final system shown in Fig. 4.8 is as follows. We use a 1 kW fiber laser (IPG Photonics, YLR-1000-WC) which terminates in a water-cooled free-space coupler and collimator (IPG, D30 F100 AC HLC-8), which is mounted in a kinematic laser mount to enable fine beam alignment. Two C-coated lenses (Thorlabs LA1301-C-ML and LC1093-C-ML) are used to focus the beam to sub-millimeter diameter on the target. An antireflective window is used to pass the beam into vacuum (Lesker VPZL-275LYAG). The final optical element is an aluminum off-axis parabolic mirror (Edmund Optics 35-590) mounted on a water-cooled rotatable flange. Pt paste (Tanaka Kikinzoku TR-7091T) is used to enhance thermal contact between the flange and the mirror. A type K thermocouple is placed in contact with the mirror to monitor its temperature. A water cooled beam dump is placed in the path of the beam specularly reflected by the target.

4.4 Results

Rate and flux stability

We next present qualitative features of the deposition process. The deposition rate measured by QCM versus inverse laser power is shown in Fig. 4.10. To account for the geometric factor from the positioning of the QCM relative to the sample, the measured rates were scaled to match the measured film thickness. The deposition rate exhibits the expected Arrhenius dependence on laser power [226, 239], with a power of 202 W yielding a deposition rate of 0.98 Å/sec.

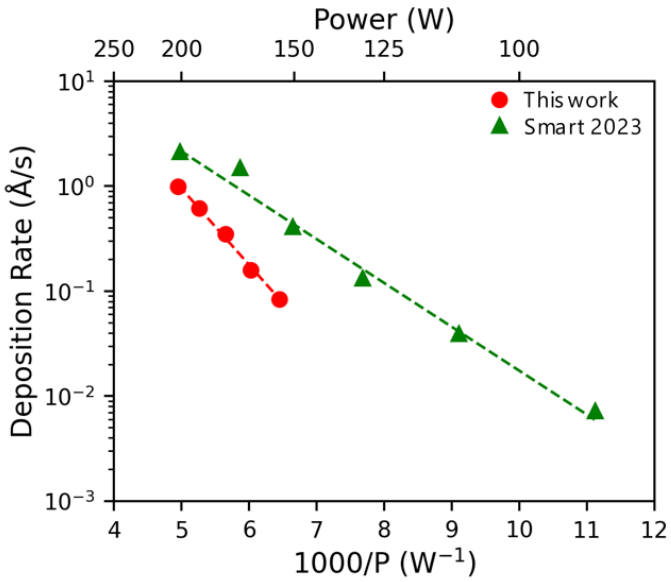

Figure 4.10: Deposition rate measured by QCM versus inverse laser power (symbols) and a fit line. Present data (red circles) shown along with data by Ref. [239] (green triangles). The present data follow an Arrhenius relationship: Rate [Å/s] = 4064 exp(−1673/P[W]).

During deposition, flux instabilities (on second timescales) and slower variations (minute timescales) were observed, as shown in Fig. 4.11. The slower variations, which manifest here as a downward trend in Fig. 4.11a, have been previously reported and are discussed in Refs. [239, 241]. These flux variations might be attributable to a change in target surface morphology induced by melting and evaporation as well as a decrease in the mirror reflectivity as less-reflective material is deposited on the aluminum mirror. Possible mitigation strategies include scanning and defocusing the beam to increase the effective evaporation area at the target surface, employing a solution to minimize deposition on the mirror (e.g. using an aperture), or postpone sample fabrication until the mirror is suitably coated such that the reflectivity stabilizes [239, 241]. We did not employ any technique, resulting in a flux variation of up to 10% over any run. The flux instabilities, which occur on second-timescales and are shown in Fig. 4.11a and Fig. 4.11b, were on the order of 2-8% (as measured by QCM), depending on the deposition rate. This fluctuation noise is approximately 3× larger than the background QCM noise. The origin of these fluctuations is not clear at present. Note that by taking a rolling average (or equivalently, querying the thickness or deposition rate at longer intervals) these fluctuations are dramatically reduced, as shown in Fig. 4.11b (this data was taken using the stainless steel mirror in Fig. 4.6d and a nickel target, once the flux rate stabilized). By averaging only

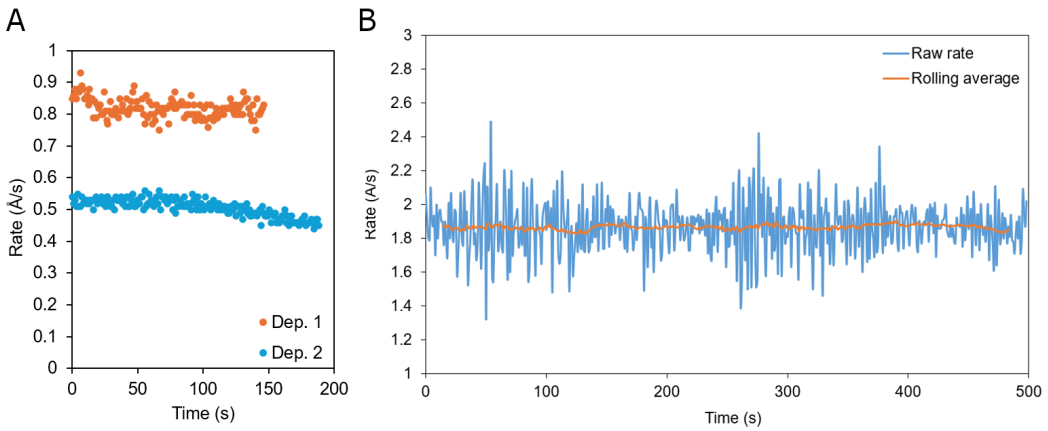

Figure 4.11: Measured, unscaled deposition rate versus time for (A) two different depositions whith an aluminum mirror, the standard deviation relative to the mean of deposition 1 (deposition 2) is 3.8% (2.7%). (B) A deposition using a directly water-cooled stainless steel mirror (see Fig. 4.6d). The raw data (taken in one-second intervals) is shown in blue while the 30 second rolling average is shown in orange. The standard deviations are 8.3% and 0.7%, respectively.

30 seconds of data, the standard deviation is decreased by an order of magnitude from 8.3% to 0.7% of the mean deposition rate. Other works have tended to report flux in 10-minute intervals, which misses the fluctuations at these shorter timescales [225, 239, 241].

We note that the observed deposition rate was lower than that previously published in Ref. [239], which concluded that higher energy densities will increase the deposition rate. The source dimensions were also different, with the referenced data set using a 12.7 mm diameter source with a height of 4 mm. However, a smaller source diameter yields lower energy losses through radiation, and thus it should be expected that a higher deposition rate would be achieved, the opposite of what was observed. Our laser was also focused tighter than it was in the reference, which should also increase the flux. Because of these factors and the observed discrepancy in flux being larger than the $\sim$ 25% estimated from the working distance, it is likely that the assumption that conduction does not play a major role is invalid in our setup. In our setup, the target is pressed into the holder, and so conductive heat loss from the target is sufficient to heat the holder to well above 1000 °C as indicated by the orange color of blackbody radiation. Because conductive heat loss is linear with temperature difference while radiation and evaporative loss vary more strongly, conductive loss will be most pronounced at lower temperatures, which is possibly the reason the difference between data sets is most significant at lower powers. This

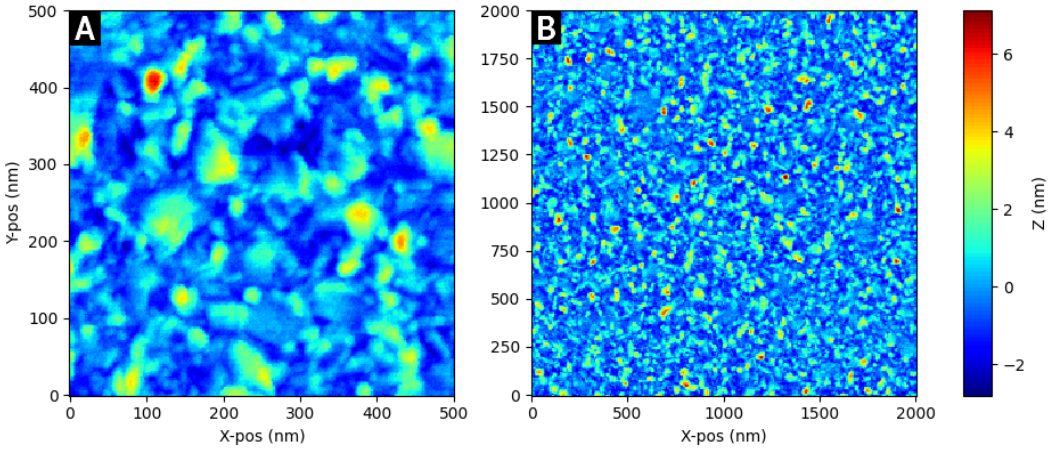

Figure 4.12: AFM scan of the TLE-deposited Ni film surface. (A) 500 × 500 nm scan (256 lines, 0.3 Hz) and (B) 2 × 2 µm scan (256 lines, 0.5 Hz). The RMS roughness $R_q = 1.10 \pm 0.14$ nm.

finding highlights the necessity of minimizing thermal contact if the efficiency of evaporation at low powers is a concern.

Surface roughness

Next, we examine the physical characteristics and surface morphology of the films. The film thickness was measured using ex-situ ellipsometry on a J.A. Woollam M2000 with the built-in profiles for sapphire and Ni. The measurement yielded a value of 14.7 ± 0.1 nm, which was not changed by incorporating roughness or native oxide. This value is quantitatively consistent with step height measurement via atomic-force microscopy (AFM) performed on a step formed by the substrate holder. Although no substrate rotation was used, the thickness variation across the sample should be limited to 0.2% given the expected cosine flux distribution, which is less than the measurement uncertainty [239]. The film surface morphology was characterized using a Bruker Dimension Icon AFM in PeakForce Tapping mode with a ScanAsyst-Air probe. The AFM scans showing the surface morphology at small and large scales in Fig. 4.12a and Fig. 4.12b, respectively. The same surface morphology and roughness is observed at both scales. These scans indicate that the sample exhibits the smoothness expected of a thermally evaporated thin metal film growing by nucleation and coalescence [258], with RMS roughness $R_q = 1.10 \pm 0.14$ nm.

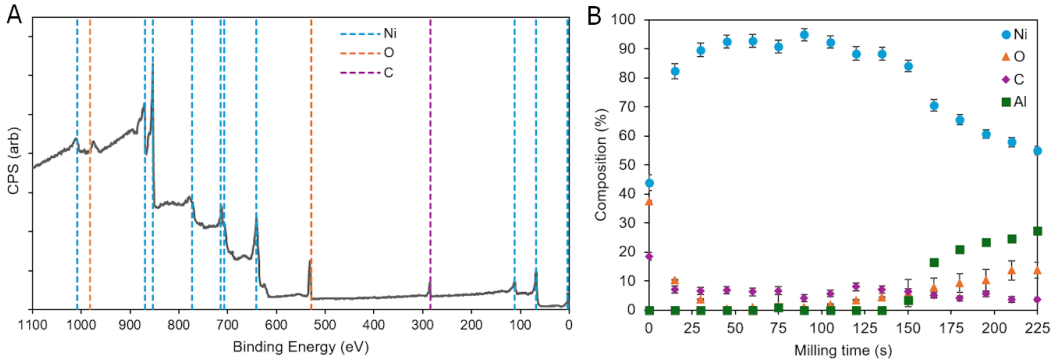

Figure 4.13: (A) XPS spectrum of the nickel film surface. Oxygen, carbon, and nickel peak locations are shown according to the Kratos element library. (B) XPS compositional analysis with depth profiling. Detected elements include nickel (blue circles), oxygen (orange triangles), carbon (magenta diamonds), and aluminum (green squares). After 150 s of milling the film becomes thin enough that the underlying sapphire substrate begins to appear in the XPS signal. Error bars represent the area uncertainty reported by CASA XPS.

Chemical composition

The chemical composition of the film was characterized using x-ray photoelectron spectroscopy (XPS). Although not as sensitive as other techniques like secondary ion mass spectrometry, XPS still provides confirmation of the presence of metallic Ni and bounds the O, C, and other impurity content in the film. The measurement was performed using a Kratos Axis Ultra XPS using an Al K α source and used an ion mill for depth profiling. The surface XPS spectrum in shown in Fig. 4.13a, and the composition throughout depth profiling in Fig. 4.13b. The detected elements were Ni with some amount of O and C. The O content ranges from approximately 0.6% to 2% in the bulk, while the C content ranges from about 7% to 12%. We attribute the C content to the adventitious C that remained on the sapphire substrate prior to deposition, which diffused into the film as a result of indirect heating of the substrate by the hot target during the deposition process. This adventitious C may also be responsible for a portion of the O content. No other elements were found within the detection limit of $\sim$ 0.2%, indicating that no metallic contamination from the target holder occurred. In a future work, secondary ion mass spectrometry will be employed to better characterize the concentrations of trace impurities, and more aggressive cleaning of the sapphire substrates (c.f. piranha wet clean) will be used to eliminate residual adventitious carbon.

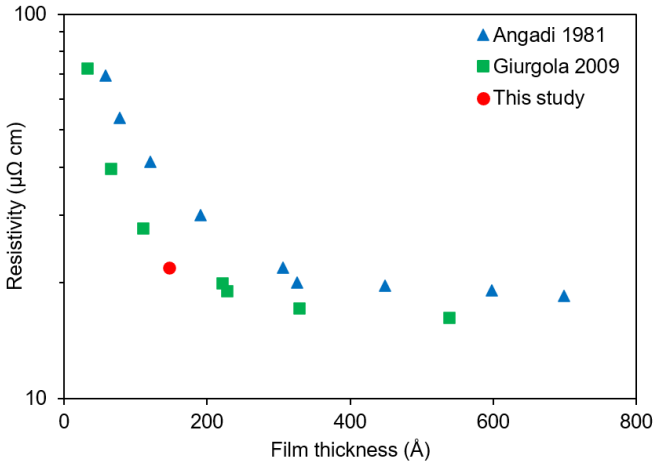

Figure 4.14: Electrical resistivity versus film thickness at room temperature. The measurement from this work is indicated as the red point (thickness of 147 Å), and the uncertainty is smaller than the symbol. Referenced data from Ref. [260] (blue triangles) and Ref. [259] (green squares).

Electrical resistivity

Finally, the electrical resistivity was measured using the van der Pauw method (vdP). The resistivity of thin films is well-known to be a sensitive probe of the structural quality and chemical purity of electrical conductors, and data is readily available in the literature for Ni. Wirebonding was performed using Al wires with a Westbond 7476D Wire Bonder, and the vdP measurement was performed using a Keithley 2400 SourceMeter. At room temperature, the value was measured as 22.0 ± 0.2 $\mu\Omega$cm. Fig. 4.14 plots this value along with other values for Ni films of varying thickness from prior studies. It is observed that the measured value is compatible with those reported for films of a similar thickness by Ref. [259], which utilized magnetron sputtering. The resistivity is approximately 33% lower than the best measurement of thermally evaporated ultra-thin Ni by Ref. [260]. The low resistivity could be due to a lower concentration of electrically-active impurities, grain size, or grain orientation. We conclude that the deposited films are of comparable quality to films deposited using conventional PVD techniques like e-beam evaporation and sputtering. Future work will characterize the temperature-dependence of the resistivity, the residual resistance ratio for films grown via multiple PVD methods, film crystallinity, and the resistivity dependence on growth rate. These measurements will provide further insight into the structural quality and chemical purity and may provide insights into the high electrical conductivity.

4.5 Discussion

The development of the major modern PVD techniques including MBE, E-beam, sputtering, and PLD occurred nearly simultaneously throughout the 1960s. While developments since have certainly brought significant changes and improvements to those technologies, the PVD scene has largely remained unchanged in terms of general capabilities. Without specialized equipment, many interesting materials incorporating elements such as W, Mo, Nb, Ta, which are especially of interest within the quantum materials community [261–263], remain difficult or impossible to synthesize as a high-quality film using an additive process.

This work is the first modern independent validation that thermal laser evaporation is a technique of promise, complementing the work done by the group at the Max Planck Institute. While other PVD techniques achieved dominance owing to the technological restrictions of TLE, recent developments in laser technology have now made the technique viable. In addition to nickel, which has a melting point of only 1455 °C, we are currently working on evaporating niobium, which has a melting point of 2470 °C, making it far more representative of other refractory metals. Furthermore, because Nb is a superconductor at low temperatures, the transition temperature may be used as a more sensitive measure of film quality than the room temperature resistivity.

Key challenges and questions still remain to be solved or answered: First is to determine if there is a means of protecting the final optic (mirror) such that deposition is completely eliminated. Otherwise, an accurate means of monitoring the laser power delivered to the target should be developed. Second, while most solid elements have been successfully deposited, only a handful of materials and compounds have undergone characterization. Additional studies on the properties of TLE-grown films are necessary to fully evaluate the technique compared to other PVD methods, such as our future work with niobium. Third, the effect of using other laser wavelengths (such as 515 and 445 nm) would be worthwhile as the current NIR lasers can be difficult to monitor optically and are absorbed less than visible lasers. Tangentially, some studies have shown that light absorbance can be increased by enhancing free-carrier absorption, for instance by partially doubling the frequency of incident light to stimulate interband transitions [224]. This or similar methods to enhance the absorptivity of the target would be useful for increasing the efficiency of this technique. Fourth, while TLE is less prone to generating particulates than PLD, it has still been observed in literature [224] and is likely a version of the

"spitting" issue which occurs in E-beam systems to this day. The issue is also still not well understood, both in terms of the physical mechanism and how to prevent it. A number of techniques to limit the production of particles have been investigated [224], and with modern technology some could be worth revisiting. Finally, the growth of high-quality thin film compounds containing refractory metals (such as TaAs and WTe_2) should be performed, as this is the most unique feature of TLE.

4.6 Summary

In summary, we have reported the deposition and characterization of ultrathin Ni films using a home-built thermal laser evaporation system. While the system follows the general design for an MBE or E-beam evaporator, a number of components are unique to TLE, for which we give detailed descriptions. Owing to the lack of current literature on the design of these systems, a number of lessons have been learned, which we also relay for the benefit of those who would also design TLE systems. We found that, depending on the TLE target holder design, the assumption in prior literature that conductive heat loss is negligible might not always be true, and we provide flux rate versus laser power data to support this conclusion. We also provide an analysis of roughness, composition, and resistivity for non-epitaxial Ni films deposited on sapphire substrates. The films exhibit smoothness consistent with that expected of thin metallic films grown without substrate heating. Compositional analysis shows no major contamination by elements other than oxygen and carbon. Electrical resistivity matched the expected value for the best quality thin film nickel data available. Our work adds to the growing consensus regarding the promising potential of TLE for deposition of high-quality films and compounds, molecular beam epitaxy, and related applications.

Chapter 5

CONCLUSIONS

5.1 Summary

In this thesis we have aimed to further develop the tools used to design and fabricate semiconductor, superconductor, and optical devices. Improving the performance of cutting-edge devices, as well as creating new types of devices, requires an understanding of the intrinsic material properties and advanced material processing methods. While disparate in terms of the underlying physics, simulation, etching, and deposition are all important parts in the nanofabrication pipeline.

In Chapter 2, we utilized and extended a recently developed *ab-initio* formalism utilizing the Boltzmann transport equation to simulate hot carrier transport in semiconductors by applying it to holes in silicon (*p*-Si). Using the formalism as-is, we predicted the anisotropic DC mobility, diffusion coefficient, and energy relaxation time up to 20 and 12 kV cm^{-1} and temperatures of 300 and 77 K, respectively. While transport coefficients were uniformly overestimated by around $\sim 25\%$, we found that the calculated properties quantitatively reproduce the trends of high-field transport including the electric field-dependence and anisotropy of the mobility and PSD, and the rapid variation of energy relaxation time with electric field at cryogenic temperatures. This finding contrasts prior calculations in *n*-GaAs and *n*-Si which concluded the one-phonon level of theory was inadequate to accurately reproduce the same transport quantities. Furthermore, we extended the mathematical theory to achieve greater accuracy and allow for calculations at cryogenic temperatures down to 6 K. Using this modified theory, we reproduced experimentally observed anomalous phenomena in the cryogenic field-dependent drift velocity and noise spectrum. Through an analysis of the scattering rates, occupation function, and simplified numerical modeling, we provided new physical mechanisms for the occurrence of these two anomalous trends. We find that the additional regime of drift velocity saturation that occurs for $T < 40$ K is due to acoustic phonon emission, in agreement with a prior work. We also found that the peak in the power spectral density of current fluctuations which occurs at 77 K and ≥ 10 GHz is due to the field-dependence of the momentum relaxation time, contrary to the conclusions of prior studies. This work highlights the use of high-field transport and noise properties not only as a

rigorous test of the theory of electron-phonon interactions in semiconductors, but also as a tool to understand the microscopic phenomenon underlying transport and noise in semiconducting devices.

In Chapter 3 we reported a new atomic layer etching process for SiO_2 using sequential exposures of TMA and an $Ar/H_2/SF_6$ plasma. The process improves upon prior processes by achieving EPC above 0.5 Å/cycle while simultaneously eliminating the need for vapor HF, and exhibiting a short cycle time (under 2 minutes) and low TMA pressure requirements (under 250 mTorr). We demonstrated that a sufficient hydrogen content in an Ar/SF_6 plasma reduces the spontaneous etch of SiO_2 to negligible levels while sufficiently modifying the surface for ALE. Using this recipe we observed an etch-per-cycle (EPC) at 400 °C of up to 0.58 Å on thermally oxidized SiO_2. We also examined the etch rate dependence on the film preparation method, finding that sputtered SiO_2 exhibits the highest etch rate of 2.38 Å/cycle compared to PECVD, ALD, and thermal SiO_2. This process exhibits perfect synergy and self-limiting characteristics. We performed surface roughness measurements after ALE and observed a 62% decrease in the roughness of an RIE-roughened surface. Furthermore, XPS reveals less than 2% combined F and Al contamination post-ALE, 89% less contamination than other similar recipes. Our work paves the way for surface smoothing of SiO_2 microdevices using widely-available processing tools, potentially leading to on-chip photonic devices limited only by intrinsic dissipation.

In Chapter 4 we constructed a thermal laser evaporation system, the first to be built in the United States in decades. We provided detailed descriptions of the components unique to TLE as well as the story behind the development of both the optics and target holder designs. We tested the system by depositing ultrathin Ni films, and characterized them via ellipsometry, AFM, XPS, and electrically. A film, which was 14.7 ± 0.1 nm thick, were found to exhibit smoothness consistent with that expected of thin metallic films grown without substrate heating. Compositional analysis shows no major contamination by elements other than oxygen and carbon. Electrical resistivity matched the expected value for the best quality thin film nickel data available. This work indicates that TLE-deposited films are of equal quality to the best films made by other evaporation methods, and the provided system design details will enable broader adoption of the technique, advancing the science and practice of thin film deposition.

5.2 Discussion and future work

Ab-initio hot carrier transport

Previous studies of both polar and nonpolar semiconductors using the *ab-initio* formalism used here have reported that single-phonon scattering is insufficient to reproduce a number of experimental trends [85–87]. The hypothesis in these studies has been that two-phonon scattering is non-negligible, in which a charge carrier either absorbs two phonons, emits two phonons, or absorbs and emits simultaneously. Therefore, quantitative agreement for most normalized transport properties with experiment in *p*-Si comes as a surprise. There is no obvious answer as to why the theory agrees well with experiment for this material system but exhibits discrepancies for the others. However, there are few significant differences between the materials, which must be related to the discrepancy in the model's accuracy since the computational details were the same between studies. Namely, *p*-Si does not have multiple valleys; while multiple bands are relevant to transport in *p*-Si, they all gather at Γ in momentum-space. In the other material systems, there is a wide swath of virtual energy states between conducting bands that could be accessed through two-phonon scattering. However, in this system, all states are relatively close in momentum and therefore are readily accessed by single-phonon scattering events. To investigate this hypothesis, additional material systems should be investigated. Ideally, the results would first be reproduced for similar systems such as *p*-Ge. Calculating transport properties for *p*-GaAs provides a test of whether the simulation retains accuracy for polar materials with a similar valence bandstructure. Finally, measuring and calculating the transport properties of more exotic materials such as IV-VI semiconductors would test whether the single-phonon level of theory holds for *p*-type semiconductors with multiple conducting pockets in momentum space.

Once the calculations can be confidently performed for arbitrary material systems, their usefulness as a probe of physical phenomena would be realized, as demonstrated by the calculations here at cryogenic temperatures. We showed that *ab-initio* calculations, when based on the proper physics, yield a complete picture of the emergent behavior of physical systems. Therefore. physical mechanisms which are difficult to probe experimentally are easily examined *in silico*. While the theory behind a non-monotonic trend in the PSD driven by the energy-dependence of the momentum relaxation time existed in the AC mobility literature, the level of analysis achievable through these calculations was useful in ruling out every other potential cause and in gathering data about the system's behavior at a variety of frequencies where experimental data does not exist. Furthermore, finding that the "shoulder"

in the cryogenic drift velocity arises from the acoustic phonon scattering rates was only possible thanks to the detailed picture of both the scattering rates and field-dependent occupation function obtained through calculations such as those done in this work. While no model is yet perfect and experiments must still be done to validate predictions, the potential for calculations such as this is evident. Therefore, this technique could prove useful for both materials discovery, analysis of experimental findings, and in developing the more practical empirical models used for device simulation.

Atomic layer etching of SiO_2

The most important development in this work is the investigation of a hydrogen and fluorine-containing plasma to replace vapor HF chemistry in a dry etching process. Previously, specialized reactors had to be constructed including gold-plated HF-pyridine canisters and custom treatment systems for the pumped vapors. Commercial systems are not typically designed for use with vapor HF, especially ALD systems such as the one used in this work. While beyond the scope and capabilities of our tool, the detailed mechanisms by which this plasma chemistry replaces HF vapor would be an intriguing path for future research. Namely, whether the vibrationally-excited HF functions differently than vapor HF, and whether any surface reactions are occurring between adsorbed hydrogen and fluorine to prevent spontaneous etching from stray fluorine radicals.

In a similar vein, while this process successfully replaces the immediately-hazardous HF vapor with nontoxic precursor gases, SF_6 is known to be a very potent greenhouse gas. While the plasma products might differ in composition from the inputs, it is unknown what precisely the product gases are of this process, which could still include a significant amount of SF_6. Furthermore, environmental legislation has sought to limit the use of gases like SF_6 in the production of semiconductors. A variety of relatively safe alternatives with lower global warming potentials do exist, such as NF_3 and hydrofluorocarbons such as CHF_3. Similar atomic layer etching recipes for other materials also use SF_6 as a process gas [101, 107, 108, 176, 215], meaning the issue is not limited to this specific recipe. Future work should investigate the use of alternatives to reduce the potential environmental effects of this and similar processes.

In addition, this work provides useful information for the use of ALE for device fabrication. First, the importance of proper preconditioning in ALE recipes when

deployed in shared user spaces cannot be understated. Improper chamber condition was found to convert this highly reliable etch process into a deposition process simply due to the presence of a niobium-containing coating on the walls. Second, process optimizations can significantly change the contamination from ALE precursors even when the overall chemistry in use is nearly identical. It is currently unknown what effect Al and F have on SiO_2 devices, but in the event they are significantly deleterious, the use of other precursors should be evaluated such as dimethylaluminum chloride and other fluorine-containing gases. Lastly, ALE etch rates in literature should be taken as rough guides only; the method used to fabricate thin films has significant implications on their etch rate. A careful investigation into this last point could also be the subject of further work, through correlating deposition parameters for sputtered and PECVD SiO_2 to their etch rate, along with an analysis of the underlying material structure.

Thermal laser evaporation

In the last few years major strides have been made in the development of TLE by the Max Planck Institute and spin-off company epiray GmbH. This work represents the first independent implementation of the technique since its revival in the 21st century. In addition, we give the first detailed characterization of non-epitaxial TLE films. Along with prior works, our findings indicate that the technique is equally, if not more capable than other evaporative PVD techniques, and therefore we conclude that TLE is a promising new avenue for thin film growth. However, there remain key technical challenges and much work to be done:

1. Coating of the optical elements must be eliminated if at all possible. There are currently means to decrease this but not entirely prevent it. It may be useful to consult PLD system design for inspiration, as PLD must contend with the same problem while having many more decades of development.

2. The characterization of more films should be performed, specifically focusing on areas that could be improved on from other PVD techniques. For instance, film crystallinity, purity, or electrical properties of materials where these are significant figures of merit.

3. Beyond the recent development of fiber lasers, other laser technologies have seen significant advances in the last few decades. While excimer lasers (UV) feature the highest absorption by most elements, they remain relatively

expensive. Lasers in visible wavelengths are an interesting middle ground between the UV and IR lasers, now achieving multiple kW powers, feature higher absorption by most elements compared to fiber lasers, and are priced more affordably than excimer lasers.

4. There may be means of enhancing evaporation efficiency at the target through increasing free-carrier absorption. For instance, by using a low-power laser with a targeted wavelength to stimulate interband transitions. This would allow for the use of much lower power lasers, increasing safety, efficiency, and decreasing costs.

5. While TLE has many minor advantages over traditional PVD technologies, the major difference lies in the crucible-free nature of evaporation, allowing for refractory metal deposition. Therefore, the most scientifically interesting avenue of future work is the exploration of refractory metal compounds which have been exceedingly difficult to fabricate to-date. This is the focus of ongoing work.

BIBLIOGRAPHY

[1] Herbert B. Callen and Theodore A. Welton. Irreversibility and generalized noise. *Phys. Rev.*, 83:34–40, Jul 1951. doi: 10.1103/PhysRev.83.34. URL https://link.aps.org/doi/10.1103/PhysRev.83.34.

[2] Ryogo Kubo. Statistical-mechanical theory of irreversible processes. i. general theory and simple applications to magnetic and conduction problems. *Journal of the Physical Society of Japan*, 12(6):570–586, 1957. doi: 10.1143/JPSJ.12.570. URL https://doi.org/10.1143/JPSJ.12.570.

[3] K. J. Schmidt-Tiedemann. Tensor theory of the conductivity of warm electrons in cubic semiconductors. *Philips Res. Repts.*, 18:338–360, 1963.

[4] Lino Reggiani. *General Theory*, pages 7–86. Springer Berlin Heidelberg, Berlin, Heidelberg, 1985. ISBN 978-3-540-38849-4. doi: 10.1007/3-540-13321-6_2. URL https://doi.org/10.1007/3-540-13321-6_2.

[5] J. P. Nougier. Noise and diffusion of hot carriers. In David K. Ferry, J. R. Barker, and C. Jacoboni, editors, *Physics of Nonlinear Transport in Semiconductors*, volume 52 of *NATO advanced study institutes series: Series B, Physics*, pages 415–465, New York, 1980. Plenum Press.

[6] Carlo Jacoboni and Lino Reggiani. Bulk hot-electron properties of cubic semiconductors. *Advances in Physics*, 28(4):493–553, 1979. doi: 10.1080/00018737900101405. URL https://doi.org/10.1080/00018737900101405.

[7] G. Ottaviani, L. Reggiani, C. Canali, F. Nava, and A. Alberigi-Quaranta. Hole drift velocity in silicon. *Phys. Rev. B*, 12:3318–3329, Oct 1975. doi: 10.1103/PhysRevB.12.3318. URL https://link.aps.org/doi/10.1103/PhysRevB.12.3318.

[8] C. Canali, C. Jacoboni, F. Nava, G. Ottaviani, and A. Alberigi-Quaranta. Electron drift velocity in silicon. *Phys. Rev. B*, 12:2265–2284, Sep 1975. doi: 10.1103/PhysRevB.12.2265. URL https://link.aps.org/doi/10.1103/PhysRevB.12.2265.

[9] Melvin Lax. Fluctuations from the nonequilibrium steady state. *Rev. Mod. Phys.*, 32:25–64, Jan 1960. doi: 10.1103/RevModPhys.32.25. URL https://link.aps.org/doi/10.1103/RevModPhys.32.25.

[10] E. Conwell. *High Field Transport in Semiconductors*. Academic Press, New York, 1967.

[11] L. Reggiani, editor. *Hot-Electron Transport in Semiconductors*. Springer-Verlag, 1985.

[12] H. L. Hartnagel, R. Katilius, and A. Matulionis. *Microwave Noise in Semiconductor Devices*. John Wiley & Sons, Inc., 2001.

[13] S.M. Sze and Kwok K. Ng. *Physics of Semiconductor Devices*. Wiley, 3 edition, 2007.

[14] Mark Lundstrom. *Fundamentals of carrier transport*. Cambridge University Press, 2 edition, 2000.

[15] David Ferry. *Semiconductor Transport*. CRC Press, 2000.

[16] Samuel Poncé, Wenbin Li, Sven Reichardt, and Feliciano Giustino. First-principles calculations of charge carrier mobility and conductivity in bulk semiconductors and two-dimensional materials. *Reports on Progress in Physics*, 83(3):036501, feb 2020. doi: 10.1088/1361-6633/ab6a43. URL https://doi.org/10.1088/1361-6633/ab6a43.

[17] Marco Bernardi. First-principles dynamics of electrons and phonons*. *The European Physical Journal B*, 89(11):239, Nov 2016. ISSN 1434-6036. doi: 10.1140/epjb/e2016-70399-4. URL https://doi.org/10.1140/epjb/e2016-70399-4.

[18] Feliciano Giustino. Electron-phonon interactions from first principles. *Rev. Mod. Phys.*, 89:015003, Feb 2017. doi: 10.1103/RevModPhys.89.015003. URL https://link.aps.org/doi/10.1103/RevModPhys.89.015003.

[19] Søren Smidstrup, Troels Markussen, Pieter Vancraeyveld, Jess Wellendorff, Julian Schneider, Tue Gunst, Brecht Verstichel, Daniele Stradi, Petr A Khomyakov, Ulrik G Vej-Hansen, Maeng-Eun Lee, Samuel T Chill, Filip Rasmussen, Gabriele Penazzi, Fabiano Corsetti, Ari Ojanperä, Kristian Jensen, Mattias L N Palsgaard, Umberto Martinez, Anders Blom, Mads Brandbyge, and Kurt Stokbro. QuantumATK: an integrated platform of electronic and atomic-scale modelling tools. *Journal of Physics: Condensed Matter*, 32(1):015901, oct 2019. doi: 10.1088/1361-648x/ab4007. URL https://doi.org/10.1088/1361-648x/ab4007.

[20] S. Poncé, E.R. Margine, C. Verdi, and F. Giustino. Epw: Electron–phonon coupling, transport and superconducting properties using maximally localized wannier functions. *Computer Physics Communications*, 209:116–133, 2016. ISSN 0010-4655. doi: https://doi.org/10.1016/j.cpc.2016.07.028. URL https://www.sciencedirect.com/science/article/pii/S0010465516302260.

[21] Aldo H. Romero, Douglas C. Allan, Bernard Amadon, Gabriel Antonius, Thomas Applencourt, Lucas Baguet, Jordan Bieder, François Bottin, Johann Bouchet, Eric Bousquet, Fabien Bruneval, Guillaume Brunin, Damien Caliste, Michel Côté, Jules Denier, Cyrus Dreyer, Philippe Ghosez, Matteo Giantomassi, Yannick Gillet, Olivier Gingras, Donald R. Hamann, Geoffroy

Hautier, François Jollet, Gérald Jomard, Alexandre Martin, Henrique P. C. Miranda, Francesco Naccarato, Guido Petretto, Nicholas A. Pike, Valentin Planes, Sergei Prokhorenko, Tonatiuh Rangel, Fabio Ricci, Gian-Marco Rignanese, Miquel Royo, Massimiliano Stengel, Marc Torrent, Michiel J. van Setten, Benoit Van Troeye, Matthieu J. Verstraete, Julia Wiktor, Josef W. Zwanziger, and Xavier Gonze. Abinit: Overview and focus on selected capabilities. *The Journal of Chemical Physics*, 152(12):124102, 2020. doi: 10.1063/1.5144261. URL https://doi.org/10.1063/1.5144261.

[22] Jin-Jian Zhou, Jinsoo Park, I-Te Lu, Ivan Maliyov, Xiao Tong, and Marco Bernardi. Perturbo: A software package for ab initio electron–phonon interactions, charge transport and ultrafast dynamics. *Comput. Phys. Commun.*, 264:107970, 2021. ISSN 0010-4655. doi: https://doi.org/10.1016/j.cpc.2021.107970. URL https://www.sciencedirect.com/science/article/pii/S0010465521000837.

[23] Nakib H. Protik, Chunhua Li, Miguel Pruneda, David Broido, and Pablo Ordejón. The elphbolt ab initio solver for the coupled electron-phonon boltzmann transport equations. *npj Computational Materials*, 8(1):28, Feb 2022. ISSN 2057-3960. doi: 10.1038/s41524-022-00710-0. URL https://doi.org/10.1038/s41524-022-00710-0.

[24] Wu Li. Electrical transport limited by electron-phonon coupling from boltzmann transport equation: An ab initio study of si, al, and mos_2. *Phys. Rev. B*, 92:075405, Aug 2015. doi: 10.1103/PhysRevB.92.075405. URL https://link.aps.org/doi/10.1103/PhysRevB.92.075405.

[25] Mattia Fiorentini and Nicola Bonini. Thermoelectric coefficients of n-doped silicon from first principles via the solution of the boltzmann transport equation. *Phys. Rev. B*, 94:085204, Aug 2016. doi: 10.1103/PhysRevB.94.085204. URL https://link.aps.org/doi/10.1103/PhysRevB.94.085204.

[26] Samuel Poncé, Francesco Macheda, Elena Roxana Margine, Nicola Marzari, Nicola Bonini, and Feliciano Giustino. First-principles predictions of hall and drift mobilities in semiconductors. *Phys. Rev. Research*, 3:043022, Oct 2021. doi: 10.1103/PhysRevResearch.3.043022. URL https://link.aps.org/doi/10.1103/PhysRevResearch.3.043022.

[27] Jin-Jian Zhou and Marco Bernardi. Ab initio electron mobility and polar phonon scattering in gaas. *Phys. Rev. B*, 94:201201, Nov 2016. doi: 10.1103/PhysRevB.94.201201. URL https://link.aps.org/doi/10.1103/PhysRevB.94.201201.

[28] Te-Huan Liu, Jiawei Zhou, Bolin Liao, David J. Singh, and Gang Chen. First-principles mode-by-mode analysis for electron-phonon scattering channels and mean free path spectra in gaas. *Phys. Rev. B*, 95:075206, Feb 2017. doi: 10.1103/PhysRevB.95.075206. URL https://link.aps.org/doi/10.1103/PhysRevB.95.075206.

[29] Cheol-Hwan Park, Nicola Bonini, Thibault Sohier, Georgy Samsonidze, Boris Kozinsky, Matteo Calandra, Francesco Mauri, and Nicola Marzari. Electron–phonon interactions and the intrinsic electrical resistivity of graphene. *Nano Letters*, 14(3):1113–1119, 2014. doi: 10.1021/nl402696q. URL https://doi.org/10.1021/nl402696q.

[30] K. M. Borysenko, J. T. Mullen, E. A. Barry, S. Paul, Y. G. Semenov, J. M. Zavada, M. Buongiorno Nardelli, and K. W. Kim. First-principles analysis of electron-phonon interactions in graphene. *Phys. Rev. B*, 81:121412, Mar 2010. doi: 10.1103/PhysRevB.81.121412. URL https://link.aps.org/doi/10.1103/PhysRevB.81.121412.

[31] Tue Gunst, Troels Markussen, Kurt Stokbro, and Mads Brandbyge. First-principles method for electron-phonon coupling and electron mobility: Applications to two-dimensional materials. *Phys. Rev. B*, 93:035414, Jan 2016. doi: 10.1103/PhysRevB.93.035414. URL https://link.aps.org/doi/10.1103/PhysRevB.93.035414.

[32] Oscar D Restrepo, Kevin E Krymowski, Joshua Goldberger, and Wolfgang Windl. A first principles method to simulate electron mobilities in 2d materials. *New Journal of Physics*, 16(10):105009, oct 2014. doi: 10.1088/1367-2630/16/10/105009. URL https://doi.org/10.1088/1367-2630/16/10/105009.

[33] Kristen Kaasbjerg, Kristian S. Thygesen, and Karsten W. Jacobsen. Phonon-limited mobility in n-type single-layer mos_2 from first principles. *Phys. Rev. B*, 85:115317, Mar 2012. doi: 10.1103/PhysRevB.85.115317. URL https://link.aps.org/doi/10.1103/PhysRevB.85.115317.

[34] Thibault Sohier, Davide Campi, Nicola Marzari, and Marco Gibertini. Mobility of two-dimensional materials from first principles in an accurate and automated framework. *Phys. Rev. Materials*, 2:114010, Nov 2018. doi: 10.1103/PhysRevMaterials.2.114010. URL https://link.aps.org/doi/10.1103/PhysRevMaterials.2.114010.

[35] Nien-En Lee, Jin-Jian Zhou, Hsiao-Yi Chen, and Marco Bernardi. Ab initio electron-two-phonon scattering in gaas from next-to-leading order perturbation theory. *Nature Communications*, 11(1):1607, Mar 2020. ISSN 2041-1723. doi: 10.1038/s41467-020-15339-0. URL https://doi.org/10.1038/s41467-020-15339-0.

[36] I-Te Lu, Jinsoo Park, Jin-Jian Zhou, and Marco Bernardi. Ab initio electron-defect interactions using wannier functions. *npj Computational Materials*, 6 (1):17, Mar 2020. ISSN 2057-3960. doi: 10.1038/s41524-020-0284-y. URL https://doi.org/10.1038/s41524-020-0284-y.

[37] I-Te Lu, Jin-Jian Zhou, Jinsoo Park, and Marco Bernardi. First-principles ionized-impurity scattering and charge transport in doped materials. *Phys. Rev. Materials*, 6:L010801, Jan 2022. doi: 10.1103/PhysRevMaterials.6.L010801. URL https://link.aps.org/doi/10.1103/PhysRevMaterials.6.L010801.

[38] Jinsoo Park, Jin-Jian Zhou, Vatsal A. Jhalani, Cyrus E. Dreyer, and Marco Bernardi. Long-range quadrupole electron-phonon interaction from first principles. *Phys. Rev. B*, 102:125203, Sep 2020. doi: 10.1103/PhysRevB.102.125203. URL https://link.aps.org/doi/10.1103/PhysRevB.102.125203.

[39] Guillaume Brunin, Henrique Pereira Coutada Miranda, Matteo Giantomassi, Miquel Royo, Massimiliano Stengel, Matthieu J. Verstraete, Xavier Gonze, Gian-Marco Rignanese, and Geoffroy Hautier. Phonon-limited electron mobility in si, gaas, and gap with exact treatment of dynamical quadrupoles. *Phys. Rev. B*, 102:094308, Sep 2020. doi: 10.1103/PhysRevB.102.094308. URL https://link.aps.org/doi/10.1103/PhysRevB.102.094308.

[40] Dhruv C. Desai, Bahdan Zviazhynski, Jin-Jian Zhou, and Marco Bernardi. Magnetotransport in semiconductors and two-dimensional materials from first principles. *Phys. Rev. B*, 103:L161103, Apr 2021. doi: 10.1103/PhysRevB.103.L161103. URL https://link.aps.org/doi/10.1103/PhysRevB.103.L161103.

[41] Vatsal A. Jhalani, Jin-Jian Zhou, Jinsoo Park, Cyrus E. Dreyer, and Marco Bernardi. Piezoelectric electron-phonon interaction from ab initio dynamical quadrupoles: Impact on charge transport in wurtzite gan. *Phys. Rev. Lett.*, 125:136602, Sep 2020. doi: 10.1103/PhysRevLett.125.136602. URL https://link.aps.org/doi/10.1103/PhysRevLett.125.136602.

[42] E. J. Ryder and W. Shockley. Mobilities of electrons in high electric fields. *Phys. Rev.*, 81:139–140, Jan 1951. doi: 10.1103/PhysRev.81.139.2. URL https://link.aps.org/doi/10.1103/PhysRev.81.139.2.

[43] E. J. Ryder. Mobility of holes and electrons in high electric fields. *Phys. Rev.*, 90:766–769, Jun 1953. doi: 10.1103/PhysRev.90.766. URL https://link.aps.org/doi/10.1103/PhysRev.90.766.

[44] W. Shockley. Hot electrons in germanium and ohm's law. *Bell System Tech. J.*, 30:990–1034, 1951.

[45] J. Zucker, V. J. Fowler, and E. M. Conwell. High-field conductivity in germanium and silicon at microwave frequencies. *Journal of Applied Physics*, 32(12):2606–2611, 1961. doi: 10.1063/1.1728360. URL https://doi.org/10.1063/1.1728360.

[46] C.B. Norris and J.F. Gibbons. Measurement of high-field carrier drift velocities in silicon by a time-of-flight technique. *IEEE Transactions on Electron Devices*, 14(1):38–43, 1967. doi: 10.1109/T-ED.1967.15893.

[47] C. Canali, G. Ottaviani, and G. Majni. Hot hole anisotropic effect in silicon and germanium. *Solid State Commun.*, 15(7):1213–1216, 1974. ISSN 0038-1098. doi: https://doi.org/10.1016/0038-1098(74)90053-2. URL https://www.sciencedirect.com/science/article/pii/0038109874900532.

[48] Lino Reggiani, Rossella Brunetti, and Edmundas Normantas. Diffusion coefficient of holes in silicon by monte carlo simulation. *J. Appl. Phys.*, 59(4): 1212–1215, 1986. doi: 10.1063/1.336507. URL https://doi.org/10.1063/1.336507.

[49] T. W. Sigmon and J. F. Gibbons. Diffusivity of electrons and holes in silicon. *Applied Physics Letters*, 15(10):320–322, 1969. doi: 10.1063/1.1652842. URL https://doi.org/10.1063/1.1652842.

[50] F. Nava, C. Canali, L. Reggiani, D. Gasquet, J. C. Vaissiere, and J. P. Nougier. On the diffusivity of holes in silicon. *J. Appl. Phys.*, 50(2):922–924, 1979. doi: 10.1063/1.326012. URL https://doi.org/10.1063/1.326012.

[51] R. Brunetti, C. Jacoboni, F. Nava, L. Reggiani, G. Bosman, and R. J. J. Zijlstra. Diffusion coefficient of electrons in silicon. *Journal of Applied Physics*, 52(11):6713–6722, 1981. doi: 10.1063/1.328622. URL https://doi.org/10.1063/1.328622.

[52] E. Erlbach and J. B. Gunn. Noise temperature of hot electrons in germanium. *Phys. Rev. Lett.*, 8:280–282, Apr 1962. doi: 10.1103/PhysRevLett.8.280. URL https://link.aps.org/doi/10.1103/PhysRevLett.8.280.

[53] J. P. Nougier and M. Rolland. Mobility, noise temperature, and diffusivity of hot holes in germanium. *Phys. Rev. B*, 8:5728–5737, Dec 1973. doi: 10.1103/PhysRevB.8.5728. URL https://link.aps.org/doi/10.1103/PhysRevB.8.5728.

[54] V. Bareikis, R. Barkauskas, A. Galdikas, and R. Katilius. Ambipolar diffusion of hot charge carriers and noise in semiconductors. *Sov. Phys. Semicond.*, 14 (9):1046–1051, 1980.

[55] D. Gasquet, B. Azais, J. C. Vaissiere, and J. P. Nougier. Generation recombination noise in p-si at 77 k. In A. d'Amico and P. Mazzetti, editors, *Noise in Physical Systems and 1/f Noise - 1985*, pages 231–233. Elsevier, 1986.

[56] S. V. Gantsevich, V. L. Gurevich, and R. Katilius. Theory of fluctuations in nonequilibrium electron gas. *La Rivista del Nuovo Cimento*, 2(5):1–88, 1979. doi: 10.1007/BF02724353. URL https://doi.org/10.1007/BF02724353.

[57] M. Asche, J. von Borzeszkowski, and O. G. Sarbei. Conductivity of hot holes in silicon at 77 °k. *Phys. Status Solidi B*, 38(1):357–362, 1970. doi: https://doi.org/10.1002/pssb.19700380135. URL https://onlinelibrary.wiley.com/doi/abs/10.1002/pssb.19700380135.

[58] C. Canali, G. Ottaviani, and A. Alberigi-Quaranta. Drift velocity of electrons and holes and associated anisotropic effects in silicon. *J. Phys. Chem. Solids*, 32(8):1707–1720, 1971. ISSN 0022-3697. doi: https://doi.org/10.1016/S0022-3697(71)80137-3. URL https://www.sciencedirect.com/science/article/pii/S0022369771801373.

[59] G.R. Tschulena. Impurity scattering of warm holes in germanium and silicon. *J. Phys. Chem. Solids*, 33(6):1219–1224, 1972. ISSN 0022-3697. doi: https://doi.org/10.1016/S0022-3697(72)80159-8. URL https://www.sciencedirect.com/science/article/pii/S0022369772801598.

[60] Carlo Jacoboni and Lino Reggiani. The monte carlo method for the solution of charge transport in semiconductors with applications to covalent materials. *Rev. Mod. Phys.*, 55:645–705, Jul 1983. doi: 10.1103/RevModPhys.55.645. URL https://link.aps.org/doi/10.1103/RevModPhys.55.645.

[61] J.-P. Nougier. Fluctuations and noise of hot carriers in semiconductor materials and devices. *IEEE Transactions on Electron Devices*, 41(11):2034–2049, 1994. doi: 10.1109/16.333821.

[62] L Reggiani, E Starikov, P Shiktorov, V Gruzinskis, and L Varani. Modelling of small-signal response and electronic noise in semiconductor high-field transport. *Semiconductor Science and Technology*, 12(2):141–156, feb 1997. doi: 10.1088/0268-1242/12/2/001. URL https://doi.org/10.1088/0268-1242/12/2/001.

[63] M.V. Fischetti. Monte carlo simulation of transport in technologically significant semiconductors of the diamond and zinc-blende structures. i. homogeneous transport. *IEEE Transactions on Electron Devices*, 38(3):634–649, 1991. doi: 10.1109/16.75176.

[64] Jim Dewey and M. A. Osman. Monte carlo study of hole transport in silicon. *Journal of Applied Physics*, 74(5):3219–3223, 1993. doi: 10.1063/1.354595. URL https://doi.org/10.1063/1.354595.

[65] S. Rodríguez-Bolívar, F. M. Gómez-Campos, F. Gámiz, and J. E. Carceller. Implications of nonparabolicity, warping, and inelastic phonon scattering on hole transport in pure si and ge within the effective mass framework. *Journal of Applied Physics*, 97(1):013702, 2005. doi: 10.1063/1.1823025. URL https://doi.org/10.1063/1.1823025.

[66] Caroline Dos Santos Soares. Ensemble monte carlo simulation of hole transport in si, ge, and sige alloys. Master's thesis, Universidade Federal Do Rio Grande Do Sul, 2020.

[67] L. Reggiani, P. Golinelli, L. Varani, T. González, D. Pardo, E. Starikov, P. Shiktorov, and V. Gružinskis. Monte carlo analysis of electronic noise in semiconductor materials and devices. *Microelectr. J.*, 28(2):183–198, 1997. ISSN 0026-2692. doi: https://doi.org/10.1016/S0026-2692(96)00061-4. URL https://www.sciencedirect.com/science/article/pii/S0026269296000614.

[68] C. Jacoboni and P. Lugli. *The Monte Carlo Method for Semiconductor Device Simulation*. Springer Vienna, 1 edition, 1989. ISBN 978-3-211-82110-7.

[69] J. Mateos, T. Gonzalez, D. Pardo, V. Hoel, and A. Cappy. Monte carlo simulator for the design optimization of low-noise hemts. *IEEE Transactions on Electron Devices*, 47(10):1950–1956, 2000. doi: 10.1109/16.870579.

[70] Karl Hess, editor. *Monte Carlo Device Simulation: Full Band and Beyond*, volume 144 of *The Springer International Series in Engineering and Computer Science*. Springer Science + Business Media, LLC, 1991. ISBN 978-1-4615-4026-7.

[71] Paul Yoder. *First Principles Monte Carlo Simulation of Charge Transport in Semiconductors*. PhD thesis, University of Illinois at Urbana-Champaign, 1994.

[72] H. Shichijo and K. Hess. Band-structure-dependent transport and impact ionization in gaas. *Phys. Rev. B*, 23:4197–4207, Apr 1981. doi: 10.1103/PhysRevB.23.4197. URL https://link.aps.org/doi/10.1103/PhysRevB.23.4197.

[73] C. Jungemann, S. Keith, M. Bartels, and B. Meinerzhagen. Efficient full-band monte carlo simulation of silicon devices. *IEICE Transactions on Electronics*, E82-C:870–879, 1999.

[74] Niels Fitzer, Angelika Kuligk, Ronald Redmer, Martin Städele, Stephen M. Goodnick, and Wolfgang Schattke. Full-band monte carlo simulations of high-field electron transport in gaas and zns. *Phys. Rev. B*, 67:201201, May 2003. doi: 10.1103/PhysRevB.67.201201. URL https://link.aps.org/doi/10.1103/PhysRevB.67.201201.

[75] J Bude and R Kent Smith. Phase-space simplex monte carlo for semiconductor transport. *Semiconductor Science and Technology*, 9(5S):840–843, may 1994. doi: 10.1088/0268-1242/9/5s/119. URL https://doi.org/10.1088/0268-1242/9/5s/119.

[76] M V. Fischetti, N. Sano, S. E. Laux, and K. Natori. Full-band-structure theory of high-field transport and impact ionization of electrons and holes in ge, si, and gaas. *Journal of Technology Computer Aided Design TCAD*, pages 1–50, 1996. doi: 10.1109/TCAD.1996.6449160.

[77] S. Jallepalli, M. Rashed, W.-K. Shih, C. M. Maziar, and A. F. Tasch. A full-band monte carlo model for hole transport in silicon. *Journal of Applied Physics*, 81(5):2250–2255, 1997. doi: 10.1063/1.364287. URL https://doi.org/10.1063/1.364287.

[78] F. M. Bufler, P. Graf, and B. Meinerzhagen. High-field hole transport in strained si and sige by monte carlo simulation: Full band versus analytic band models. *VLSI Design*, 8(065181):41–45, 1998. ISSN 1065-514X. doi: 10.1155/1998/65181. URL https://doi.org/10.1155/1998/65181.

[79] Björn Fischer and Karl R. Hofmann. A full-band monte carlo model for the temperature dependence of electron and hole transport in silicon. *Applied Physics Letters*, 76(5):583–585, 2000. doi: 10.1063/1.125824. URL https://doi.org/10.1063/1.125824.

[80] Phuong Hoa Nguyen, Karl R. Hofmann, and Gernot Paasch. Comparative full-band monte carlo study of si and ge with screened pseudopotential-based phonon scattering rates. *Journal of Applied Physics*, 94(1):375–386, 2003. doi: 10.1063/1.1579860. URL https://doi.org/10.1063/1.1579860.

[81] Zhen Li, Patrizio Graziosi, and Neophytos Neophytou. Deformation potential extraction and computationally efficient mobility calculations in silicon from first principles. *Phys. Rev. B*, 104:195201, Nov 2021. doi: 10.1103/PhysRevB.104.195201. URL https://link.aps.org/doi/10.1103/PhysRevB.104.195201.

[82] Jinlong Ma, Arun S. Nissimagoudar, and Wu Li. First-principles study of electron and hole mobilities of si and gaas. *Phys. Rev. B*, 97:045201, Jan 2018. doi: 10.1103/PhysRevB.97.045201. URL https://link.aps.org/doi/10.1103/PhysRevB.97.045201.

[83] Samuel Poncé, Elena R. Margine, and Feliciano Giustino. Towards predictive many-body calculations of phonon-limited carrier mobilities in semiconductors. *Phys. Rev. B*, 97:121201, Mar 2018. doi: 10.1103/PhysRevB.97.121201. URL https://link.aps.org/doi/10.1103/PhysRevB.97.121201.

[84] Alexander Y. Choi, Peishi S. Cheng, Benjamin Hatanpää, and Austin J. Minnich. Electronic noise of warm electrons in semiconductors from first principles. *Phys. Rev. Materials*, 5:044603, Apr 2021. doi: 10.1103/PhysRevMaterials.5.044603. URL https://link.aps.org/doi/10.1103/PhysRevMaterials.5.044603.

[85] Peishi S. Cheng, Jiace Sun, Shi-Ning Sun, Alexander Y. Choi, and Austin J. Minnich. High-field transport and hot-electron noise in gaas from first-principles calculations: Role of two-phonon scattering. *Phys. Rev. B*, 106:245201, Dec 2022. doi: 10.1103/PhysRevB.106.245201. URL https://link.aps.org/doi/10.1103/PhysRevB.106.245201.

[86] Benjamin Hatanpää, Alexander Y. Choi, Peishi S. Cheng, and Austin J. Minnich. Two-phonon scattering in nonpolar semiconductors: A first-principles study of warm electron transport in si. *Phys. Rev. B*, 107: L041110, Jan 2023. doi: 10.1103/PhysRevB.107.L041110. URL https://link.aps.org/doi/10.1103/PhysRevB.107.L041110.

[87] Benjamin Hatanpää and Austin J. Minnich. Hot electron diffusion, microwave noise, and piezoresistivity in si from first principles. *Phys. Rev. B*, 109: 235201, Jun 2024. doi: 10.1103/PhysRevB.109.235201. URL https://link.aps.org/doi/10.1103/PhysRevB.109.235201.

[88] Ivan Maliyov, Jinsoo Park, and Marco Bernardi. Ab initio electron dynamics in high electric fields: Accurate prediction of velocity-field curves. *Phys. Rev. B*, 104:L100303, Sep 2021. doi: 10.1103/PhysRevB.104.L100303. URL https://link.aps.org/doi/10.1103/PhysRevB.104.L100303.

[89] L. Reggiani. High-field transport of holes in elemental semiconductors. In David K. Ferry, J. R. Barker, and C. Jacoboni, editors, *Physics of Nonlinear Transport in Semiconductors*, volume 52 of *NATO advanced study institutes series: Series B, Physics*, pages 467–477, New York, 1980. Plenum Press.

[90] C. Jacoboni. An introduction to nonlinear transport in semiconductors. In David K. Ferry, J. R. Barker, and C. Jacoboni, editors, *Physics of Nonlinear Transport in Semiconductors*, volume 52 of *NATO advanced study institutes series: Series B, Physics*, pages xiii–xx, New York, 1980. Plenum Press.

[91] Te-Huan Liu, Bai Song, Laureen Meroueh, Zhiwei Ding, Qichen Song, Jiawei Zhou, Mingda Li, and Gang Chen. Simultaneously high electron and hole mobilities in cubic boron-v compounds: Bp, bas, and bsb. *Phys. Rev. B*, 98: 081203(R), Aug 2018. doi: 10.1103/PhysRevB.98.081203. URL https://link.aps.org/doi/10.1103/PhysRevB.98.081203.

[92] Jungwoo Shin, Geethal Amila Gamage, Zhiwei Ding, Ke Chen, Fei Tian, Xin Qian, Jiawei Zhou, Hwijong Lee, Jianshi Zhou, Li Shi, Thanh Nguyen, Fei Han, Mingda Li, David Broido, Aaron Schmidt, Zhifeng Ren, and Gang Chen. High ambipolar mobility in cubic boron arsenide. *Science*, 377(6604):437–440, 2022. doi: 10.1126/science.abn4290. URL https://www.science.org/doi/abs/10.1126/science.abn4290.

[93] Shuai Yue, Fei Tian, Xinyu Sui, Mohammadjavad Mohebinia, Xianxin Wu, Tian Tong, Zhiming Wang, Bo Wu, Qing Zhang, Zhifeng Ren, Jiming Bao, and Xinfeng Liu. High ambipolar mobility in cubic boron arsenide revealed by transient reflectivity microscopy. *Science*, 377(6604):433–436, 2022. doi: 10.1126/science.abn4727. URL https://www.science.org/doi/abs/10.1126/science.abn4727.

[94] Richard C. Jaeger. *Introduction to Microelectronic Fabrication*. Prentice Hall, 2 edition, 2002.

[95] Sami Franssila. *Introduction to Microfabrication*. Wiley, 2 edition, 2010.

[96] Gottlieb S. Oehrlein, Stephan M. Brandstadter, Robert L. Bruce, Jane P. Chang, Jessica C. DeMott, Vincent M. Donnelly, Rémi Dussart, Andreas Fischer, Richard A. Gottscho, Satoshi Hamaguchi, Masanobu Honda, Masaru Hori, Kenji Ishikawa, Steven G. Jaloviar, Keren J. Kanarik, Kazuhiro Karahashi, Akiteru Ko, Hiten Kothari, Nobuyuki Kuboi, Mark J. Kushner, Thorsten Lill, Pingshan Luan, Ali Mesbah, Eric Miller, Shoubhanik Nath, Yoshinobu Ohya, Mitsuhiro Omura, Chanhoon Park, John Poulose, Shahid Rauf, Makoto Sekine, Taylor G. Smith, Nathan Stafford, Theo Standaert, and Peter L. G. Ventzek. Future of plasma etching for microelectronics: Challenges and opportunities. *Journal of Vacuum Science & Technology B*, 42(4):041501, 06 2024. ISSN 2166-2746. doi: 10.1116/6.0003579. URL https://doi.org/10.1116/6.0003579.

[97] H. F. Winters and J. W. Coburn. The etching of silicon with xef2 vapor. *Applied Physics Letters*, 34(1):70–73, 01 1979. ISSN 0003-6951. doi: 10.1063/1.90562. URL https://doi.org/10.1063/1.90562.

[98] Thorsten Lill. *Atomic Layer Processing: Semiconductor Dry Etching Technology*, chapter 4. Wiley, 2021.

[99] Shashank C. Deshmukh and Demetre J. Economou. Remote plasma etching reactors: Modeling and experiment. *Journal of Vacuum Science & Technology B: Microelectronics and Nanometer Structures Processing, Measurement, and Phenomena*, 11(2):206–215, 03 1993. ISSN 1071-1023. doi: 10.1116/1.586704. URL https://doi.org/10.1116/1.586704.

[100] Franz Laermer, Sami Franssila, Lauri Sainiemi, and Kai Kolari. Chapter 16 - deep reactive ion etching. In Markku Tilli, Mervi Paulasto-Krockel, Matthias Petzold, Horst Theuss, Teruaki Motooka, and Veikko Lindroos, editors, *Handbook of Silicon Based MEMS Materials and Technologies (Third Edition)*, Micro and Nano Technologies, pages 417–446. Elsevier, third edition edition, 2020. ISBN 978-0-12-817786-0. doi: https://doi.org/10.1016/B978-0-12-817786-0.00016-5. URL https://www.sciencedirect.com/science/article/pii/B9780128177860000165.

[101] Ivy I. Chen, Jennifer Solgaard, Ryoto Sekine, Azmain A. Hossain, Anthony Ardizzi, David S. Catherall, Alireza Marandi, James R. Renzas, Frank Greer, and Austin J. Minnich. Isotropic atomic layer etching of mgo-doped lithium niobate using sequential exposures of h2 and sf6/ar plasmas. *Journal of Vacuum Science & Technology A*, 42(6):062603, 10 2024. ISSN 0734-2101. doi: 10.1116/6.0003962. URL https://doi.org/10.1116/6.0003962.

[102] Ivy I. Chen, Mariya Ezzy, Emily Hsue-Chi Shi, Clifford F. Frez, Suraj, Lin Yi, Mahmood Bagheri, James R. Renzas, Alireza Marandi, Frank Greer, and Austin J. Minnich. Directional atomic layer etching of mgo-doped lithium

niobate using br-based plasma. *Journal of Vacuum Science & Technology A*, 44(2):022606, 01 2026. ISSN 0734-2101. doi: 10.1116/6.0005127. URL https://doi.org/10.1116/6.0005127.

[103] Nathan Marchack, Marwan Khater, Jason Orcutt, Josephine Chang, Steven Holmes, Tymon Barwicz, Swetha Kamlapurkar, William Green, and Sebastian Engelmann. Reducing Line Edge Roughness in Si and SiN through plasma etch chemistry optimization for photonic waveguide applications. In Sebastian U. Engelmann, editor, *Advanced Etch Technology for Nanopatterning VI*, volume 10149, page 101490F. International Society for Optics and Photonics, SPIE, 2017. doi: 10.1117/12.2258112. URL https://doi.org/10.1117/12.2258112.

[104] Xingchen Ji, Felippe A. S. Barbosa, Samantha P. Roberts, Avik Dutt, Jaime Cardenas, Yoshitomo Okawachi, Alex Bryant, Alexander L. Gaeta, and Michal Lipson. Ultra-low-loss on-chip resonators with sub-milliwatt parametric oscillation threshold. *Optica*, 4(6):619–624, Jun 2017. doi: 10.1364/OPTICA.4.000619. URL https://opg.optica.org/optica/abstract.cfm?URI=optica-4-6-619.

[105] Yu Zhang, Xian Xiao, Kaiqi Zhang, Siwei Li, Anirban Samanta, Yichi Zhang, Kuanping Shang, Roberto Proietti, Katsunari Okamoto, and S. J. Ben Yoo. Foundry-enabled scalable all-to-all optical interconnects using silicon nitride arrayed waveguide router interposers and silicon photonic transceivers. *IEEE Journal of Selected Topics in Quantum Electronics*, 25(5):1–9, 2019. doi: 10.1109/JSTQE.2019.2910415.

[106] Xingchen Ji, Samantha Roberts, Mateus Corato-Zanarella, and Michal Lipson. Methods to achieve ultra-high quality factor silicon nitride resonators. *APL Photonics*, 6(7):071101, 07 2021. ISSN 2378-0967. doi: 10.1063/5.0057881. URL https://doi.org/10.1063/5.0057881.

[107] Azmain A. Hossain, Haozhe Wang, David S. Catherall, Martin Leung, Harm C. M. Knoops, James R. Renzas, and Austin J. Minnich. Isotropic plasma-thermal atomic layer etching of superconducting titanium nitride films using sequential exposures of molecular oxygen and SF6/H2 plasma. *Journal of Vacuum Science & Technology A*, 41(6):062601, 09 2023. ISSN 0734-2101. doi: 10.1116/6.0002965. URL https://doi.org/10.1116/6.0002965.

[108] Azmain A. Hossain, Sela Murphy, David S. Catherall, Anthony J. Ardizzi, and Austin J. Minnich. Atomic layer etching of niobium nitride using sequential exposures of o2 and h2/sf6 plasmas. *Journal of Vacuum Science & Technology A*, 43(4):042605, 07 2025. ISSN 0734-2101. doi: 10.1116/6.0004548. URL https://doi.org/10.1116/6.0004548.

[109] Mete M Bayrak, Anthony J Ardizzi, Sadhvikas Addamane, Kieran A Cleary, and Austin J Minnich. Atomic layer etching of ingaas using sequential exposures of atomic hydrogen and oxygen gas. *Semiconductor Science and*

Technology, 40(11):115012, nov 2025. doi: 10.1088/1361-6641/ae16cb. URL https://doi.org/10.1088/1361-6641/ae16cb.

[110] Hao Zhu, Wenqi Zhang, Kangcheng Zhao, Chaolong Jin, Zhaoyang Zhang, Kun Xu, Yang Liu, Jingtao Wang, and Viboon Saetang. Recent advances in precision deposition techniques on semiconductor surfaces: Mechanisms, methods, and applications. *Materials Today Communications*, 48:113495, 2025. ISSN 2352-4928. doi: https://doi.org/10.1016/j.mtcomm.2025.113495. URL https://www.sciencedirect.com/science/article/pii/S2352492825020070.

[111] Aaron J. Ptak. 4 - principles of molecular beam epitaxy. In Thomas F. Kuech, editor, *Handbook of Crystal Growth (Second Edition)*, Handbook of Crystal Growth, pages 161–192. North-Holland, Boston, second edition edition, 2015. ISBN 978-0-444-63304-0. doi: https://doi.org/10.1016/B978-0-444-63304-0.00004-4. URL https://www.sciencedirect.com/science/article/pii/B9780444633040000044.

[112] Nick A. Shepelin, Zahra P. Tehrani, Natacha Ohannessian, Christof W. Schneider, Daniele Pergolesi, and Thomas Lippert. A practical guide to pulsed laser deposition. *Chem. Soc. Rev.*, 52:2294–2321, 2023. doi: 10.1039/D2CS00938B. URL http://dx.doi.org/10.1039/D2CS00938B.

[113] Ion N. Mihailescu, Valentin S. Teodorescu, Eniko Gyorgy, Carmen Ristoscu, and R. Cristescu. Particulates in pulsed laser deposition: formation mechanisms and possible approaches to their elimination. In Dan C. Dumitras, Maria Dinescu, and Vitali I. Konov, editors, *ALT'01 International Conference on Advanced Laser Technologies*, volume 4762, pages 64 – 74. International Society for Optics and Photonics, SPIE, 2002. doi: 10.1117/12.478666. URL https://doi.org/10.1117/12.478666.

[114] E. Gy orgy, I. N. Mihailescu, M. Kompitsas, and A. Giannoudakos. A practical guide to pulsed laser deposition. *J. Optoelectron. Adv. M.*, 6:39–46, 2004.

[115] James A. Greer. Intelligent process control for pulsed-laser deposition. Technical Report WL-TR-96-4037, Wright Laboratory, Air Force Material Command, 1995.

[116] Chihiro Hamaguchi. *Basic Semiconductor Physics*. Springer, 2 edition, 2010.

[117] Gang Chen. *Nanoscale Energy Transport and Conversion*. Oxford University Press, 1 edition, 2005.

[118] Giuseppe Grosso and Giuseppe Pastori Parravicini. *Solid State Phyiscs*. Elsevier, 2 edition, 2014.

[119] P. Kocevar. Nonequilibrium phonon processes. In David K. Ferry, J. R. Barker, and C. Jacoboni, editors, *Physics of Nonlinear Transport in Semiconductors*, volume 52 of *NATO advanced study institutes series: Series B, Physics*, pages 401–413, New York, 1980. Plenum Press.

[120] V. V. Paranjape and B. V. Paranjape. Phonon excitation by electric field in semiconductors. *Phys. Rev.*, 166:757–762, Feb 1968. doi: 10.1103/PhysRev.166.757. URL https://link.aps.org/doi/10.1103/PhysRev.166.757.

[121] Hendrik J. Monkhorst and James D. Pack. Special points for brillouin-zone integrations. *Phys. Rev. B*, 13:5188–5192, Jun 1976. doi: 10.1103/PhysRevB.13.5188. URL https://link.aps.org/doi/10.1103/PhysRevB.13.5188.

[122] Arash A. Mostofi, Jonathan R. Yates, Young-Su Lee, Ivo Souza, David Vanderbilt, and Nicola Marzari. wannier90: A tool for obtaining maximally-localised wannier functions. *Computer Physics Communications*, 178(9): 685–699, 2008. ISSN 0010-4655. doi: https://doi.org/10.1016/j.cpc.2007.11.016. URL https://www.sciencedirect.com/science/article/pii/S0010465507004936.

[123] Nicola Marzari and David Vanderbilt. Maximally localized generalized wannier functions for composite energy bands. *Phys. Rev. B*, 56:12847–12865, Nov 1997. doi: 10.1103/PhysRevB.56.12847. URL https://link.aps.org/doi/10.1103/PhysRevB.56.12847.

[124] Lars Onsager. Reciprocal relations in irreversible processes. i. *Phys. Rev.*, 37: 405–426, Feb 1931. doi: 10.1103/PhysRev.37.405. URL https://link.aps.org/doi/10.1103/PhysRev.37.405.

[125] R. H. Fowler. *Statistical Mechanics*. Cambridge University Press, 2 edition, 1936.

[126] J. Von Borzeszkowski. On the electric field dependence of the conductivity of holes in si at low temperatures 1. the drift velocity under consideration of the non-equipartition of acoustic phonon energy. *physica status solidi (b)*, 73(2): 607–614, 1976. doi: https://doi.org/10.1002/pssb.2220730228. URL https://onlinelibrary.wiley.com/doi/abs/10.1002/pssb.2220730228.

[127] Yasuo Ohno. Spin-orbit band effects on silicon hot-hole transport. *Journal of Applied Physics*, 64(9):4549–4553, 1988. doi: 10.1063/1.341256. URL https://doi.org/10.1063/1.341256.

[128] A. Bareikis, V. Galdikas and R. Miliusyte. volume 3 of *Electrons in Semiconductors / Elektrony v poluprovodnikakh*, chapter 4. Fluctuations and Diffusion Coefficient / Fluktuacii Luktuacii I Kojefficient Diffuzii, pages 127–161. Vilnius: Mokslas, 1981. Academy of Sciences of the Lithuanian SSR / Lietuvos TSR Moksly Akademija.

[129] Paolo Giannozzi, Stefano Baroni, Nicola Bonini, Matteo Calandra, Roberto Car, Carlo Cavazzoni, Davide Ceresoli, Guido L Chiarotti, Matteo Cococcioni, Ismaila Dabo, Andrea Dal Corso, Stefano de Gironcoli, Stefano Fabris, Guido Fratesi, Ralph Gebauer, Uwe Gerstmann, Christos Gougoussis, Anton Kokalj, Michele Lazzeri, Layla Martin-Samos, Nicola Marzari, Francesco Mauri, Riccardo Mazzarello, Stefano Paolini, Alfredo Pasquarello, Lorenzo Paulatto, Carlo Sbraccia, Sandro Scandolo, Gabriele Sclauzero, Ari P Seitsonen, Alexander Smogunov, Paolo Umari, and Renata M Wentzcovitch. QUANTUM ESPRESSO: a modular and open-source software project for quantum simulations of materials. *J. Phys.: Condens. Mat*, 21(39):395502, sep 2009. doi: 10.1088/0953-8984/21/39/395502. URL https://doi.org/10.1088/0953-8984/21/39/395502.

[130] P Giannozzi, O Andreussi, T Brumme, O Bunau, M Buongiorno Nardelli, M Calandra, R Car, C Cavazzoni, D Ceresoli, M Cococcioni, N Colonna, I Carnimeo, A Dal Corso, S de Gironcoli, P Delugas, R A DiStasio, A Ferretti, A Floris, G Fratesi, G Fugallo, R Gebauer, U Gerstmann, F Giustino, T Gorni, J Jia, M Kawamura, H-Y Ko, A Kokalj, E Küçükbenli, M Lazzeri, M Marsili, N Marzari, F Mauri, N L Nguyen, H-V Nguyen, A Otero de-la Roza, L Paulatto, S Poncé, D Rocca, R Sabatini, B Santra, M Schlipf, A P Seitsonen, A Smogunov, I Timrov, T Thonhauser, P Umari, N Vast, X Wu, and S Baroni. Advanced capabilities for materials modelling with quantum ESPRESSO. *J. Phys.: Condens. Mat*, 29(46):465901, oct 2017. doi: 10.1088/1361-648x/aa8f79. URL https://doi.org/10.1088/1361-648x/aa8f79.

[131] Pauli Virtanen, Ralf Gommers, Travis E. Oliphant, Matt Haberland, Tyler Reddy, David Cournapeau, Evgeni Burovski, Pearu Peterson, Warren Weckesser, Jonathan Bright, Stéfan J. van der Walt, Matthew Brett, Joshua Wilson, K. Jarrod Millman, Nikolay Mayorov, Andrew R. J. Nelson, Eric Jones, Robert Kern, Eric Larson, C. J. Carey, İlhan Polat, Yu Feng, Eric W. Moore, Jake VanderPlas, Denis Laxalde, Josef Perktold, Robert Cimrman, Ian Henriksen, E. A. Quintero, Charles R. Harris, Anne M. Archibald, Antônio H. Ribeiro, Fabian Pedregosa, Paul van Mulbregt, Aditya Vijaykumar, Alessandro Pietro Bardelli, Alex Rothberg, Andreas Hilboll, Andreas Kloeckner, Anthony Scopatz, Antony Lee, Ariel Rokem, C. Nathan Woods, Chad Fulton, Charles Masson, Christian Häggström, Clark Fitzgerald, David A. Nicholson, David R. Hagen, Dmitrii V. Pasechnik, Emanuele Olivetti, Eric Martin, Eric Wieser, Fabrice Silva, Felix Lenders, Florian Wilhelm, G. Young, Gavin A. Price, Gert-Ludwig Ingold, Gregory E. Allen, Gregory R. Lee, Hervé Audren, Irvin Probst, Jörg P. Dietrich, Jacob Silterra, James T. Webber, Janko Slavič, Joel Nothman, Johannes Buchner, Johannes Kulick, Johannes L. Schönberger, José Vinícius de Miranda Cardoso, Joscha Reimer, Joseph Harrington, Juan Luis Cano Rodríguez, Juan Nunez-Iglesias, Justin Kuczynski, Kevin Tritz, Martin Thoma, Matthew

Newville, Matthias Kümmerer, Maximilian Bolingbroke, Michael Tartre, Mikhail Pak, Nathaniel J. Smith, Nikolai Nowaczyk, Nikolay Shebanov, Oleksandr Pavlyk, Per A. Brodtkorb, Perry Lee, Robert T. McGibbon, Roman Feldbauer, Sam Lewis, Sam Tygier, Scott Sievert, Sebastiano Vigna, Stefan Peterson, Surhud More, Tadeusz Pudlik, Takuya Oshima, Thomas J. Pingel, Thomas P. Robitaille, Thomas Spura, Thouis R. Jones, Tim Cera, Tim Leslie, Tiziano Zito, Tom Krauss, Utkarsh Upadhyay, Yaroslav O. Halchenko, Yoshiki Vázquez-Baeza, and SciPy 1.0 Contributors. Scipy 1.0: fundamental algorithms for scientific computing in python. *Nature Methods*, 17(3):261–272, Mar 2020. ISSN 1548-7105. doi: 10.1038/s41592-019-0686-2. URL https://doi.org/10.1038/s41592-019-0686-2.

[132] R. A. Logan and A. J. Peters. Impurity effects upon mobility in silicon. *Journal of Applied Physics*, 31(1):122–124, 1960. doi: 10.1063/1.1735385. URL https://doi.org/10.1063/1.1735385.

[133] L. Reggiani. Microscopic models in hot electron phenomena. *J. Phys. Soc. Japan Suppl. A*, 49:317–324, 1980. Proc. 15th Int. Conf. Physics of Semiconductors.

[134] N. A. Zakhlenyuk, V. A. Kochelap, and V. V. Mitin. Nonequilibrium fluctuations in semiconductors associated with energy scattering of charge carriers by lattice optical phonons. *Sov. Phys. JETP*, 68(4):863, 1989.

[135] C. Canali, C. Jacoboni, G. Ottaviani, and A. Alberigi-Quaranta. High-field diffusion of electrons in silicon. *Applied Physics Letters*, 27(5):278–280, 1975. doi: 10.1063/1.88465.

[136] A. Dargys and T. Banys. Dependence of the phenomenological energy relaxation time on electric field in n-si and n-ge at 77 °k. *physica status solidi (b)*, 52(2):699–706, 1972. doi: https://doi.org/10.1002/pssb.2220520241. URL https://onlinelibrary.wiley.com/doi/abs/10.1002/pssb.2220520241.

[137] Karl Hess and Karlheinz Seeger. Energie-relaxation warmer ladungsträger in germanium und silizium. *Zeitschrift für Physik A Hadrons and nuclei*, 218 (5):431–436, Oct 1969. ISSN 0939-7922. doi: 10.1007/BF01392422. URL https://doi.org/10.1007/BF01392422.

[138] David S. Catherall and Austin J. Minnich. High-field charge transport and noise in *p*-si from first principles. *Phys. Rev. B*, 107:035201, Jan 2023. doi: 10.1103/PhysRevB.107.035201. URL https://link.aps.org/doi/10.1103/PhysRevB.107.035201.

[139] D. S. Kim, H. L. Smith, J. L. Niedziela, C. W. Li, D. L. Abernathy, and B. Fultz. Phonon anharmonicity in silicon from 100 to 1500 k. *Phys. Rev. B*, 91:014307, Jan 2015. doi: 10.1103/PhysRevB.91.014307. URL https://link.aps.org/doi/10.1103/PhysRevB.91.014307.

[140] Neil W. Ashcroft and N. David Mermin. *Solid State Phyiscs*. Saunders College Publishing, 1 edition, 1976.

[141] K.S. Champlin, D.B. Armstrong, and P.D. Gunderson. Charge carrier inertia in semiconductors. *Proceedings of the IEEE*, 52(6):677–685, 1964. doi: 10.1109/PROC.1964.3049.

[142] Ernst Bonek. Millimeter-wave investigation of electronic conduction in semiconducting iii-v compounds. *Journal of Applied Physics*, 43(12):5101–5109, 1972. doi: 10.1063/1.1661079. URL https://doi.org/10.1063/1.1661079.

[143] A.F. Gibson, J.W. Granville, and E.G.S. Paige. A study of energy-loss processes in germanium at high electric fields using microwave techniques. *Journal of Physics and Chemistry of Solids*, 19(3):198–217, 1961. ISSN 0022-3697. doi: https://doi.org/10.1016/0022-3697(61)90029-4. URL https://www.sciencedirect.com/science/article/pii/0022369761900294.

[144] B. V. Paranjape. Behavior of hot electrons in microwave fields. *Phys. Rev.*, 122:1372–1375, Jun 1961. doi: 10.1103/PhysRev.122.1372. URL https://link.aps.org/doi/10.1103/PhysRev.122.1372.

[145] G. H. Glover. Study of electron energy relaxation times in gaas and inp. *Journal of Applied Physics*, 44(3):1295–1301, 1973. doi: 10.1063/1.1662343. URL https://doi.org/10.1063/1.1662343.

[146] D. Mukhopadhyay and B.R. Nag. Microwave incremental conductivity of insb at 77°k in the presence of high steady electric field. *Electronics Letters*, 5(2):20–21, 1969. doi: 10.1049/el:19690014. URL https://doi.org/10.1049/el:19690014.

[147] K. Seeger and H. Pötzl. Experimental and theoretical investigations in semiconductors concerning the boltzmann equation. In E. G. D. Cohen and W. Thirring, editors, *The Boltzmann Equation*, pages 341–378, Vienna, 1973. Springer Vienna. ISBN 978-3-7091-8336-6.

[148] E. Bonek, H.W. Pötzl, and K. Richter. High-frequency behavior of hot electrons in one-valley polar semiconductors. *Journal of Physics and Chemistry of Solids*, 31(5):1151–1161, 1970. ISSN 0022-3697. doi: https://doi.org/10.1016/0022-3697(70)90324-0. URL https://www.sciencedirect.com/science/article/pii/0022369770903240.

[149] Yuras K. Pozhela. *Transport parameters from microwave conductivity and noise measurements*, pages 113–147. Springer Berlin Heidelberg, Berlin, Heidelberg, 1985. ISBN 978-3-540-38849-4. doi: 10.1007/3-540-13321-6_4. URL https://doi.org/10.1007/3-540-13321-6_4.

[150] H. Nyquist. Thermal agitation of electric charge in conductors. *Phys. Rev.*, 32:110–113, Jul 1928. doi: 10.1103/PhysRev.32.110. URL https://link.aps.org/doi/10.1103/PhysRev.32.110.

[151] J. B. Johnson. Thermal agitation of electricity in conductors. *Phys. Rev.*, 32: 97–109, Jul 1928. doi: 10.1103/PhysRev.32.97. URL https://link.aps.org/doi/10.1103/PhysRev.32.97.

[152] G. S. Oehrlein, D. Metzler, and C. Li. Atomic layer etching at the tipping point: An overview. *ECS Journal of Solid State Science and Technology*, 4 (6):N5041, mar 2015. doi: 10.1149/2.0061506jss. URL https://dx.doi.org/10.1149/2.0061506jss.

[153] Chang Fang, Yanqiang Cao, Di Wu, and Aidong Li. Thermal atomic layer etching: Mechanism, materials and prospects. *Progress in Natural Science: Materials International*, 28(6):667–675, 2018. ISSN 1002-0071. doi: https://doi.org/10.1016/j.pnsc.2018.11.003. URL https://www.sciencedirect.com/science/article/pii/S1002007118304623.

[154] Steven M. George. Mechanisms of thermal atomic layer etching. *Accounts of Chemical Research*, 53(6):1151–1160, 2020. doi: 10.1021/acs.accounts.0c00084. URL https://doi.org/10.1021/acs.accounts.0c00084. PMID: 32476413.

[155] Andreas Fischer, Aaron Routzahn, Steven M. George, and Thorsten Lill. Thermal atomic layer etching: A review. *Journal of Vacuum Science & Technology A*, 39(3):030801, 03 2021. ISSN 0734-2101. doi: 10.1116/6.0000894. URL https://doi.org/10.1116/6.0000894.

[156] Andreas Fischer and Thorsten Lill. Plasma application in atomic layer etching. *Physics of Plasmas*, 30(8):080601, 08 2023. ISSN 1070-664X. doi: 10.1063/5.0158785. URL https://doi.org/10.1063/5.0158785.

[157] Colin T. Carver, John J. Plombon, Patricio E. Romero, Satyarth Suri, Tristan A. Tronic, and Robert B. Turkot. Atomic layer etching: An industry perspective. *ECS Journal of Solid State Science and Technology*, 4(6):N5005, feb 2015. doi: 10.1149/2.0021506jss. URL https://doi.org/10.1149/2.0021506jss.

[158] Keren J. Kanarik, Samantha Tan, and Richard A. Gottscho. Atomic layer etching: Rethinking the art of etch. *The Journal of Physical Chemistry Letters*, 9(16):4814–4821, 2018. doi: 10.1021/acs.jpclett.8b00997. URL https://doi.org/10.1021/acs.jpclett.8b00997. PMID: 30095919.

[159] Sven H. Gerritsen, Nicholas J. Chittock, Vincent Vandalon, Marcel A. Verheijen, Harm C. M. Knoops, Wilhelmus M. M. Kessels, and Adriaan J. M. Mackus. Surface smoothing by atomic layer deposition and

etching for the fabrication of nanodevices. *ACS Applied Nano Materials*, 5(12):18116–18126, 2022. doi: 10.1021/acsanm.2c04025. URL https://doi.org/10.1021/acsanm.2c04025.

[160] Chien-Wei Chen, Wen-Hao Cho, Chan-Yuen Chang, Chien-Ying Su, Nien-Nan Chu, Chi-Chung Kei, and Bor-Ran Li. CF4 plasma-based atomic layer etching of Al2O3 and surface smoothing effect. *Journal of Vacuum Science & Technology A*, 41(1):012602, 12 2022. ISSN 0734-2101. doi: 10.1116/6.0002210. URL https://doi.org/10.1116/6.0002210.

[161] Antoine Pacco, Yuya Akanishi, Quoc Toan Le, Els Kesters, Gayle Murdoch, and Frank Holsteyns. Controlled cobalt recess for advanced interconnect metallization. *Microelectronic Engineering*, 217:111131, 2019. ISSN 0167-9317. doi: https://doi.org/10.1016/j.mee.2019.111131. URL https://www.sciencedirect.com/science/article/pii/S0167931719302874.

[162] Yukun Gong, Kailash Venkatraman, and Rohan Akolkar. Communication—electrochemical atomic layer etching of copper. *Journal of The Electrochemical Society*, 165(7):D282, may 2018. doi: 10.1149/2.0901807jes. URL https://dx.doi.org/10.1149/2.0901807jes.

[163] Elham Mohimi, Xiaoqing I. Chu, Brian B. Trinh, Shaista Babar, Gregory S. Girolami, and John R. Abelson. Thermal atomic layer etching of copper by sequential steps involving oxidation and exposure to hexafluoroacetylacetone. *ECS Journal of Solid State Science and Technology*, 7(9):P491, aug 2018. doi: 10.1149/2.0211809jss. URL https://dx.doi.org/10.1149/2.0211809jss.

[164] Ryan Sheil, J. Mark P. Martirez, Xia Sang, Emily A. Carter, and Jane P. Chang. Precise control of nanoscale cu etching via gas-phase oxidation and chemical complexation. *The Journal of Physical Chemistry C*, 125(3):1819–1832, 2021. doi: 10.1021/acs.jpcc.0c08932. URL https://doi.org/10.1021/acs.jpcc.0c08932.

[165] Nicholas R. Johnson and Steven M. George. Wo3 and w thermal atomic layer etching using "conversion-fluorination" and "oxidation-conversion-fluorination" mechanisms. *ACS Applied Materials & Interfaces*, 9(39):34435–34447, 2017. doi: 10.1021/acsami.7b09161. URL https://doi.org/10.1021/acsami.7b09161. PMID: 28876892.

[166] Wenyi Xie, Paul C. Lemaire, and Gregory N. Parsons. Thermally driven self-limiting atomic layer etching of metallic tungsten using wf6 and o2. *ACS Applied Materials & Interfaces*, 10(10):9147–9154, 2018. doi: 10.1021/acsami.7b19024. URL https://doi.org/10.1021/acsami.7b19024. PMID: 29461793.

[167] Satish D. Athavale and Demetre J. Economou. Realization of atomic layer etching of silicon. *Journal of Vacuum Science & Technology B: Microelectronics and Nanometer Structures Processing, Measurement, and Phenomena*, 14(6):3702–3705, 11 1996. ISSN 1071-1023. doi: 10.1116/1.588651. URL https://doi.org/10.1116/1.588651.

[168] S. D. Park, D. H. Lee, and G. Y. Yeom. Atomic layer etching of si(100) and si(111) using cl2 and ar neutral beam. *Electrochemical and Solid-State Letters*, 8(8):C106, jun 2005. doi: 10.1149/1.1938848. URL https://dx.doi.org/10.1149/1.1938848.

[169] S. D. Park, C. K. Oh, J. W. Bae, G. Y. Yeom, T. W. Kim, J. I. Song, and J. H. Jang. Atomic layer etching of InP using a low angle forward reflected Ne neutral beam. *Applied Physics Letters*, 89(4):043109, 07 2006. ISSN 0003-6951. doi: 10.1063/1.2221504. URL https://doi.org/10.1063/1.2221504.

[170] K. K. Ko and S. W. Pang. Controllable layer-by-layer etching of III–V compound semiconductors with an electron cyclotron resonance source. *Journal of Vacuum Science & Technology B: Microelectronics and Nanometer Structures Processing, Measurement, and Phenomena*, 11(6):2275–2279, 11 1993. ISSN 1071-1023. doi: 10.1116/1.586889. URL https://doi.org/10.1116/1.586889.

[171] Yoshinobu Aoyagi, Kohji Shinmura, Kiyoshi Kawasaki, Tomoko Tanaka, Kenji Gamo, Susumu Namba, and Ichirou Nakamoto. Molecular layer etching of GaAs. *Applied Physics Letters*, 60(8):968–970, 02 1992. ISSN 0003-6951. doi: 10.1063/1.106477. URL https://doi.org/10.1063/1.106477.

[172] T. Meguro, M. Ishii, K. Kodama, Y. Yamamoto, K. Gamo, and Y. Aoyagi. Surface processes in digital etching of gaas. *Thin Solid Films*, 225(1):136–139, 1993. ISSN 0040-6090. doi: https://doi.org/10.1016/0040-6090(93)90142-C. URL https://www.sciencedirect.com/science/article/pii/004060909390142C.

[173] K.S. Min, S.H. Kang, J.K. Kim, Y.I. Jhon, M.S. Jhon, and G.Y. Yeom. Atomic layer etching of al2o3 using bcl3/ar for the interface passivation layer of iii–v mos devices. *Microelectronic Engineering*, 110:457–460, 2013. ISSN 0167-9317. doi: https://doi.org/10.1016/j.mee.2013.03.170. URL https://www.sciencedirect.com/science/article/pii/S0167931713004036.

[174] Younghee Lee, Craig Huffman, and Steven M. George. Selectivity in thermal atomic layer etching using sequential, self-limiting fluorination and ligand-exchange reactions. *Chemistry of Materials*, 28(21):7657–7665, 2016. doi: 10.1021/acs.chemmater.6b02543. URL https://doi.org/10.1021/acs.chemmater.6b02543.

[175] John Hennessy, Christopher S. Moore, Kunjithapatham Balasubramanian, April D. Jewell, Kevin France, and Shouleh Nikzad. Enhanced atomic layer etching of native aluminum oxide for ultraviolet optical applications. *Journal of Vacuum Science & Technology A*, 35(4):041512, 06 2017. ISSN 0734-2101. doi: 10.1116/1.4986945. URL https://doi.org/10.1116/1.4986945.

[176] Nicholas J. Chittock, Martijn F. J. Vos, Tahsin Faraz, Wilhelmus M. M. (Erwin) Kessels, Harm C. M. Knoops, and Adriaan J. M. Mackus. Isotropic plasma atomic layer etching of Al2O3 using a fluorine containing plasma and Al(CH3)3. *Applied Physics Letters*, 117(16):162107, 10 2020. ISSN 0003-6951. doi: 10.1063/5.0022531. URL https://doi.org/10.1063/5.0022531.

[177] Dominik Metzler, Robert L. Bruce, Sebastian Engelmann, Eric A. Joseph, and Gottlieb S. Oehrlein. Fluorocarbon assisted atomic layer etching of SiO2 using cyclic Ar/C4F8 plasma. *Journal of Vacuum Science & Technology A*, 32(2):020603, 12 2013. ISSN 0734-2101. doi: 10.1116/1.4843575. URL https://doi.org/10.1116/1.4843575.

[178] Sanbir S Kaler, Qiaowei Lou, Vincent M Donnelly, and Demetre J Economou. Atomic layer etching of silicon dioxide using alternating c4f8 and energetic ar+ plasma beams. *Journal of Physics D: Applied Physics*, 50(23):234001, may 2017. doi: 10.1088/1361-6463/aa6f40. URL https://dx.doi.org/10.1088/1361-6463/aa6f40.

[179] Kyongbeom Koh, Yongjae Kim, Chang-Koo Kim, and Heeyeop Chae. Quasi atomic layer etching of SiO2 using plasma fluorination for surface cleaning. *Journal of Vacuum Science & Technology A*, 36(1):01B106, 12 2017. ISSN 0734-2101. doi: 10.1116/1.5003417. URL https://doi.org/10.1116/1.5003417.

[180] Kang-Yi Lin, Chen Li, Sebastian Engelmann, Robert L. Bruce, Eric A. Joseph, Dominik Metzler, and Gottlieb S. Oehrlein. Selective atomic layer etching of HfO2 over silicon by precursor and substrate-dependent selective deposition. *Journal of Vacuum Science & Technology A*, 38(3):032601, 03 2020. ISSN 0734-2101. doi: 10.1116/1.5143247. URL https://doi.org/10.1116/1.5143247.

[181] Xu Yi, Qi-Fan Yang, Ki Youl Yang, Myoung-Gyun Suh, and Kerry Vahala. Soliton frequency comb at microwave rates in a high-q silica microresonator. *Optica*, 2(12):1078–1085, Dec 2015. doi: 10.1364/OPTICA.2.001078. URL https://opg.optica.org/optica/abstract.cfm?URI=optica-2-12-1078.

[182] Lue Wu, Heming Wang, Qifan Yang, Qing xin Ji, Boqiang Shen, Chengying Bao, Maodong Gao, and Kerry Vahala. Greater than one billion q factor for

on-chip microresonators. *Opt. Lett.*, 45(18):5129–5131, Sep 2020. doi: 10.1364/OL.394940. URL https://opg.optica.org/ol/abstract.cfm?URI=ol-45-18-5129.

[183] Lue Wu, Maodong Gao, Jin-Yu Liu, Hao-Jing Chen, Kellan Colburn, Henry A. Blauvelt, and Kerry J. Vahala. Hydroxyl ion absorption in on-chip high-q resonators. *Opt. Lett.*, 48(13):3511–3514, Jul 2023. doi: 10.1364/OL.492067. URL https://opg.optica.org/ol/abstract.cfm?URI=ol-48-13-3511.

[184] Hansuek Lee, Tong Chen, Jiang Li, Ki Youl Yang, Seokmin Jeon, Oskar Painter, and Kerry J. Vahala. Chemically etched ultrahigh-q wedge-resonator on a silicon chip. *Nature Photonics*, 6(6):369–373, Jun 2012. ISSN 1749-4893. doi: 10.1038/nphoton.2012.109. URL https://doi.org/10.1038/nphoton.2012.109.

[185] Yegeun Cho, Yongjae Kim, Sunjung Kim, and Heeyeop Chae. Atomic layer etching of SiO2 for surface cleaning using ammonium fluorosilicate with CF4/NH3 plasma. *Journal of Vacuum Science & Technology A*, 38(2):022604, 01 2020. ISSN 0734-2101. doi: 10.1116/1.5132986. URL https://doi.org/10.1116/1.5132986.

[186] Nobuya Miyoshi, Hiroyuki Kobayashi, Kazunori Shinoda, Masaru Kurihara, Kohei Kawamura, Yutaka Kouzuma, and Masaru Izawa. Atomic layer etching of SiO2 with self-limiting behavior on the surface modification step using sequential exposure of HF and NH3. *Journal of Vacuum Science & Technology A*, 40(1):012601, 12 2021. doi: 10.1116/6.0001517. URL https://doi.org/10.1116/6.0001517.

[187] Hiroto Ohtake, Nobuya Miyoshi, Kazunori Shinoda, Sumiko Fujisaki, and Yoshihide Yamaguchi. Isotropic atomic layer etchings of various materials by using dry chemical removal. *Japanese Journal of Applied Physics*, 62 (SG):SG0801, feb 2023. doi: 10.35848/1347-4065/acaed0. URL https://dx.doi.org/10.35848/1347-4065/acaed0.

[188] You Jung Gill, Doo San Kim, Hong Seong Gil, Ki Hyun Kim, Yun Jong Jang, Ye Eun Kim, and Geun Young Yeom. Cyclic etching of silicon oxide using nf3/h2 remote plasma and nh3 gas flow. *Plasma Processes and Polymers*, 18(11):2100063, 2021. doi: https://doi.org/10.1002/ppap.202100063. URL https://onlinelibrary.wiley.com/doi/abs/10.1002/ppap.202100063.

[189] Hong Seong Gil, Doo San Kim, Yun Jong Jang, Dea Whan Kim, Hea In Kwon, Gyoung Chan Kim, Dong Woo Kim, and Geun Young Yeom. Selective isotropic etching of sio2 over si3n4 using nf3/h2 remote plasma and methanol vapor. *Scientific Reports*, 13(1):11599, Jul 2023. ISSN 2045-2322. doi: 10.1038/s41598-023-38359-4. URL https://doi.org/10.1038/s41598-023-38359-4.

[190] Jaime W. DuMont, Amy E. Marquardt, Austin M. Cano, and Steven M. George. Thermal atomic layer etching of sio2 by a "conversion-etch" mechanism using sequential reactions of trimethylaluminum and hydrogen fluoride. *ACS Applied Materials & Interfaces*, 9(11):10296–10307, 2017. doi: 10.1021/acsami.7b01259. URL https://doi.org/10.1021/acsami.7b01259. PMID: 28240864.

[191] Rezwanur Rahman, Eric C. Mattson, Joseph P. Klesko, Aaron Dangerfield, Sandrine Rivillon-Amy, David C. Smith, Dennis Hausmann, and Yves J. Chabal. Thermal atomic layer etching of silica and alumina thin films using trimethylaluminum with hydrogen fluoride or fluoroform. *ACS Applied Materials & Interfaces*, 10(37):31784–31794, 2018. doi: 10.1021/acsami.8b10899. URL https://doi.org/10.1021/acsami.8b10899. PMID: 30179460.

[192] Eun-Jin Song, Ji-Hye Kim, Jung-Dae Kwon, Se-Hun Kwon, and Ji-Hoon Ahn. Silicon atomic layer etching by two-step plasma process consisting of oxidation and modification to form (nh4)2sif6, and its sublimation. *Japanese Journal of Applied Physics*, 57(10):106505, sep 2018. doi: 10.7567/JJAP.57.106505. URL https://dx.doi.org/10.7567/JJAP.57.106505.

[193] Aziz I. Abdulagatov and Steven M. George. Thermal atomic layer etching of silicon using o2, hf, and al(ch3)3 as the reactants. *Chemistry of Materials*, 30 (23):8465–8475, 2018. doi: 10.1021/acs.chemmater.8b02745. URL https://doi.org/10.1021/acs.chemmater.8b02745.

[194] Aziz I. Abdulagatov and Steven M. George. Thermal atomic layer etching of silicon nitride using an oxidation and "conversion etch" mechanism. *Journal of Vacuum Science & Technology A*, 38(2):022607, 02 2020. ISSN 0734-2101. doi: 10.1116/1.5140481. URL https://doi.org/10.1116/1.5140481.

[195] Robert W. Collins and Yeon Taik Kim. Ellipsometry for thin-film and surface analysis. *Analytical Chemistry*, 62(17):887A–890A, 1990. doi: 10.1021/ac00216a001. URL https://doi.org/10.1021/ac00216a001.

[196] Bert Boigtl ander. *Atomic Force Microscopy*. Springer, Cham, Switzerland, 2019.

[197] Fred A. Stevie and Carrie L. Donley. Introduction to x-ray photoelectron spectroscopy. *Journal of Vacuum Science & Technology A*, 38(6):063204, 09 2020. ISSN 0734-2101. doi: 10.1116/6.0000412. URL https://doi.org/10.1116/6.0000412.

[198] J. J. Hinchen and C. M. Banas. cw hf electric-discharge mixing laser. *Applied Physics Letters*, 17(9):386–388, 11 1970. ISSN 0003-6951. doi: 10.1063/1.1653447. URL https://doi.org/10.1063/1.1653447.

[199] Minoru Obara and Tomoo Fujioka. Time-resolved spectroscopic studies on the te hf chemical lasers using the mixtures of sf6/h2 and sf6/ch4. *Japanese Journal of Applied Physics*, 13(4):675, apr 1974. doi: 10.1143/JJAP.13.675. URL https://doi.org/10.1143/JJAP.13.675.

[200] D. M. Neumark, A. M. Wodtke, G. N. Robinson, C. C. Hayden, and Y. T. Lee. Molecular beam studies of the f+h2 reaction. *The Journal of Chemical Physics*, 82(7):3045–3066, 04 1985. ISSN 0021-9606. doi: 10.1063/1.448254. URL https://doi.org/10.1063/1.448254.

[201] Vladimir Volynets, Yuri Barsukov, Gonjun Kim, Ji-Eun Jung, Sang Ki Nam, Kyuhee Han, Shuo Huang, and Mark J. Kushner. Highly selective Si3N4/SiO2 etching using an NF3/N2/O2/H2 remote plasma. I. Plasma source and critical fluxes. *Journal of Vacuum Science & Technology A*, 38(2):023007, 01 2020. ISSN 0734-2101. doi: 10.1116/1.5125568. URL https://doi.org/10.1116/1.5125568.

[202] P A Pankratiev, Yu V Barsukov, A A Kobelev, A Ya Vinogradov, I V Miroshnikov, and A S Smirnov. Etching of si3n4 by sf6/h2 and sf6/d2 plasmas. *Journal of Physics: Conference Series*, 1697(1):012222, dec 2020. doi: 10.1088/1742-6596/1697/1/012222. URL https://dx.doi.org/10.1088/1742-6596/1697/1/012222.

[203] Ji-Eun Jung, Yuri Barsukov, Vladimir Volynets, Gonjun Kim, Sang Ki Nam, Kyuhee Han, Shuo Huang, and Mark J. Kushner. Highly selective si3n4/sio2 etching using an nf3/n2/o2/h2 remote plasma. ii. surface reaction mechanism. *Journal of Vacuum Science & Technology A*, 38(2):023008, 01 2020. ISSN 0734-2101. doi: 10.1116/1.5125569. URL https://doi.org/10.1116/1.5125569.

[204] C. M. Herzinger, B. Johs, W. A. McGahan, J. A. Woollam, and W. Paulson. Ellipsometric determination of optical constants for silicon and thermally grown silicon dioxide via a multi-sample, multi-wavelength, multi-angle investigation. *Journal of Applied Physics*, 83(6):3323–3336, 03 1998. ISSN 0021-8979. doi: 10.1063/1.367101. URL https://doi.org/10.1063/1.367101.

[205] Joseph R. Vella, Mahmoud A. I. Elgarhy, Qinzhen Hao, Vincent M. Donnelly, and David B. Graves. Reactor wall effects in si–cl2–ar atomic layer etching. *Journal of Vacuum Science & Technology A*, 42(4):042604, 06 2024. ISSN 0734-2101. doi: 10.1116/6.0003651. URL https://doi.org/10.1116/6.0003651.

[206] Masatoshi Kawakami, Dominik Metzler, Chen Li, and Gottlieb S. Oehrlein. Effect of the chamber wall on fluorocarbon-assisted atomic layer etching of sio2 using cyclic ar/c4f8 plasma. *Journal of Vacuum Science & Technology A*, 34(4):040603, 05 2016. ISSN 0734-2101. doi: 10.1116/1.4949260. URL https://doi.org/10.1116/1.4949260.

[207] National Institute of Standards and Technology. Nist x-ray photoelectron spectroscopy database, 2000. Accessed: 2024-04-04.

[208] Jessica A. Murdzek and Steven M. George. Effect of crystallinity on thermal atomic layer etching of hafnium oxide, zirconium oxide, and hafnium zirconium oxide. *Journal of Vacuum Science & Technology A*, 38(2): 022608, 02 2020. ISSN 0734-2101. doi: 10.1116/1.5135317. URL https://doi.org/10.1116/1.5135317.

[209] Jessica A. Murdzek, Adarsh Rajashekhar, Raghuveer S. Makala, and Steven M. George. Thermal atomic layer etching of amorphous and crystalline Al2O3 films. *Journal of Vacuum Science & Technology A*, 39 (4):042602, 06 2021. ISSN 0734-2101. doi: 10.1116/6.0000995. URL https://doi.org/10.1116/6.0000995.

[210] M. F. Ceiler, P. A. Kohl, and S. A. Bidstrup. Plasma-enhanced chemical vapor deposition of silicon dioxide deposited at low temperatures. *Journal of The Electrochemical Society*, 142(6):2067, jun 1995. doi: 10.1149/1.2044242. URL https://dx.doi.org/10.1149/1.2044242.

[211] Lukáš Šimurka, Radim Čtvrtlík, Jan Tomaštík, Gence Bektaş, Jan Svoboda, and Klaus Bange. Mechanical and optical properties of sio2 thin films deposited on glass. *Chemical Papers*, 72(9):2143–2151, Sep 2018. ISSN 1336-9075. doi: 10.1007/s11696-018-0420-z. URL https://doi.org/10.1007/s11696-018-0420-z.

[212] Gijs Dingemans, Cristian Van Helvoirt, M.C.M. Van de Sanden, and W. M. Kessels. Plasma-assisted atomic layer deposition of low temperature sio2. *ECS Transactions*, 35(4):191, apr 2011. doi: 10.1149/1.3572283. URL https://dx.doi.org/10.1149/1.3572283.

[213] K. Taniguchi, M. Tanaka, C. Hamaguchi, and K. Imai. Density relaxation of silicon dioxide on (100) silicon during thermal annealing. *Journal of Applied Physics*, 67(5):2195–2198, 03 1990. ISSN 0021-8979. doi: 10.1063/1.345563. URL https://doi.org/10.1063/1.345563.

[214] M. L. Gorodetsky, A. A. Savchenkov, and V. S. Ilchenko. Ultimate q of optical microsphere resonators. *Opt. Lett.*, 21(7):453–455, Apr 1996. doi: 10.1364/OL.21.000453. URL https://opg.optica.org/ol/abstract.cfm?URI=ol-21-7-453.

[215] Haozhe Wang, Azmain Hossain, David Catherall, and Austin J. Minnich. Isotropic plasma-thermal atomic layer etching of aluminum nitride using sf6 plasma and al(ch3)3. *Journal of Vacuum Science & Technology A*, 41 (3):032606, 05 2023. ISSN 0734-2101. doi: 10.1116/6.0002476. URL https://doi.org/10.1116/6.0002476.

[216] Donald M. Mattox. *Handbook of Physical Vapor Deposition (PVD) Processing*. Elsevier Science, Oxford, UK, 2nd edition, 2010. ISBN 0815520387.

[217] Jafar Safarian and Thorvald A. Engh. Vacuum evaporation of pure metals. *Metallurgical and Materials Transactions A*, 44(2):747–753, Feb 2013. ISSN 1543-1940. doi: 10.1007/s11661-012-1464-2. URL https://doi.org/10.1007/s11661-012-1464-2.

[218] Milo D. Koretsky. *Engineering and Chemical Thermodynamics*. Wiley, 2 edition, 2013.

[219] Theodore Gray. Heat of vaporization of the elements. https://periodictable.com/Properties/A/VaporizationHeat.an.html. Accessed: 2026-02-10.

[220] E. R. Plante and A. B. Sessoms. Vapor pressure and heat of sublimation of tungsten. *Journal of Research of the National Bureau of Standards - A. Physics and Chemistry*, 77A(2):237–242, 1973. doi: 10.6028/jres.077A.015. URL https://nvlpubs.nist.gov/nistpubs/jres/77A/jresv77An2p237_A1b.pdf.

[221] James Welty, Gregory Rorrer, and David Foster. *Fundamentals of Momentum, Heat, and Mass Transfer*. Wiley, 6 edition, 2015.

[222] G. Groh. Vacuum deposition of thin films by means of a co2 laser. *Journal of Applied Physics*, 39(12):5804–5805, 11 1968. ISSN 0021-8979. doi: 10.1063/1.1656056. URL https://doi.org/10.1063/1.1656056.

[223] Jeffrey T. Cheung and Haluk Sankur. Growth of thin films by laser-induced evaporation. *Critical Reviews in Solid State and Materials Sciences*, 15(1):63–109, 1988. doi: 10.1080/10408438808244625. URL https://doi.org/10.1080/10408438808244625.

[224] H. Sankur and J. T. Cheung. Formation of dielectric and semiconductor thin films by laser-assisted evaporation. *Applied Physics A*, 47(3):271–284, Nov 1988. ISSN 1432-0630. doi: 10.1007/BF00615933. URL https://doi.org/10.1007/BF00615933.

[225] Wolfgang Braun and Jochen Mannhart. Film deposition by thermal laser evaporation. *AIP Advances*, 9(8):085310, 08 2019. ISSN 2158-3226. doi: 10.1063/1.5111678. URL https://doi.org/10.1063/1.5111678.

[226] Thomas J. Smart, Jochen Mannhart, and Wolfgang Braun. Thermal laser evaporation of elements from across the periodic table. *Journal of Laser Applications*, 33(2):022008, 03 2021. ISSN 1042-346X. doi: 10.2351/7.0000348. URL https://doi.org/10.2351/7.0000348.

[227] Dong Yeong Kim, Jochen Mannhart, and Wolfgang Braun. Thermal laser evaporation for the growth of oxide films. *APL Materials*, 9(8):081105, 08 2021. ISSN 2166-532X. doi: 10.1063/5.0055237. URL https://doi.org/10.1063/5.0055237.

[228] Dong Yeong Kim, Thomas J. Smart, Lena Majer, Sander Smink, Jochen Mannhart, and Wolfgang Braun. Thermal laser evaporation of elemental metal sources in oxygen. *Journal of Applied Physics*, 132(24):245110, 12 2022. ISSN 0021-8979. doi: 10.1063/5.0114600. URL https://doi.org/10.1063/5.0114600.

[229] B. Brauns, D. Schäfer, R. Wolf, and G. Zscherpe. Deposition of laser mirrors by laser beam evaporation. *Optica Acta: International Journal of Optics*, 33(5):545–547, 1986. doi: 10.1080/713821984. URL https://doi.org/10.1080/713821984.

[230] V. S. Ban and D. A. Kramer. Thin films of semiconductors and dielectrics produced by laser evaporation. *Journal of Materials Science*, 5(11):978–982, Nov 1970. ISSN 1573-4803. doi: 10.1007/BF00558179. URL https://doi.org/10.1007/BF00558179.

[231] Susumu Fujimori. Formation of carbon films by laser deposition. *Shinkū*, 23 (7):333–338, 1980. doi: 10.3131/jvsj.23.333.

[232] H. Sankur and J. T. Cheung. Highly oriented zno films grown by laser evaporation. *Journal of Vacuum Science & Technology A*, 1(4):1806–1809, 10 1983. ISSN 0734-2101. doi: 10.1116/1.572219. URL https://doi.org/10.1116/1.572219.

[233] H. Sankur and R. Hall. Thin-film deposition by laser-assisted evaporation. *Appl. Opt.*, 24(20):3343–3347, Oct 1985. doi: 10.1364/AO.24.003343. URL https://opg.optica.org/ao/abstract.cfm?URI=ao-24-20-3343.

[234] X.J. Yin, G.R. Lai, J.S. Chen, and J.S. Kao. Conductivity enhancement in transparetn zno films via al-dopping produced by cw-co2 laser-induced evaporation. *Surface and Coatings Technology*, 90(3):239–246, 1997. ISSN 0257-8972. doi: https://doi.org/10.1016/S0257-8972(96)03150-7. URL https://www.sciencedirect.com/science/article/pii/S0257897296031507.

[235] S. Mineta, M. Kohata, N. Yasunaga, and Y. Kikuta. Preparation of cubic boron nitride film by co2 laser physical vapour deposition with simultaneous nitrogen ion supply. *Thin Solid Films*, 189(1):125–138, 1990. ISSN 0040-6090. doi: https://doi.org/10.1016/0040-6090(90)90033-A. URL https://www.sciencedirect.com/science/article/pii/004060909090033A.

[236] Naga Prathibha Jasti, Shay Tirosh, Ansuman Halder, Eti Teblum, and David Cahen. Continuous wave laser-assisted evaporation of halide perovskite thin

films from a single stoichiometric source. *Journal of Vacuum Science & Technology A*, 42(4):043406, 05 2024. ISSN 0734-2101. doi: 10.1116/6.0003607. URL https://doi.org/10.1116/6.0003607.

[237] Amjad Al Taleb, Lena N. Majer, Espen W. Selfors, Sander Smink, Bodil Holst, Jochen Mannhart, Wolfgang Braun, and Daniel Farías. Ultrasmooth graphene-coated metal thin films on sapphire grown by thermal laser epitaxy. *Thin Solid Films*, 758:139449, 2022. ISSN 0040-6090. doi: https://doi.org/10.1016/j.tsf.2022.139449. URL https://www.sciencedirect.com/science/article/pii/S0040609022003637.

[238] Thomas J. Smart, Felix V. E. Hensling, Dong Yeong Kim, Lena N. Majer, Y. Eren Suyolcu, Dominik Dereh, Darrell G. Schlom, Debdeep Jena, Jochen Mannhart, and Wolfgang Braun. Why thermal laser epitaxy aluminum sources yield reproducible fluxes in oxidizing environments. *Journal of Vacuum Science & Technology A*, 41(4):042701, 05 2023. ISSN 0734-2101. doi: 10.1116/6.0002632. URL https://doi.org/10.1116/6.0002632.

[239] Thomas James Smart. *Thermal Laser Epitaxy: From Fundamental Physics to the Growth of Novel Thin Films*. PhD thesis, University of Stuttgart, 2023.

[240] Dong Yeong Kim, Thomas J. Smart, Jochen Mannhart, and Wolfgang Braun. Thermal laser epitaxy of carbon films. *Crystal Growth & Design*, 23(11):8087–8093, Nov 2023. ISSN 1528-7483. doi: 10.1021/acs.cgd.3c00833. URL https://doi.org/10.1021/acs.cgd.3c00833.

[241] Thomas J. Smart, Dong Yeong Kim, and Wolfgang Braun. Twin-free thermal laser epitaxy of si on sapphire. *Journal of Vacuum Science & Technology B*, 42(6):062204, 10 2024. ISSN 2166-2746. doi: 10.1116/6.0003945. URL https://doi.org/10.1116/6.0003945.

[242] Lena N. Majer, Tolga Acartürk, Peter A. van Aken, Wolfgang Braun, Luca Camuti, Johan Eckl-Haese, Jochen Mannhart, Takeyoshi Onuma, Ksenia S. Rabinovich, Darrell G. Schlom, Sander Smink, Ulrich Starke, Jacob Steele, Patrick Vogt, Hongguang Wang, and Felix V. E. Hensling. Adsorption-controlled growth of homoepitaxial c-plane sapphire films. *APL Materials*, 12(9):091112, 09 2024. ISSN 2166-532X. doi: 10.1063/5.0224092. URL https://doi.org/10.1063/5.0224092.

[243] Lena N. Majer, Sander Smink, Wolfgang Braun, Hongguang Wang, Peter A. van Aken, Jochen Mannhart, and Felix V. E. Hensling. Growth of high-quality ruthenium films on sapphire. *Journal of Vacuum Science & Technology A*, 42(5):052702, 07 2024. ISSN 0734-2101. doi: 10.1116/6.0003756. URL https://doi.org/10.1116/6.0003756.

[244] Lena N. Majer, Sander Smink, Wolfgang Braun, Bernhard Fenk, Varun Harbola, Benjamin Stuhlhofer, Hongguang Wang, Peter A. van Aken, Jochen Mannhart, and Felix V. E. Hensling. α-ta films on c-plane sapphire with

enhanced microstructure. *APL Materials*, 12(9):091108, 09 2024. ISSN 2166-532X. doi: 10.1063/5.0218021. URL https://doi.org/10.1063/5.0218021.

[245] Thomas J Smart, Bilen Emek Abali, Hans Boschker, and Wolfgang Braun. Deposition rates in thermal laser epitaxy: simulation and experiment. *Journal of Physics D: Applied Physics*, 58(20):205303, apr 2025. doi: 10.1088/1361-6463/adcb4d. URL https://doi.org/10.1088/1361-6463/adcb4d.

[246] Rudolf Gross, J. Klein, B. Wiedenhorst, C. Hoefener, U. Schoop, J. B. Philipp, M. Schonecke, F. Herbstritt, L. Alff, Yafeng Lu, A. Marx, S. Schymon, S. Thienhaus, and W. Mader. Heteroepitaxial growth of transition metal oxides using UHV laser molecular beam epitaxy. In Davor Pavuna and Ivan Bozovic, editors, *Superconducting and Related Oxides: Physics and Nanoengineering IV*, volume 4058, pages 278 – 294. International Society for Optics and Photonics, SPIE, 2000. doi: 10.1117/12.397845. URL https://doi.org/10.1117/12.397845.

[247] Douglas H. Lowndes, D. B. Geohegan, A. A. Puretzky, D. P. Norton, and C. M. Rouleau. Synthesis of novel thin-film materials by pulsed laser deposition. *Science*, 273(5277):898–903, 1996. doi: 10.1126/science.273.5277.898. URL https://www.science.org/doi/abs/10.1126/science.273.5277.898.

[248] Roudy Hanna, Sören Ihssen, Simon Geisert, Umut Kocak, Matteo Arfini, Albert Hertel, Thomas J. Smart, Michael Schleenvoigt, Tobias Schmitt, Joscha Domnick, Kaycee Underwood, Abdur Rehman Jalil, Jin Hee Bae, Benjamin Bennemann, Mathieu Féchant, Mitchell Field, Martin Spiecker, Nicolas Zapata, Christian Dickel, Erwin Berenschot, Niels Tas, Gary A. Steele, Detlev Grützmacher, Ioan M. Pop, and Peter Schüffelgen. On-chip stencil lithography for superconducting qubits, 2025. URL https://arxiv.org/abs/2507.17005.

[249] Dong Yeong Kim, Varun Harbola, Seungwon Jung, Jinjoo Lee, Sukanya Roy, Felix V. E. Hensling, Lena N. Majer, Hongguang Wang, Peter A. van Aken, Joao Marcelo J. Lopes, Neha Aggarwal, Jochen Mannhart, and Wolfgang Braun. Nitride thin films grown by thermal laser epitaxy. *APL Materials*, 13(1):011125, 01 2025. ISSN 2166-532X. doi: 10.1063/5.0238169. URL https://doi.org/10.1063/5.0238169.

[250] Susumu Fujimori, Toshio Kasai, and Takahiro Inamura. Carbon film formation by laser evaporation and ion beam sputtering. *Thin Solid Films*, 92(1):71–80, 1982. ISSN 0040-6090. doi: https://doi.org/10.1016/0040-6090(82)90189-4. URL https://www.sciencedirect.com/science/article/pii/0040609082901894.

[251] P. Maier-Komor. Preparation of isotope targets using laser beam evaporation techniques. *Nuclear Instruments and Methods*, 167(1):73–76,

1979. ISSN 0029-554X. doi: https://doi.org/10.1016/0029-554X(79)90480-4. URL https://www.sciencedirect.com/science/article/pii/0029554X79904804.

[252] Milton S. Hess and John F. Milkosky. Vapor deposition of platinum using cw laser energy. *Journal of Applied Physics*, 43(11):4680–4683, 11 1972. ISSN 0021-8979. doi: 10.1063/1.1660988. URL https://doi.org/10.1063/1.1660988.

[253] G. Hass and J. B. Ramsey. Vacuum deposition of dielectric and semiconductor films by a co2 laser. *Appl. Opt.*, 8(6):1115–1118, Jun 1969. doi: 10.1364/AO.8.001115. URL https://opg.optica.org/ao/abstract.cfm?URI=ao-8-6-1115.

[254] W. W. Duley. *Laser Processing and Analysis of Materials*. Plenum Press, 1 edition, 1983.

[255] Dong Yeong Kim, Jochen Mannhart, and Wolfgang Braun. Epitaxial film growth by thermal laser evaporation. *Journal of Vacuum Science & Technology A*, 39(5):053406, 08 2021. ISSN 0734-2101. doi: 10.1116/6.0001177. URL https://doi.org/10.1116/6.0001177.

[256] Wolfgang Braun, Maren Jäger, Gennadii Laskin, Prosper Ngabonziza, Wolfgang Voesch, Pascal Wittlich, and Jochen Mannhart. In situ thermal preparation of oxide surfaces. *APL Materials*, 8(7):071112, 07 2020. ISSN 2166-532X. doi: 10.1063/5.0008324. URL https://doi.org/10.1063/5.0008324.

[257] Thorlabs Inc. Off-axis parabolic mirrors. https://www.thorlabs.com/off-axis-parabolic-mirrors. Accessed: 2026-02-03.

[258] D.W. Pashley. The nucleation, growth, structure and epitaxy of thin surface films. *Advances in Physics*, 14(55):327–416, 1965. doi: 10.1080/00018736500101071. URL https://doi.org/10.1080/00018736500101071.

[259] Stefano Giurgola, Anabel Rodriguez, Luis Martinez, Paolo Vergani, Federico Lucchi, Sarah Benchabane, and Valerio Pruneri. Ultra thin nickel transparent electrodes. *Journal of Materials Science: Materials in Electronics*, 20(1):181–184, Jan 2009. ISSN 1573-482X. doi: 10.1007/s10854-007-9519-7. URL https://doi.org/10.1007/s10854-007-9519-7.

[260] M.A. Angadi and L.A. Udachan. Electrical properties of thin nickel films. *Thin Solid Films*, 79(2):149–153, 1981. ISSN 0040-6090. doi: https://doi.org/10.1016/0040-6090(81)90272-8. URL https://www.sciencedirect.com/science/article/pii/0040609081902728.

[261] Su-Yang Xu, Ilya Belopolski, Nasser Alidoust, Madhab Neupane, Guang Bian, Chenglong Zhang, Raman Sankar, Guoqing Chang, Zhujun Yuan, Chi-Cheng Lee, Shin-Ming Huang, Hao Zheng, Jie Ma, Daniel S. Sanchez, BaoKai Wang, Arun Bansil, Fangcheng Chou, Pavel P. Shibayev, Hsin Lin, Shuang Jia, and M. Zahid Hasan. Discovery of a weyl fermion semimetal and topological fermi arcs. *Science*, 349(6248):613–617, 2015. doi: 10.1126/science.aaa9297. URL https://www.science.org/doi/abs/10.1126/science.aaa9297.

[262] Yu Saito, Tsutomu Nojima, and Yoshihiro Iwasa. Highly crystalline 2d superconductors. *Nature Reviews Materials*, 2(1):16094, Dec 2016. ISSN 2058-8437. doi: 10.1038/natrevmats.2016.94. URL https://doi.org/10.1038/natrevmats.2016.94.

[263] Feliciano Giustino, Jin Hong Lee, Felix Trier, Manuel Bibes, Stephen M Winter, Roser Valentí, Young-Woo Son, Louis Taillefer, Christoph Heil, Adriana I Figueroa, Bernard Plaçais, QuanSheng Wu, Oleg V Yazyev, Erik P A M Bakkers, Jesper Nygård, Pol Forn-Díaz, Silvano De Franceschi, J W McIver, L E F Foa Torres, Tony Low, Anshuman Kumar, Regina Galceran, Sergio O Valenzuela, Marius V Costache, Aurélien Manchon, Eun-Ah Kim, Gabriel R Schleder, Adalberto Fazzio, and Stephan Roche. The 2021 quantum materials roadmap. *Journal of Physics: Materials*, 3(4):042006, jan 2021. doi: 10.1088/2515-7639/abb74e. URL https://doi.org/10.1088/2515-7639/abb74e.